eXPRESS Polymer Letters Vol.3, No.11 (2009) 676
Available online at www.expresspolymlett.com
DOI: 10.3144/expresspolymlett.2009.84

Editorial corner – a personal view

Thermoset polymers containing bio-based renewable resources

J. Karger-Kocsis[*]

Department of Polymer Engineering, Budapest University of Technology and Economics, Műegyetem rkp. 3., H-1111 Budapest, Hungary, and Department of Polymer Technology, Faculty of Engineering and Built Environment, Tshwane University of Technology, Pretoria 0001, Republic of South Africa

The use of materials from renewable resources is becoming increasingly important mostly due to environmental and sustainability issues. To replace petrochemical-based materials with bio (agricultural)-based ones seems to be a straightforward strategy provided that there is no competition between food and non-food uses. Unfortunately, recent price trends suggest a strong interplay between food and non-food applications possibly due to the fact that no further fields are available for agricultural cultivation.

Genetic engineering, heavily pushed forward at present, may contribute to a 'polymer-conform design' of natural molecules (for example oils with more double bonds) and also to their better yield. This raises, however, a further ethical question related to the possible contamination of traditional food feedstock with gene-manipulated one. There is much to clarify in respect even when accepting that gene manipulation is nothing else than some kind of a 'forced evolution'.

Oils, fats, resins, agricultural waste have been used in various polymer recipes in the past as modifiers, extenders. Their role is changing nowadays: instead of additives they are becoming essential parts of the polymers. However, in order to widen the use bio-based feedstock, its constituents have to be functionalized. The functional groups guarantee the required reactivity of bio-based molecules. Accordingly, bio-based intermediates are predestined for use in thermosets instead of thermoplastics.

Pioneering works have already outlined different reaction pathways for example for the functionalization of plant oils. The related strategies considered also the follow-up reactions of the functionalized oils in ring-opening, free radical polymerization, and polycondensation processes. This task is, however, not yet finished – chemists have to check the feasibility of different options and present the related technologies to 'decision-makers'. For the functionalization catalytic methods are likely more suited than those based on traditional chemistry. Though the target of some research works was the full replacement of 'petroresins', the proper combination of petrochemical- and bio-based (agricultural, 'green' etc.) resins is our next task. Functionalized (acrylated, epoxidized, acrylated/epoxidized, maleinated) plant oils are becoming available commercially and their property modification potential in traditional resins should be investigated. There is also a great potential to modify/produce phenolics from bio-based materials. Break-through with the use of bio-based renewable resources requires, however, also support from the politics – there is likely no success when this issue is merely governed by the market.

Prof. Dr.-Ing. Dr. h.c. József Karger-Kocsis
Editor-in-chief

---

[*] Corresponding author, e-mail: karger@pt.bme.hu

eXPRESS Polymer Letters Vol.3, No.11 (2009) 677–683
Available online at www.expresspolymlett.com
DOI: 10.3144/expresspolymlett.2009.85

PP-EPDM thermoplastic vulcanisates (TPVs) by electron induced reactive processing

K. Naskar[1,2], *U. Gohs*[1*], *U. Wagenknecht*[1], *G. Heinrich*[1]

[1]Leibniz-Institut für Polymerforschung Dresden e.V., Hohe Strasse 6, D-01069 Dresden, Germany
[2]Rubber Technology Centre, Indian Institute of Technology, Kharagpur, Kharagpur-721302, West Bengal, India

Received 23 June 2009; accepted in revised form 12 August 2009

Abstract. Reactive processing combines melt mixing process and chemical reaction simultaneously. TPVs are produced by such reactive processing. Polymer modification with high energy electrons is based on generation of excited atoms or molecules and ions for subsequent molecular changes via radical induced chemical reactions. In the present study, electron induced reactive processing is used for the development of TPVs. A 1.5 MeV electron accelerator was directly coupled to an internal mixer in order to induce chemical reactions by energy input via high energy electrons under dynamic conditions of melt mixing of polypropylene (PP) and ethylene propylene diene monomer rubber (EPDM). The influence of absorbed dose (25 to 100 kGy) as well as electron energy (1.5 and 0.6 MeV) and electron treatment time (15 to 60 s) have been studied. Increased values of both tensile strength and elongation at break of the TPVs indicate *in-situ* compatibilisation of PP and EPDM as well as cross-linking in the EPDM phase upon electron induced reactive processing. Dynamic mechanical analyses showed a decrease in value of glass transition temperature peak of EPDM in tangent delta curve with increasing dose. This also indicates higher degree of cross-linking in EPDM phase, which is further supported by a gel content that is higher than the EPDM content itself in the blend.

Keywords: *polymer blends and alloys, PP, EPDM, thermoplastic vulcanisate, electron induced reactive processing*

1. Introduction

Thermoplastic elastomers (TPEs) are one of the fastest growing polymeric materials which combine the elastic and mechanical properties of cross-linked rubbers with the melt processability of thermoplastics [1, 2]. TPEs find lot of applications in automotives, buildings and constructions, wires and cables, soft touch etc. The most important advantage of a TPE is its ability to reuse and recycle the production scrap and waste. TPVs or dynamic vulcanisates are a special class of TPEs, produced by simultaneously mixing and cross-linking a rubber with a thermoplastic at elevated temperature [3–5]. As a result a typical morphology is formed, where the cross-linked rubber particles are finely dispersed in a continuous matrix of thermoplastic. TPVs based on blends of PP and EPDM rubber are most significant from a commercial point of view, where the rubber phase is generally cross-linked either by activated phenol formaldehyde resins or by peroxides [6–12]. Besides advantages, both resin and peroxide cross-linking systems have their own limitations. For instance, phenolic resin has a strong tendency to absorb moisture even at ambient temperature and also appear as a dark brown color. On the other hand, peroxide cross-linked TPVs often provide an unpleasant smell or may show a blooming effect. Furthermore, the rate of generation of peroxide radicals at a constant temperature changes as a function of time. These disadvantages of resins and peroxides create a demand for other alternatives.

---

[*] Corresponding author, e-mail: gohs@ipfdd.de

Dynamic vulcanisation by electron induced reactive processing is a potential option.

Influence of electron beam (EB) on PP under static conditions is well known in the literature [13–16] and characterises a process where required absorbed dose is applied to form parts (after molding) in solid state and at room temperature. EB cross-linking of EPDM rubber under static conditions is also reported by several authors [17–19]. The absorbed dose controls the energy input per unit of mass as well as the total number of radicals. However, the effects of high energy electrons in PP-EPDM blends under dynamic conditions were not yet explored. Electron induced reactive processing is a novel technique where chemical reactions are induced by spatial and temporal precise energy input via high energy electrons under dynamic conditions of melt mixing. In this novel process, the penetration depth of electrons is limited to a part of mixing volume. The total mixing volume is modified due to the change of polymer mass within the penetration depth of electrons during mixing process. Further, electron treatment time and electron energy do not only control dose rate and penetration depth, respectively. In the novel process, electron treatment time also influences the ratio of radical generation rate to mixing rate (dose per rotation) and electron energy controls the ratio of modified volume to total mixing chamber volume (r_{vol}).

Thus, the primary objective of the present investigation is to develop PP-EPDM based TPVs at 50:50 blend ratio under various conditions (absorbed dose, electron treatment time and electron energy) of electron induced reactive processing. The mechanical, thermal, dynamic mechanical, and morphological characteristics of various dynamically electron cross-linked PP-EPDM blends were pursued to get an in-sight.

2. Experimental

2.1. Materials

Buna EP G 6850, the ethylidene norbornene (ENB) containing EPDM rubber, was obtained from Lanxess, Leverkusen, Germany. The EPDM contains 51 wt% of ethylene and 7.7 wt% of ENB. It has a Mooney viscosity, ML (1+4) at 125°C of 60 and a density of 0.860 g/cm^3. PP HD120MO, a polypropylene homopolymer, was obtained from Borealis, Düsseldorf, Germany. The melt flow rate of the polypropylene, measured at 230°C and 2.16 kg, amounts to 8.0 g/10 min. It has a density of 0.908 g/cm^3.

2.2. Preparation of PP/EPDM TPVs

All TPVs were prepared by a batch process in a Brabender mixing chamber, having a mixing chamber volume of 50 cm^3, with a rotor speed of 45 rpm at 175–180°C in presence of air. The friction ratio of the rotors amounts to 1:1.5. Figure 1 shows a schematic representation of the unique set-up. The total time of mixing was 16 min due to safety regulations of electron accelerator. The experimental variables were absorbed dose (25, 50, and 100 kGy), electron treatment time (15, 30, and 60 s), and electron energy (0.6 and 1.5 MeV). Immediately after mixing, the composition was pressed manually by metallic plates without any additional heating to achieve a sheet of about 2 mm thickness. This sheet was cut into small pieces and pressed in a compression molding machine (Rucks Maschinenbau, Glauchau, Germany) at 200°C, 6 min, and 88 bar pressure. The sheet was then cooled down to room temperature under pressure. Test specimens were die-cut from the compression molded sheet and used for testing after 24 h of storage at room temperature.

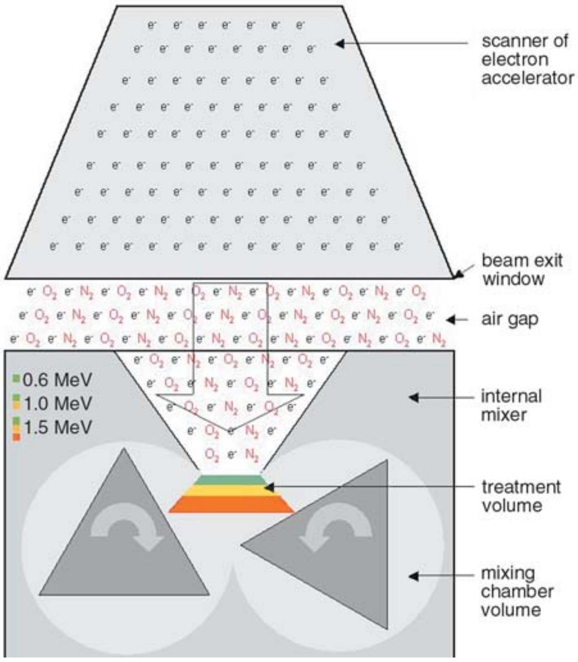

Figure 1. Schematic representation of the set-up: coupling of an electron accelerator with an internal mixer

2.3. Testing procedure

Tensile tests were carried out according to ISO 527-2/S2/50 on dumb-bell shaped specimens using an universal tensile testing machine Zwick 8195.04 at a constant cross-head speed of 50 mm/min. *E* modulus was determined in between 0.05 and 0.25% of strain. Differential scanning calorimeter (DSC) measurements were carried out using a DSC Q1000 (TA instruments, New Castle, USA). The scans were taken in the temperature range from –80 to 200°C with a programmed heating rate of 10 K/min under N_2 atmosphere. Dynamic mechanical thermal analyses (DMTA) of the samples were performed using an Eplexor 2000N DMTA (version 8.373 h) at a frequency of 10 Hz and 0.2% strain. The samples were first cooled to –80°C and then subsequently heated at a rate of 4 K/min over a range of –80 to 140°C. The tanδ peak maxima were assigned to the glass transitions (T_g) of EPDM and PP. Gel content of the samples was calculated after extracting out the PP-phase by boiling xylene. Phase morphology was investigated by a LEO 435 VP Ultra plus Scanning Electron Microscope (SEM) from Carl Zeiss SMT (Jena, Germany) after ultracutting of TPV samples at –130°C in a Leica Ultra-microtome (Wetzlar, Germany).

3. Results and discussion

3.1. Mechanical properties

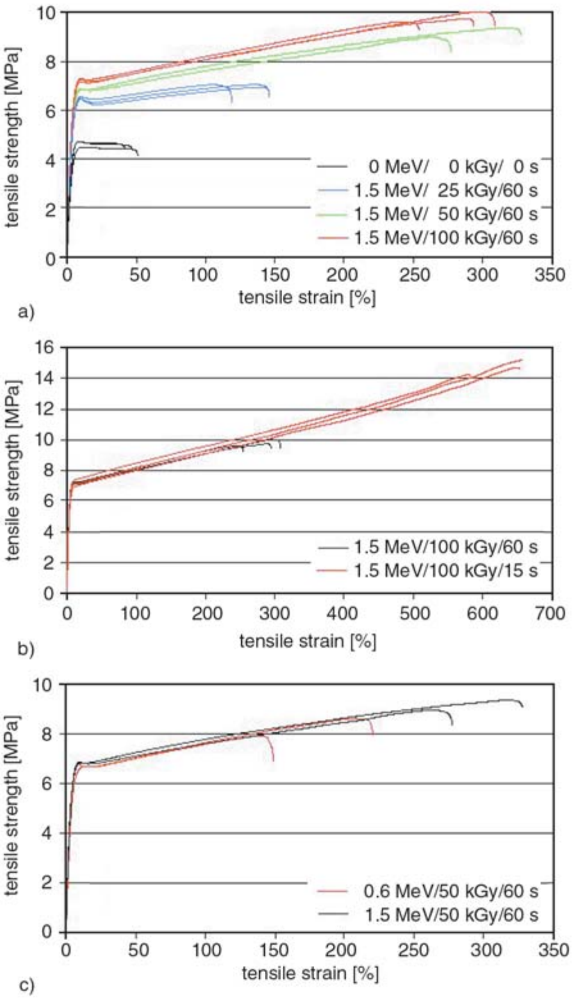

Figure 2. a) Influence of dose on tensile stress as function of tensile strain, b) influence of electron treatment time on tensile stress as function of tensile strain, c) influence of electron energy on tensile stress as function of tensile strain

Study of mechanical properties of TPVs is very important to understand the effects of electron induced reactive processing. Influence of the various conditions of this novel process on the stress-strain behavior of the PP/EPDM TPVs is shown in Figures 2a, b, and c. The experimental data of *E* modulus, tensile strength, and elongation at break as well as and their uncertainties at 96% confidence level are given in Table 1. From experimental data at 1.5 MeV and for an electron treatment of 60 s it was observed that with increasing absorbed dose from 25 to 50 kGy tensile strength, elongation at break, and *E* modulus of the TPVs were significantly improved. In case of the untreated sample tensile strength was only 4.7 ± 0.1 MPa and elongation at break was 46 ± 5%. At 50 kGy, tensile strength was 9.2 ± 0.3 MPa and elongation at break

Table 1. Experimental data of *E* modulus, tensile strength, and elongation at break

Electron energy [MeV]	Dose [kGy]	Treatment time [s]	E-modulus [MPa]	Tensile strength [MPa]	Elongation at break [%]
0.0	0	0	112 ± 12	4.7 ± 0.1	46 ± 5
1.5	25	60	159 ± 11	7.0 ± 0.1	135 ± 15
1.5	50	60	156 ± 4	9.2 ± 0.3	298 ± 35
1.5	100	60	173 ± 20	9.8 ± 0.2	282 ± 28
1.5	100	30	191 ± 8	9.5 ± 0.7	215 ± 80
1.5	100	15	176 ± 3	14.7 ± 0.5	624 ± 41
0.6	50	60	150 ± 36	8.2 ± 0.4	168 ± 42

was 298 ± 35%. Further increase in dose to 100 kGy resulted in a small increase of tensile strength to 9.8 ± 0.2 MPa where as elongation at break is kept constant (282 ± 28%). Such influence of absorbed dose has been expected from EB treatment under static conditions [19].

The experimental data at 1.5 MeV and 100 kGy showed that with decreasing electron treatment time from 60 s (16.5 kGy/s and 22 kGy per rotation) to 15 s (66 kGy/s and 88 kGy per rotation), tensile strength and elongation at break were further improved whereas *E* modulus remained constant at a level of 178 ± 2 MPa. This value is higher in comparison to the *E* modulus of untreated sample (112 ± 12 MPa). Highest tensile strength of 14.7 ± 0.5 MPa and maximum elongation at break of 624 ± 41% were recorded for an electron treatment of 15 s. Thus, electron treatment time influencing on dose rate as well as absorbed dose per rotation is an additional parameters controlling the stress-strain behavior of the PP/EPDM TPVs.

The influence of electron energy on mechanical properties was investigated at an absorbed dose of 50 kGy due to limited dose rate of electron accelerator and for an electron treatment time of 60 s. In comparison to the results at 1.5 MeV (8.2 kGy/s and $r_{vol} = 0.062$) it is seen that at 0.6 MeV (28.8 kGy/s and $r_{vol} = 0.017$) tensile strength and elongation at break were reduced whereas *E* modulus remained constant. Finally, electron energy influencing penetration depth as well as ratio of modified volume to total mixing chamber volume is controlling the stress-strain behavior of the PP/EPDM TPVs.

3.2. DSC study

Table 2 shows the experimental data of glass transition temperatures of EPDM and PP (T_g), melting temperature (T_m), crystallisation temperature ($T_{c,m}$) and melt enthalpy (ΔH). The uncertainties of melt enthalpy are related to a confidence level of 96%. Absorbed dose has an influence on both the onset of crystallisation ($T_{c,0}$) and the maximum crystallisation temperature ($T_{c,m}$) at fixed electron energy (1.5 MeV) and constant electron treatment time (60 s). For the untreated sample the value of $T_{c,m}$ was 113.5°C, where as at 25 and 100 kGy the values were increased to 123.1 and 124.8°C, respectively. This result may be explained by self-nucleation of PP in presence of irradiation, which is in line with the mechanical properties. Further, it was observed that only slight changes took place after EB treatment in the values of T_g of EPDM (at around –53°C) and PP (at around –6°C). Furthermore, no significant changes were noticed in enthalpy value (ΔH) within experimental uncertainty and melting temperature (T_m) of PP after EB treatment indicating hardly any degradation (Table 2).

In contrast to the results of stress-strain behavior, electron treatment time and electron energy have no significant influence on the heat flow curves. Thus, overall orientation, crystallisation, thickness of lamella and crosslinking are not changed.

3.3. DMTA study

It can be observed from Figure 3 that storage moduli of all the TPVs were higher than that of the untreated sample over the entire temperature range. Further, storage modulus depends on absorbed dose at fixed electron energy (1.5 MeV) and constant electron treatment time (60 s). Again, electron treatment time and electron energy have no significant influence on storage modulus of TPVs. Figure 4 illustrates the tanδ plot as function of temperature and demonstrates that there are two

Table 2. Experimental data of glass transition temperature of EPDM and PP (T_g), melting temperature (T_m), crystallisation temperature ($T_{c,m}$), and melt enthalpy (ΔH)

Electron energy [MeV]	Dose [kGy]	Treatment time [s]	T_g (EPDM) [°C]	T_g (PP) [°C]	T_m (2nd heating) [°C]	$T_{c,m}$ (1st cooling) [°C]	ΔH (2nd heating) [J/g]
0.0	0	0	–53	–7	158.6	113.5	50.8 ± 0.9
1.5	25	60	–53	–7	161.1	123.1	49.6 ± 0.6
1.5	50	60	–53	–6	160.1	124.4	48.4 ± 1.3
1.5	100	60	–53	–6	158.6	124.8	51.6 ± 1.0
1.5	100	30	–53	–6	158.3	125.0	51.6 ± 1.5
1.5	100	15	–53	–6	158.3	124.8	51.3 ± 0.9
0.6	50	60	–53	–5	160.3	124.6	49.8 ± 1.8

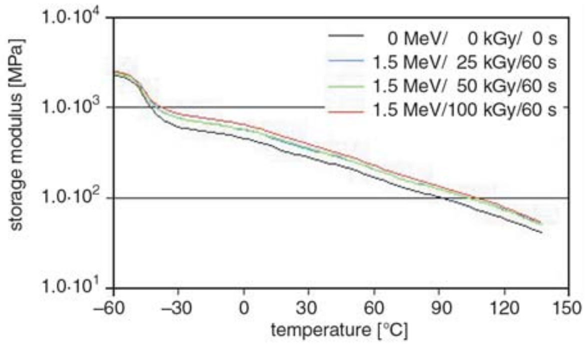

Figure 3. Influence of dose on storage modulus as a function of temperature

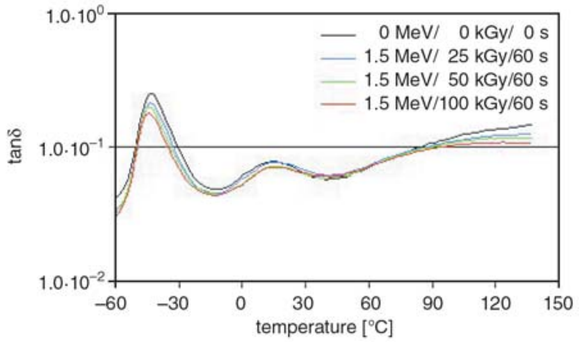

Figure 4. Influence of dose on tanδ as a function of temperature

major transitions: the T_g of EPDM at around –43°C and that of PP at around 16°C. Table 3 shows the $\tan\delta_{max}$ value at the T_g of EPDM of the TPVs at varied absorbed dose. It clearly demonstrates that the values were lowered with increasing absorbed dose indicating higher extent of cross-linking in the EPDM phase and lesser damping characteristics of the TPVs. These results were further supported by the gel content values as also shown in Table 3. With increasing dose the gel content value also increases. The gel content values were higher than the EPDM content itself in the blend which indicated high degree of cross-linking in EPDM phase and the formation of *in-situ* PP-EPDM graft-links by electron induced reactive processing. The PP-EPDM graft-links were not extractable even by boiling xylene and therefore also contribute to the gel contents.

Electron treatment time and electron energy have no significant influence on storage modulus and on the tanδ values. Thus, viscous and elastic properties of PP-EPDM TPVs were not changed.

3.4. Morphology

TPVs are characterised by its typical dispersed phase morphology, where cross-linked rubber particles are dispersed in a continuous matrix of thermoplastic. In general, the smaller the particle size, the better the mechanical properties. Figures 5a, b, and c illustrate SEM photomicrographs of various PP-EPDM blends: both untreated and treated under various conditions. In all cases, a wide distribution of particle sizes is generated due to the mixing under dynamic conditions. It can be seen from the micrographs that for the untreated sample, the particle sizes were much bigger (around 2–3 μm). Electron induced reactive processing at 1.5 MeV, 100 kGy, and 60 s results in smaller EPDM particle size (even to 0.2 μm) indicating better dispersion due to the dynamic vulcanisation. The smallest EPDM particle sizes (around 0.04 μm) were recorded in case of 100 kGy absorbed dose and 15 s electron treatment time (Figure 5c) at 1.5 MeV, which is in line with the mechanical properties.

4. Conclusions

Thermoplastic vulcanisates (TPVs) were prepared by dynamic vulcanisation with 50:50 blend ratio of PP and EPDM using novel electron induced reactive processing under various conditions as an alternative to conventional phenolic resin and peroxide cross-linking systems. The adhesion between the dispersed EPDM particles and PP matrix plays a very important role governing the deformation behavior of the TPVs. It can be concluded that electron induced reactive processing with 1.5 MeV electrons for 15 s at an absorbed dose of 50 kGy should give best balance of mechanical properties for our experimental setup.

Table 3. $\tan\delta_{max}$ and gel content of various PP-EPDM TPVs

Electron energy [MeV]	Dose [kGy]	Treatment time [s]	tanδ peak value (EPDM)	Gel content [%]
0.0	0	0	0.249	0.0
1.5	25	60	0.213	54.5
1.5	50	60	0.201	64.0
1.5	100	60	0.180	65.0

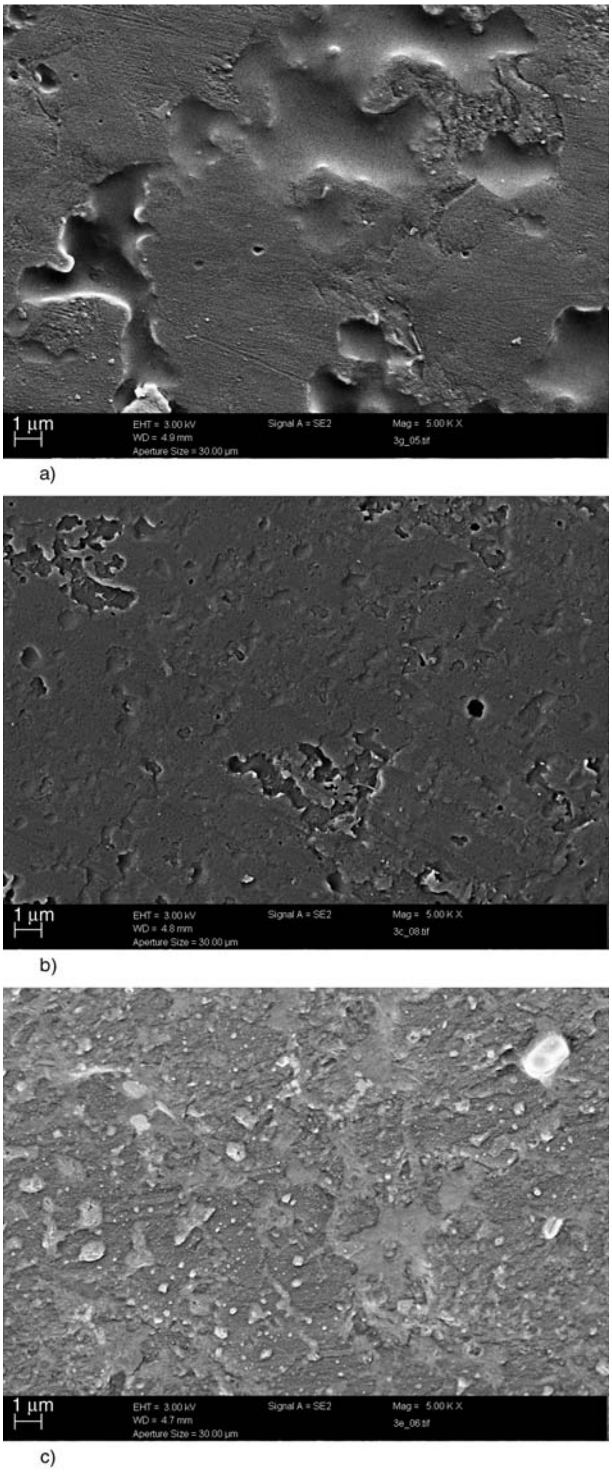

Figure 5. a) SEM photomicrograph of sample: 0 MeV, 0 kGy, b) SEM photomicrograph of sample: 1.5 MeV, 100 kGy for 60 s, c) SEM photomicrograph of sample: 1.5 MeV, 100 kGy for 15 s

The experimental results clearly indicated that two processes are simultaneously occurring contributing to enhancement in the mechanical properties: (a) *in-situ* compatibilisation of PP and EPDM and (b) cross-linking in the EPDM phase. Both processes do not only depend on absorbed dose like in traditional electron treatment under static conditions. Moreover, they depend on electron treatment time as well as electron energy. Electron treatment time correlates with dose rate and radical generation rate. Thus we can conclude that radical generation rate of electron induced reactive processing controls structure, morphology and properties of PP-EPDM vulcanisate at fixed mixing rate and fixed mixing temperature range. An influence of reaction rate in relation to mixing rate was already reported by Msakni *et al.* [20] for cross-linking of ethylene-octene copolymers by peroxide under dynamic conditions.

Further experiments are required to investigate the role of absorbed dose per rotation and electron energy in electron induced reactive processing of PP-EPDM-vulcanisate as well as to understand the mechanism of electron induced reactive processing resulting in the observed experimental data.

Acknowledgements

K. Naskar is thankful to Alexander von Humboldt Foundation, Germany, for the financial assistance.

References

[1] Legge N. R., Holden G., Schroeders H. E.: Thermoplastic elastomer: A comprehensive review. Hanser, Munich (1987).

[2] De S. K., Bhowmick A. K.: Thermoplastic elastomers from rubber plastic blends. Horwood, London, (1990).

[3] Gessler A. M., Haslett W. H.: Process for preparing a vulcanised blend of crystalline polypropylene and chlorinated butyl rubber. US Patent 3037954, USA (1962).

[4] Coran A. Y., Patel R. P.: Rubber-thermoplastic compositions. Part I. EPDM-polypropylene thermoplastic vulcanisates. Rubber Chemistry and Technology, **53**, 141–150 (1980).

[5] Karger-Kocsis J.: Thermoplastic rubbers via dynamic vulcanisation. in ‘Polymer blends and alloys’ (eds.: Shonaike G. O., Simon G. P.) Marcel Dekker, New York, 125–153 (1999).

[6] Abdou-Sabet S., Fath M. A.: Thermoplastic elastomer blends of olefin rubber and polyolefin resin. US Patent 4311628, USA (1982).

[7] Abdou-Sabet S., Patel R. P.: Morphology of elastomeric alloys. Rubber Chemistry and Technology, **64**, 769–779 (1991).

[8] Ilisch S., Menge H., Radusch H-J.: Vernetzungsausbeute an konventionellen und dynamischen Vulkanisaten. Kautschuk und Gummi Kunststoffe, **53**, 206–212 (2000).

[9] Naskar K., Noordermeer J. W. M.: Dynamically vulcanised PP/EPDM blends-effects of different types of peroxides on the properties. Rubber Chemistry and Technology, **76**, 1001–1018 (2003).

[10] Naskar K., Noordermeer J. W. M.: Dynamically vulcanized PP/EPDM blends-effects of multifunctional peroxides as crosslinking agents. Rubber Chemistry and Technology, **77**, 955–971 (2004).

[11] Naskar K.: Thermoplastic elastomer based on PP/EPDM blends by Dynamic vulcanization – A review. Rubber Chemistry and Technology, **80**, 504–510 (2007).

[12] Chatterjee K., Naskar K.: Development of thermoplastic elastomers based on maleated ethylene propylene rubber (m-EPDM) and polypropylene (PP) by dynamic vulcanisation. Express Polymer Letters, **1**, 527–534 (2007).
DOI: 10.3144/expresspolymlett.2007.75

[13] Dole M.: Cross-unking and crystallinity in irradiated polypropylene. Polymer Plastic Technology and Engineering, **13**, 41–64 (1979).
DOI: 10.1080/03602557908067674

[14] Zaharah A. K., Yoshii F., Makuuchi K., Ishikaki I.: Durability of radiation-sterilised polymers: 12. The effects of nucleating agent on the oxidative degradation of polypropylene. Polymer, **30**, 1425–1432 (1989).
DOI: 10.1016/0032-3861(89)90211-5

[15] Yoshii F., Meligi G., Sasaki T., Makuuchi K., Rabei A. M., Nishimato S.: Effects of irradiation on the degradability of polypropylene in the natural environment. Polymer Degradation and Stability, **49**, 315–321 (1995).

[16] Schulze U., Majumder P. S., Heinrich G., Stephan M., Gohs U.: Electron beam crosslinking of atactic polypropylene: development of a potential novel elastomer. Macromolecular Materials and Engineering, **293**, 692–699 (2008).
DOI: 10.1002/mame.200800093

[17] Majumder P. S., Bhowmick A. K.: Surface and bulk properties of EPDM rubber modified by electron beam irradiation. Radiation Physics and Chemistry, **53**, 63–78 (1999).
DOI: 10.1016/S0969-806X(97)00296-X

[18] Majumder P. S., Bhowmick A. K.: Friction behaviour of electron beam modified ethylene propylene diene monomer rubber surface. Wear, **221**, 15–23 (1998).
DOI: 10.1016/S0043-1648(98)00255-5

[19] Khan M. S., Lehmann D., Heinrich G., Gohs U., Franke R.: Structure-property effects on mechanical, friction and wear properties of electron modified PTFE filled EPDM composite. Express Polymer Letters, **3**, 39–48 (2009).
DOI: 10.3144/expresspolymlett.2009.7

[20] Msakni A., Chaumont P., Cassagnau P.: Cross-linking of ethylene-octene copolymers by peroxide under static and dynamic conditions. Polymer Engineering and Science, **46**, 1530–1540 (2006).
DOI: 10.1002/pen.20618

eXPRESS Polymer Letters Vol.3, No.11 (2009) 684–691
Available online at www.expresspolymlett.com
DOI: 10.3144/expresspolymlett.2009.86

Theoretical investigations on the geometric and electronic structures of polyacetylene molecule under the influence of external electric field

Y. W. Li[1,2*], *J. H. Yao*[1], *X. D. Zhu*[3], *C. J. Liu*[1,2], *J. Q. Jiang*[1], *X. S. Deng*[1]

[1]Key Laboratory of New Processing Technology for Nonferrous Metals and Materials, Ministry of Education, Guilin University of Technology, Guilin 541004, PR. China
[2]Department of Material and Chemical Engineering, Guilin University of Technology, Guilin 541004, P.R. China
[3]Department of Applied Chemistry, Harbin Institute of Technology, Harbin, 150001, PR China

Received 12 July 2009; accepted in revised form 13 August 2009

Abstract. The geometric and electronic structures of all-trans polyacetylene (PA) molecule in neutral, cationic, and anionic states have been studied theoretically by density functional theory method at the B3LYP/6-31+G* level. The results show that both the geometric and electronic structures of the PA molecule are sensitive to the external electric field (EF). For neutral PA molecule, with the increase of EF, the carbon-carbon single bonds are shortened while the carbon-carbon double bonds are elongated. The energy gap between the highest occupied molecular orbital and the lowest unoccupied molecular orbital (LUMO-HOMO gap) decreases with the EF increasing. For cationic PA molecule, the carbon-carbon single bonds and carbon-carbon double bonds on the high potential side are elongated and shortened, respectively. While, the carbon-carbon single bonds and carbon-carbon double bonds on the low potential side are shortened and elongated, respectively. Contrary to the neutral PA case, the LUMO-HOMO gap increases with the EF increasing. Contrast to the case of cationic PA, the evolution of carbon-carbon bond lengths for the anionic PA molecule under the external EF reverses. The LUMO-HOMO gap of the anionic PA molecule decreases with the increase of external EF. In addition, the spatial distributions of the HOMO and LUMO under the influence of external EF are also discussed for the PA molecule in neutral, cationic, and anionic states.

Keywords: *modeling and simulation, density functional theory, polyacetylene, electronic structure, geometric structure*

1. Introduction

π-conjugated polymers are the subject of recent fundamental and industrial research due to their novel properties and a variety of applications in the electronic devices, such as light-emitting diodes (LED) [1, 2], field-effect transistors (FET) [3, 4], and molecular electronic devices [5, 6]. The characteristic feature of all these substances is the conjugated double bond. Among these conjugated polymers, all-trans polyacetylene (PA) is the most prominent representative of this kind of material, and many other conjugated polymers can, in principle, derived by the structure modification. Therefore, it has been studied intensively both experimentally [7–9] and theoretically [10–12].

Previous works [13–15] demonstrated that the properties of these polymers are critically dependent on the geometric and electronic structures of the molecules. Therefore, knowledge about these characters of the conjugated molecules is highly desired not only for understanding the packing model of molecules in solid, but also for designing or ration-

---

*Corresponding author, e-mail: lywhit@glite.edu.cn

alizing electronic devices. Although much information of the properties for this kind of materials has been obtained with the assistance of nuclear magnetic resonance (NMR) [16], X-ray analysis [17], and scanning tunneling microscopic (STM) investigation [18], the details of the molecular geometric and electronic structures as well as the structure/properties relationships are not very clear. Electric conductance is a bulk property. However, it does indeed take place over the single molecules [19]. Moreover, conjugated molecules are promising materials for electronic devices [1–6, 20], in which the molecules undergo a large external electric field (EF). Thus, in order to study, and eventually to be able to predict, electrical conduction of polymers made from organic monomers, it is important to understand the nature of the molecular response to an external EF both for neutral and charged species. However, there is no systematic report on these issues yet. The purpose of this work is to perform theoretical investigations on the evolution of the geometric and electronic structures of PA molecule in neutral and charged states by considering the influence of external EF.

2. Methods

Previous theoretical investigations of conjugated molecules have demonstrated the significance of correlation effects [21, 22]. In order to perform an accurate calculation on the geometric and electronic properties of a conjugated molecule, the computation of electron correlation effects by many-body perturbation theory should be carried out after the Hartree-Fock (HF) calculation. Alternatively, we can do density functional theory (DFT) calculation, in which the electron correlation is taken account. In the present work, all the calculations are performed at the B3LYP level with 6-31+G* basis set, which is widely used for calculations for conjugated molecules [22, 23], by using the GAUSSIAN 03 program [24].

Theoretical modeling has been achieved as follows. Prior to the introduction of EF, linear chain of all-trans PA (see Figure 1) was fully optimized at the B3LYP/6-31+G* level for both the neutral and charged states. All the geometric parameters were, then, optimized at the same level of theory in the application of uniform external EF. A uniform EF ranging from *zero* to $2.57 \cdot 10^9$ V·m^{-1} and aligned along the two terminal carbon-carbon inter-atomic vector was applied to the model molecules (see Figure 1), which may reasonably represent the working condition of organic electronic devices [19, 25].

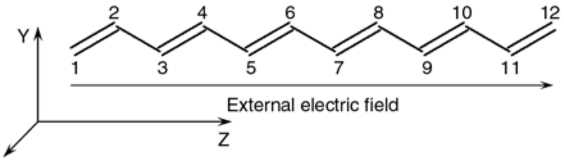

Figure 1. Scheme of the polyacetylene molecule studied in the present work. The external EF is aligned along the two terminal carbon-carbon inter-atomic vector C1–C12.

3. Results and discussion

3.1. EF effect on the geometric structure

The equilibrium geometries of the neutral and charged all-trans PA without EF (*zero* EF) show a coplanar conformation with C_{2h} symmetry as expected. The carbon-carbon bond lengths along the backbone is one of the most crucial parameters in determining molecular properties, such as static electronic polarizability, second hyperpolarizability [26], nonlinear optical property [27], and the energy gap between the highest occupied molecular orbital (HOMO) and the lowest unoccupied molecular orbital (LUMO) (abbreviated as LUMO-HOMO gap) in the conjugated molecules [28]. Figure 2 presents the bond lengths of the model PA in neutral state, cationic state, and anionic state. It

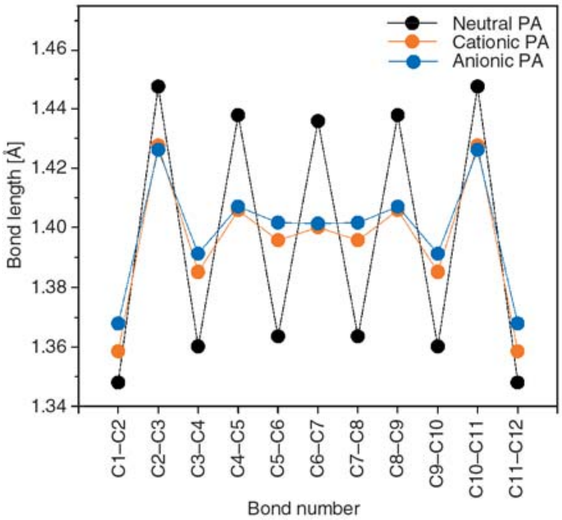

Figure 2. The bond lengths of PA molecule in neutral state, cationic state, and anionic state as a function of bond number (see chemical structures in Figure 1 for bond codes)

can be seen that the neutral PA shows biggest bond length alternation (BLA, the average of the difference in the length between the adjacent carbon-carbon bonds in the polyacetylene). When the PA gets charged, the BLA is decreased dramatically. In addition, the BLA of the anionic PA is somewhat smaller than that of the cationic PA. The carbon-carbon bond length is predominated not only by the nature of the molecule, but also the surroundings. Especially, when a considerable EF is applied, the carbon-carbon bond length is expected to vary [29]. In order to study, and eventually to be able to predict the properties of the conjugated molecule, it is important to understand how the carbon-carbon bond length responds to the external EF.

After the application of EF, the molecular symmetry is destroyed, although the coplanar conformation remains. Figure 3 gives the evolution of the bond length with respect to that of *zero* EF for the model molecule (see Figure 1) in neutral state. When EF increases, the carbon-carbon single bonds become shorter and the double bonds become longer, resulting in a decreased BLA. Similar result has also been observed for other conjugated molecules, such as polythiophene and oligo(phenylene ethylene), as reported by us [30, 31]. However, the EF dependence of the bond length is not identical for all the bonds. The bonds on the high potential side show more deviation than those on the low potential side of the model molecule. In addition, the maximum deviation occurs in the central part for both the single and double bonds due to the chain end effect [29] and the better conjugation as compared to those toward the end of the molecule.

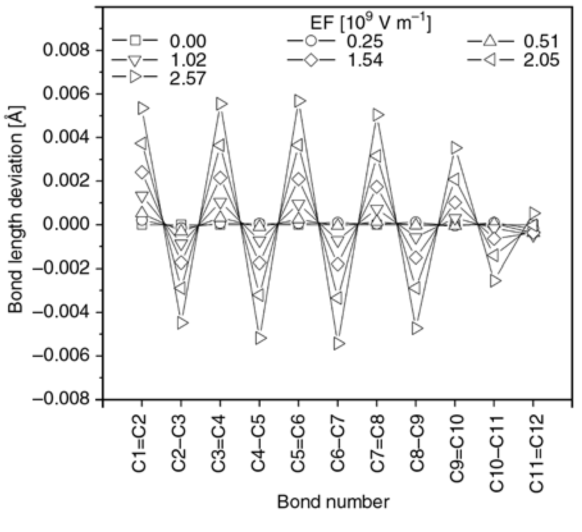

Figure 3. Geometric deviation of the bond lengths of neutral PA molecule under various external EF (see chemical structures in Figure 1 for bond codes). The bond lengths under *zero* EF are referred to as *zero*.

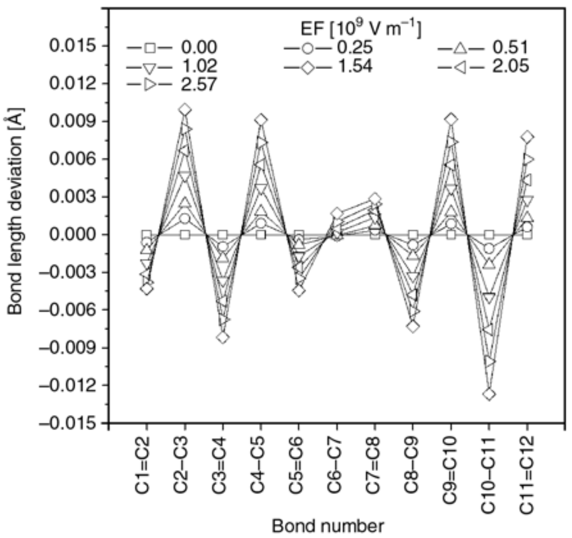

Figure 4. Geometric deviation of the bond lengths of cationic PA molecule under various external EF (see chemical structures in Figure 1 for bond codes). The bond lengths under *zero* EF are referred to as *zero*.

When the molecules are under nonequilibrium conditions, the electronic state would be different and accordingly it is essential to investigate the charged state. Figure 4 presents the evolution of bond length with respect to that of *zero* EF for the model molecule in cationic state. When EF is introduced, all the bond lengths change. However, the bond length evolution is very different from that observed for the neutral PA. With the EF increasing, the single bonds and double bonds on the high potential side get longer and shorter, respectively; while the single bonds and double bonds on the low potential side get shorter and longer, respectively. Therefore, the application of external EF weakens the conjugation of the high potential side of the molecule and strengthens the conjugation of the low potential side of the molecule. Contrary to the case of neutral PA, the bonds in the central part of cationic PA exhibit minimum bond length deviation. Figure 5 shows the evolution of bond length with respect to that of *zero* EF for the model molecule in anionic state. In contrast to the case of cationic state, for the anionic PA, with the EF increasing, the single bonds and double bonds on the high potential side get shorter and longer, respectively; while the single bonds and double bonds on the low potential side get longer and

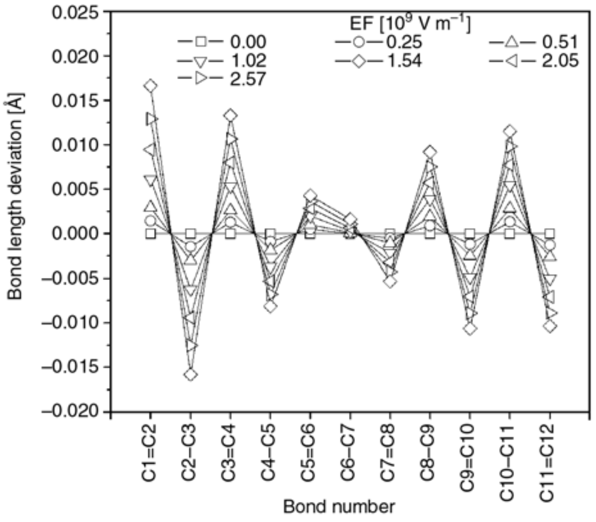

Figure 5. Geometric deviation of the bond lengths of anionic PA molecule under various external EF (see chemical structures in Figure 1 for bond codes). The bond lengths under *zero* EF are referred to as *zero*.

shorter, respectively. Thus, the application of external EF strengths the conjugation of the high potential side of the molecule and weakens the conjugation of the low potential side of the molecule. Similar to the case of cationic PA, the bonds in the central part of the anionic PA exhibits minimum bond length deviation.

3.2. EF effect on the electronic structure

The energy levels of the molecular orbitals, especially the HOMO and LUMO, are excellent indicators of many molecular properties, such as chemical activity [32] and electrical performance [33]. Figure 6a gives the HOMO and LUMO levels for the model PA in neutral state calculated by B3LYP/6-31+G* method. It can be seen that with the increase of EF, both the energy levels of HOMO and LUMO decrease. When the EF increases from *zero* to $2.57 \cdot 10^9$ V·m^{-1}, the HOMO and LUMO are decreased by 1.66 and 1.90 eV, respectively. Figure 6b illustrates the LUMO-HOMO gap of the model PA in neutral state. Under *zero* EF, the LUMO-HOMO gap is 2.93 eV. With the EF increasing, the LUMO-HOMO gap decreases. By detailed analysis, it is interesting to find that the LUMO-HOMO gap decreases linearly with the square of EF (see the inset in Figure 6b). Figure 7a shows the HOMO and LUMO levels for the model PA in cationic state calculated by B3LYP/6-31+G* method. Similar to that of neutral case, with the EF increasing, both the HOMO and LUMO decrease. When the EF increases from *zero* to $2.57 \cdot 10^9$ V·m^{-1}, the decrements of HOMO and LUMO are 1.74 and 1.67 eV, respectively. Figure 7b gives LUMO-HOMO gap of the model PA in cationic state. Under *zero* EF, the LUMO-HOMO gap is 2.58 eV, which is 0.35 eV lower than that of the neutral PA. Contrary to the case of neutral PA, with the EF increasing, the LUMO-HOMO gap of the cationic PA increases. A linear relationship between the LUMO-HOMO gap and the square of EF is also observed for the cationic PA (see the inset in Figure 7b). Figure 8a presents HOMO and LUMO levels for the model PA in anionic state calculated by B3LYP/6-31+G* method. With the EF increasing, both the HOMO and LUMO decreases. When the EF increases from *zero* to $2.57 \cdot 10^9$ V·m^{-1}, the decrements of HOMO

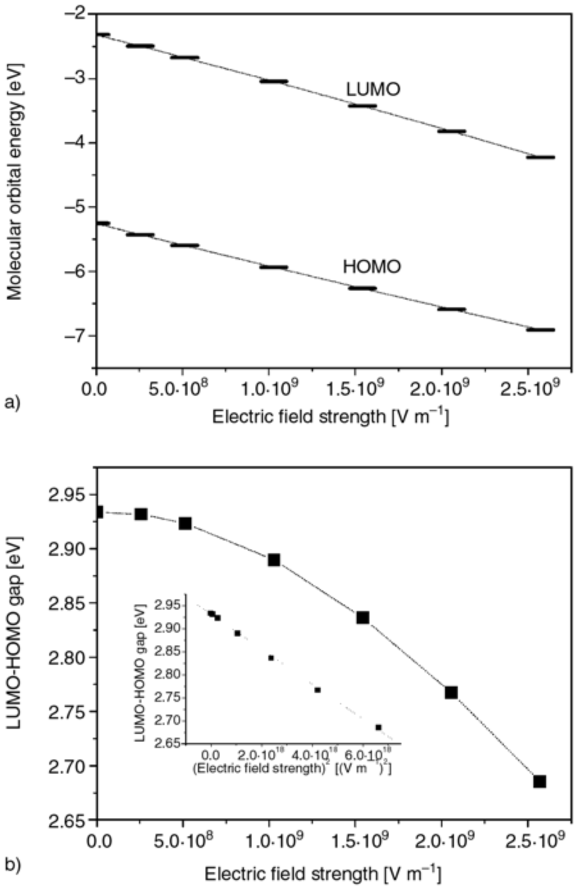

Figure 6. (a) LUMO and HOMO energies for the neutral PA molecule under various external EF; (b) LUMO-HOMO gap for the neutral PA molecule under various external EF. The inset shows the linear relationship of the LUMO-HOMO gap and the square of EF.

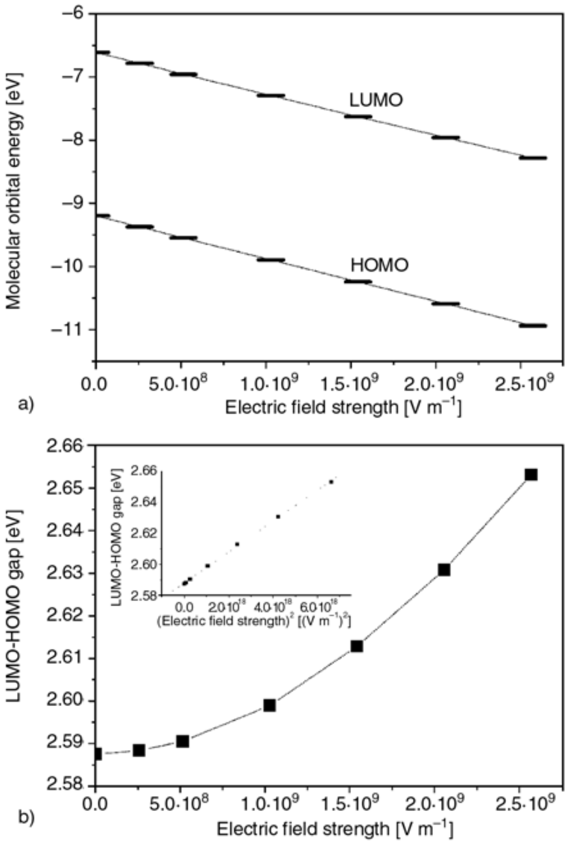

Figure 7. (a) LUMO and HOMO energies for the cationic PA molecule under various external EF; (b) LUMO-HOMO gap for the cationic PA molecule under various external EF. The inset shows the linear relationship of the LUMO-HOMO gap and the square of EF.

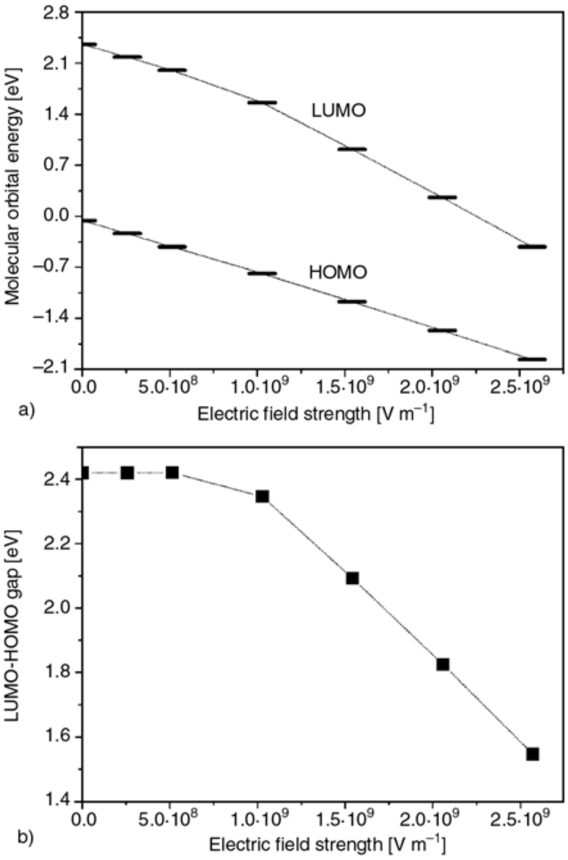

Figure 8. (a) LUMO and HOMO energies for the anionic PA molecule under various external EF; (b) LUMO-HOMO gap for the anionic PA molecule under various external EF

and LUMO are 1.91 and 1.94 eV, respectively. Figure 8b gives LUMO-HOMO gap of the model PA in anionic state. Under *zero* EF, the LUMO-HOMO gap is 2.42 eV, which is 0.16 and 0.51 eV lower than that of the neutral PA and cationic PA, respectively. When EF is less than $0.51\cdot10^9$ V·m^{-1}, the LUMO-HOMO gap seems not sensitive to the charges of EF. However, when the EF is higher than $0.51\cdot10^9$ V·m^{-1}, the LUMO-HOMO gap decreases dramatically. When EF increases from $1.02\cdot10^9$ to $2.57\cdot10^9$ V·m^{-1}, the LUMO-HOMO gap almost decreases linearly with the increase of EF. Compared to the cases of the neutral PA and cationic PA, the distortion of the linear relationship between the LUMO-HOMO gap and the square of EF for the anionic PA is possibly caused by the enhanced electron interaction from the additional electron.

Other than the energy levels of the molecular orbitals, one way to understand the molecular properties is to analyze the spatial distribution of frontier orbitals [34]. Table 1 compares the spatial distribution of the HOMO and LUMO for the model PA in neutral, cationic, and anionic states under various EF. At *zero* EF, both the HOMO and LUMO for the PA in neutral and charged states are fully delocalized on the whole molecular backbone. For the neutral PA, the introduction of EF tends to move the HOMO to the low potential side and the LUMO to the high potential side. Similar result has also been observed for other conjugated molecules, such as polythiophene and oligo(phenylene ethylene), as reported by us [30, 31]. While for the cationic PA, both the HOMO and LUMO are almost unchanged with the application of EF. For the anionic PA, the HOMO tends to shift to high potential side with the increasing of EF; The LUMO almost remains when the EF is less than $0.51\cdot10^9$ V·m^{-1}. However, further increasing EF leads the LUMO practically localize on the high potential end of the molecule.

Table 1. Spatial distribution of HOMO and LUMO of the PA in neutral state, cationic state, and anionic state under various EF

EF 10^9 [V·m^{-1}]	Neutral PA		Cationic PA		Anionic PA	
	HOMO	LUMO	HOMO	LUMO	HOMO	LUMO
0.00						
0.51						
1.54						
2.57						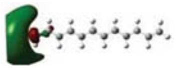

4. Conclusions

B3LYP/6-31+G* calculations are performed to study the geometric and electronic characters of all-trans polyacetylene (PA) molecule in neutral, cationic, and anionic states under the influence of external electric field (EF). For neutral PA molecule, the carbon-carbon single bonds are shortened while the carbon-carbon double bonds are elongated with the EF increasing. The energy gap between the HOMO and LUMO is decreased with the interlocution of the external EF. For cationic PA molecule, the carbon-carbon single bonds and carbon-carbon double bonds on the low potential side are elongated and shortened, respectively. While, the evolution of carbon-carbon bond length on the high potential side reverses. Contrary to the neutral PA case, with the increase of EF, the LUMO-HOMO gap increases. When compared to the case of cationic PA, the evolution of carbon-carbon bond length of the anionic PA molecule under the external EF reverses. The LUMO-HOMO gap of the anionic PA molecule decreases with the increase of the external EF. Under *zero* EF, both the HOMO and LUMO of all-trans PA molecule in neutral, cationic, and anionic states are delocalized on the whole molecular backbone. Under the influence of external EF, the HOMO and LUMO for the neutral PA slightly shift to low potential side and high potential side, respectively. The introduction of EF has almost no effect on the spatial distribution of the HOMO and LUMO of the cationic PA. With the application of external EF, both the HOMO and LUMO of anionic PA shift to high potential side. In particular, under certain EF the LUMO of anionic PA practically localized on the high potential end of the molecule.

Acknowledgements

We gratefully acknowledge the financial support of Guangxi Natural Science Foundation (No. 0991247), Guangxi Science Research and Technology Developing Foundation of China (No. 0842003-15) and Talent Development Foundation of Guilin University of Technology (No. 006206236).

References

[1] Friend R. H., Gymer R. W., Holmes A. B., Burroughes J. H., Marks R. N., Taliani C., Bradley D. D. C., Dos Santos D. A., Brédas J. L., Lögdlund M., Salaneck W. R.: Electroluminescence in conjugated polymers. Nature, **397**, 121–128 (1999).
DOI: 10.1038/16393

[2] Garcia A., Yang R., Jin Y., Walker B., Nguyen T.: Structure-function relationships of conjugated polyelectrolyte electron injection layers in polymer light emitting diodes. Applied Physics Letters, **91**, 153502/1–153502/3 (2007).
DOI: 10.1063/1.2794422

[3] Horowitz G.: Organic field-effect transistors. Advanced Materials, **5**, 365–377 (1998).
DOI: 10.1002/(SICI)1521-4095(199803)10:5<365::AID-ADMA365>3.0.CO;2-U

[4] Sun Y., Liu Y., Zhu D.: Advances in organic field-effect transistors. Journal of Materials Chemistry, **15**, 53–65 (2005).
DOI: 10.1039/b411245h

[5] Akkerman H. B., Blom P. W. M., Leeuw D. M., Boer B.: Towards molecular electronics with large-area molecular junctions. Nature, **441**, 69–72 (2006).
DOI: 10.1038/nature04699

[6] Li Y., Yao J., Liu C., Yang C.: Theoretical investigation on electron transport properties of a single molecular diode. Journal of Molecular Structure: THEOCHEM, **867**, 59–63 (2008).
DOI: 10.1016/j.theochem.2008.07.026

[7] Shirakawa H.: The discovery of polyacetylene film: The dawning of an era of conducting polymers. Synthesis Metals, **125**, 3–10 (2001).
DOI: 10.1016/S0379-6779(01)00507-0

[8] Roth S., Filzmoser M.: Conducting polymers-thirteen years of Polyacetylene Doping. Advanced Materials, **21**, 356–360 (2004).
DOI: 10.1002/adma.19900020804

[9] Lam J. W. Y., Luo J., Dong Y., Cheuk K. K. L., Tang B. Z.: Functional polyacetylenes: Synthesis, thermal stability, liquid crystallinity, and light emission of polypropiolates. Macromolecules, **35**, 8288–8299 (2002).
DOI: 10.1021/ma021011a

[10] Pino R., Scuseria G. E.: Importance of chain-chain interactions on the band gap of *trans*-polyacetylene as predicted by second-order perturbation theory. Journal of Chemical Physics, **121**, 8113–8119 (2004).
DOI: 10.1063/1.1798991

[11] Ciofini I., Adamo C., Chermette H.: Effect of self-interaction error in the evaluation of the bond length alternation in trans-polyacetylene using density-functional theory. Journal of Chemical Physics, **123**, 121102/1–121102/4 (2005).
DOI: 10.1063/1.2047447

[12] Champagne B., Spassova M.: Structural properties of doped polyacetylene chains: A comparative theoretical investigation using Hartree-Fock, Moller-Plesset second-order perturbation theory, and density functional theory approaches. Physical Chemistry Chemical Physics, **6**, 3167–3174 (2004).
DOI: 10.1039/b402635g

[13] Brédas J. L.: Molecular geometry and nonlinear optics. Science, **263**, 487–488 (1994).
DOI: 10.1126/science.263.5146.487

[14] Kertész M., Choi C. H., Yang S.: Conjugated polymers and aromaticity. Chemical Reviews, **105**, 3448–3481 (2005).
DOI: 10.1021/cr990357p

[15] Bundgaard E., Krebs F. C.: Low-band-gap conjugated polymers based on thiophene, benzothiadiazole, and benzobis(thiadiazole). Macromolecules, **39**, 2823–2831 (2006).
DOI: 10.1021/ma052683e

[16] Tang R., Tan Z., Li Y., Xi F.: Synthesis of new conjugated polyfluorene derivatives bearing triphenylamine moiety through a vinylene bridge and their stable blue electroluminescence. Chemistry of Materials, **18**, 1053–1061 (2006).
DOI: 10.1021/cm0522735

[17] Hou J., Huo L., He C., Yang C., Li Y.: Synthesis and absorption spectra of poly(3-(phenylenevinyl)thiophene)s with conjugated side chains. Macromolecules, **39**, 594–603 (2006).
DOI: 10.1021/ma051883n

[18] Sakaguchi H., Matsumura H., Gong H., Abouelwafa A. M.: Direct visualization of the formation of single-molecule conjugated copolymers. Science, **310**, 1002–1006 (2005).
DOI: 10.1126/science.1117990

[19] Chen F., Hihath J., Huang Z., Li X., Tao N. J.: Measurement of single-molecule conductance. The Annual Review of Physical Chemistry, **58**, 535–564 (2007).
DOI: 10.1146/annurev.physchem.58.032806.104523

[20] Stan M. R., Franzon P. D., Goldstein S. C., Lach J. C., Ziegler M. M.: Molecular electronics: From devices and interconnect to circuits and architecture. Proceedings of the IEEE, **91**, 1940–1957 (2003).
DOI: 10.1109/JPROC.2003.818327

[21] Torrent-Sucarrat M., Sola M., Duran M., Luis J. M.: Basis set and electron correlation effects on ab initio electronic and vibrational nonlinear optical properties of conjugated organic molecules. Journal of Chemical Physics, **118**, 711–718 (2003).
DOI: 10.1063/1.1521725

[22] Jacquemin D., Perpete E. A., Ciofini I., Adamo C.: Assessment of recently developed density functional approaches for the evaluation of the bond length alternation in polyacetylene. Chemical Physics Letters, **405**, 376–381 (2005).
DOI: 10.1016/j.cplett.2005.02.037

[23] Li Y. W., Zhang Y., Yin G. P., Zhao J. W.: Theoretical investigations on molecular conducting wire under electric field. Chemical Journal of Chinese Universities, **27**, 292–296 (2006).

[24] Frisch M. J., Trucks G. W., Schlegel H. B., Scuseria G. E., Robb M. A., Cheeseman J. R., Montgomery J. A., Vreven Jr., T., Kudin K. N., Burant J. C., Millam J. M., Iyengar S. S., Tomasi J., Barone V., Mennucci B., Cossi M., Scalmani G., Rega N., Petersson G. A., Nakatsuji H., Hada M., Ehara M., Toyota K., Fukuda R., Hasegawa J., Ishida M., Nakajima T., Honda Y., Kitao O., Nakai H., Klene M., Li X., Knox J. E., Hratchian H. P., Cross J. B., Adamo C., Jaramillo J., Gomperts R., Stratmann R. E., Yazyev O., Austin A. J., Cammi R., Pomelli C., Ochterski J. W., Ayala P. Y., Morokuma K., Voth G. A., Salvador P., Dannenberg J. J., Zakrzewski V. G., Dapprich S., Daniels A. D., Strain M. C., Farkas O., Malick D. K., Rabuck A. D., Raghavachari K., Foresman J. B., Ortiz J. V., Cui Q., Baboul A. G., Clifford S., Cioslowski J., Stefanov B. B., Liu G., Liashenko A., Piskorz P., Komaromi I., Martin R. L., Fox D. J., Keith T., Al-Laham M. A., Peng C. Y., Nanayakkara A., Challacombe M., Gill P. M. W., Johnson B., Chen W., Wong M. W., Gonzalez C., Pople J. A.: Gaussian 03, Revision C.02, Gaussian, Inc., Wallingford, USA (2004).

[25] Schön J. H., Meng H., Bao Z.: Field-effect modulation of the conductance of single molecules. Science, **294**, 2138–2140 (2001).
DOI: 10.1126/science.1066171

[26] Champagne B., Perpete E. A.: Bond length alternation effects on the static electronic polarizability and second hyperpolarizability of polyacetylene chains. International Journal of Quantum Chemistry, **75**, 441–447 (1999).
DOI: 10.1002/(SICI)1097-461X(1999)75:4/5<441::AID-QUA10>3.0.CO;2-B

[27] Marder S. R., Gorman C. B., Tiemann B. G., Perry J. W., Bourhill G., Mansour K.: Relation between bond-length alternation and second electronic hyperpolarizability of conjugated organic molecules. Science, **261**, 186–189 (1993).
DOI: 10.1126/science.261.5118.186

[28] Brisset H., Blanchard P., Illien B., Riou A., Roncali J.: Bandgap control through reduction of bond length alternation in bridged poly(diethienylethylene)s. Chemical Communications, 569–570 (1997).
DOI: 10.1039/a607890g

[29] Champagne B., Deumens E., Öhrn Y.: Vibrations and soliton dynamics of positively charged polyacetylene chains. The Journal of Chemical Physics, **107**, 5433–5444 (1997).
DOI: 10.1063/1.474249

[30] Zhang Y., Ye Y., Li Y., Yin X., Liu H., Zhao J.: Ab initio investigations of quaterthiophene molecular wire under the interaction of external electric field. Journal of Molecular Structure: THEOCHEM, **802**, 53–58 (2007).
DOI: 10.1016/j.theochem.2006.09.012

[31] Li Y., Zhao J., Yin G.: Theoretical investigations of oligo(phenylene ethylene) molecular wire: Effects from substituents and external electric field. Computational Materials Science, **39**, 775–781 (2007).
DOI: 10.1016/j.commatsci.2006.09.010

[32] Aihara J.: Correlation found between the HOMO-LUMO energy separation and the chemical reactivity at the most reactive site for isolated-pentagon isomers of fullerenes. Physical Chemistry Chemical Physics, **2**, 3121–3125 (2000).
DOI: 10.1039/b002601h

[33] Singh T. B., Sariciftci N. S.: Progress in plastic electronics devices. Annual Review of Materials Research, **36**, 199–230 (2006).
DOI: 10.1146/annurev.matsci.36.022805.094757

[34] Li Y., Zhao J., Yin X., Liu H., Yin G.: Conformational analysis of diphenylacetylene under the influence of an external electric field. Physical Chemistry Chemical Physics, **9**, 1186–1193 (2007).
DOI: 10.1039/b615618e

eXPRESS Polymer Letters Vol.3, No.11 (2009) 692–702
Available online at www.expresspolymlett.com
DOI: 10.3144/expresspolymlett.2009.87

Kinetics of structure formation in PP/layered silicate nanocomposites

J. Hári[1,2], *Z. Dominkovics*[1,2], *E. Fekete*[1,2], *B. Pukánszky*[1,2*]

[1]Laboratory of Plastics and Rubber Technology, Department of Physical Chemistry and Materials Science, Budapest University of Technology and Economics, H-1521 Budapest, P.O. Box 91, Hungary
[2]Institute of Materials and Environmental Chemistry, Chemical Research Center, Hungarian Academy of Sciences, H-1525 Budapest, P.O. Box 17, Hungary

Received 30 April 2009; accepted in revised form 19 August 2009

Abstract. Polypropylene (PP)/organophilized montmorillonite (OMMT) and polypropylene/organophilized montmorillonite/maleic anhydride grafted polypropylene (MAPP) composites were prepared in an internal mixer under a wide range of processing conditions to study the kinetics of structure formation. Structure and properties were characterized by a variety of techniques. The gallery structure of the organophilic silicate changed in spite of the fact that no compatibilizer was added to PP/OMMT composites. Silicate reflection shifted towards smaller 2θ angles, broadened and its intensity decreased indicating intercalation. Transmission electron microscopy (TEM) micrographs even showed individual platelets at long mixing times. However, the extent and direction of changes in the gallery structure of the silicate did not justify those observed in properties. The analysis of the results and additional experiments proved that the degradation of the polymer also takes place during processing leading to the formation of carbonyl and/or carboxyl groups, as well as to the decrease of molecular weight. The modification of the chain structure of the polymer influences interfacial interactions and the intercalation process. Some properties are directly determined by molecular weight (rheological properties, elongation). Both the clay and the MAPP seem to accelerate degradation. Thermooxidative degradation must have disadvantageous effect during the application of PP nanocomposites and needs further study.

Keywords: *nanocomposites, layered silicate, polypropylene, gallery structure, thermal degradation*

1. Introduction

The interest in polymer/layered silicate nanocomposites is still large and intensive research is going on in many research groups in this field in spite of the fact that a real breakthrough has not been achieved yet. The strong interest is justified mainly by the claimed advantages of such nanocomposites. The complete exfoliation of the nanometer thick silicate layers is expected to result in the formation of a large interface which should result in exceptional properties [1–4]. Reinforcement at small clay content [1–4], decreased flammability [1–3] and permeability [1–4], improved heat deflection temperature [2, 4] are among the most often cited advantages of these materials.

Although the principles for the preparation of layered silicate nanocomposites are clear, complete exfoliation and the expected improvement in properties are rarely achieved. Quite a few controversial results are reported about the structure and properties of these materials as well as about the effect of various factors on them. The extent of exfoliation in a polymer/layered silicate nanocomposite is determined by thermodynamic and kinetic factors as discussed among others by Vaia and Giannelis [5, 6]. Layered silicate nanocomposites are often

---

[*]Corresponding author, e-mail: bpukanszky@mail.bme.hu

complicated systems containing several components like the polymer, the silicate, the surfactant, and quite often also swelling and coupling agents or other additives to help exfoliation [7–14]. The competitive interactions acting among the various groups of the components are very difficult to estimate and control, which results in a wide range of structures often with inferior properties.

Similarly to the uncertainties related to the role and effect of interactions on the structure and properties of nanocomposites, the effect of kinetics, i.e. processing conditions, on structure development is also quite unclear. Some groups claim that processing conditions, or even preparation conditions do not influence the structure of the composites [15, 16], while others found a strong effect of processing [17, 18]. For example Yilmazer and Ozden [16] compared the effect of three preparation conditions, i.e. in situ polymerization, melt compounding and a masterbatch method, and did not find any significant difference in structure and properties of polystyrene (PS) nanocomposites. On the other hand, Paul and co-workers [19–21] carried out a detailed study on polyamide 6 (PA6) nanocomposites using a single and three twin-screw extruders for processing and found a profound effect of conditions on the structure of the composites. Twin-screw extruders, longer residence time and medium shear resulted in larger extent of exfoliation than other conditions including high shear. Lertvimolnun and Vergnes [22–24] came practically to the same conditions finding a strong effect of kinetics on the structure and properties of PP/layered silicate nanocomposites. These results clearly show that the combination of thermodynamics and kinetics must determine the extent of exfoliation, as well as the resulting properties.

In view of the controversies cited above, the goal of our work was to study the effect of various factors on structure development in PP/layered silicate composites. The study focused mainly on kinetic factors, but interactions were also modified by the addition of a compatibilizer. The experiments were carried out in two series. In the first series several polypropylene homopolymers with different melt flow indices were used as matrix to modify shear stresses, and both the time and the rate of mixing were also changed. In the second series the same polymer was used in all experiments, but maleated PP was also added to assist exfoliation. The rate and time of mixing were changed also in this series at several levels. The structure of the composites was characterized by various methods and several properties were measured in order to identify the processes taking place during mixing and the most important factors influencing them.

2. Experimental

Five PP homopolymers produced by TVK, Hungary were used in the first series of experiments, the Tipplen H377 (PP90), H483 (PP65), H543 (PP40), H605 (PP30) and the H890 (PP03) grades. All polymers, their abbreviation and melt flow index (MFI) value are compiled in Table 1 together with the composition of the nanocomposites studied. The abbreviation is based on the MFI of the polymers. All polymers contained a commercial additive package except the H605 grade. The Nanofil 848 (N 848) product of Süd Chemie was used as silicate. This clay is coated with stearyl amine, its density is 1.8 g/cm^3, moisture content 2 wt%, organic content 25 wt% and particle size 3 µm. Composition was the same in all experiments, 2 vol% clay was added to the polymer. The Tipplen H 649 (PP25) grade was used as matrix polymer in the second series, the Nanofil SE 3000 (NSE 3000) silicate as reinforcement. The silicate was organophilized with 55 wt% distearyldimethyl amine, its density was 1.8 g/cm^3 and the average

Table 1. Characteristics of the polymers and composition of the nanocomposites studied

Polymer			MAPP		Silicate	
Trade name	**Abbrev.**	**MFI[a] [g/10 min]**	**Type**	**vol%**	**Type**	**vol%**
Tipplen H 377	PP90	9.0	–	0	N 848	2
Tipplen H 483	PP65	6.5	–	0	N 848	2
Tipplen H 543	PP40	4.0	–	0	N 848	2
Tipplen H 605	PP30	3.0	–	0	N 848	2
Tipplen H 890	PP03	0.3	–	0	N 848	2
Tipplen H 649	PP25	2.5	AR 504	20	NSE 3000	1

[a]Determined at 230°C and 21.6 N

particle size was less than 10 µm. A small molar mass maleated PP, Licomont AR 504 (AR 504, Clariant AG) was used as coupling agent to promote exfoliation. Its maleic anhydride content was 3.5 wt% and it had very low viscosity (0.8 Pa·s at 170 °C). The composites contained 1 vol% clay and 20 vol% MAPP in this series.

Composites were prepared in a Brabender W 50 EH internal mixer attached to a Haake Rheocord EU 10 V driving unit at 190 °C. Charge volume was 42 cm^3 in both series. Samples were prepared at the combination of 2, 5, 8, 10, 12, 15 and 20 min mixing time and 50 rpm, as well as at 10, 30, 70 and 100 rpm and 8 min in the first series. Time changed in six (5, 10, 15, 30, 45 and 60 min), while the rate of mixing in four (20, 50, 80 and 120 rpm) steps and samples were prepared at all combinations of the parameters in the second series. The homogenized samples were compression molded into 1 mm thick plates using a Fontijne SRA 100 machine at 190 °C and 3 min preheating and 3 min compression time.

The gallery structure of the silicate was characterized by X-ray diffraction (XRD) using a Phillips PW 1830/PW 1050 equipment with CuK$_\alpha$ radiation at 40 kV and 35 mA. The morphology of the samples was examined by transmission electron microscopy. 50–100 nm thick slices were cut at –80 °C with a Leica Ultracut UCT microtome. TEM images were created with a Philips CM30 Twin STEM electron microscope fitted with Kevex Delta-Plus EDX and Gatan model 666 PEELS. Thin films of approximately 100 µm thickness were compression molded from the composites for Fourier transform infrared spectroscopy (FTIR). The spectra were recorded using a Mattson Galaxy 3020 spectrometer (Unicam) in the 4000–400 cm^{-1} wavelength range with 4 cm^{-1} resolution in 16 scans. The color of the samples was measured using a Hunterlab Colourquest 45/0 apparatus and it was characterized by the yellowness index according to the ASTM D 1925 standard. Rheological measurements were carried out using a Paar Physica UDS 200 apparatus at 200 °C in oscillatory mode in the frequency range of 0.1–600 1/sec on discs with 25 mm diameter and 0.5 mm thickness. The amplitude of the deformation was 5%, which was in the linear elastic region checked by an amplitude sweep. The tensile properties of the samples were measured using an Instron 5566 apparatus. Young's modulus was determined at 0.5 mm/min cross-head speed. 50 mm/min was used in the first and 5 mm/min in the second series for the determination of tensile strength and elongation-at-break. All characteristics were derived from three parallel measurements.

3. Results and discussion

The results are presented in three sections. The two series are discussed separately first, then they are compared in a subsequent section to draw general conclusions from the study. Mostly the time dependence of properties will be shown to simplify discussion, practically the same conclusions can be drawn from the effect of the rate of processing on structure and properties.

3.1. PP/OMMT composites

The torque developing in the mixer was recorded during the preparation of the samples. Torque is proportional to shear stress, and since average shear rate is constant, it is proportional also to the viscosity of the melt. The torque recorded at the end of the homogenization is plotted against mixing time in Figure 1 for two composites with different matrices. The viscosity of the remaining three polymers was very similar to that of PP65, which was quite surprising since their MFI changed between 3 and

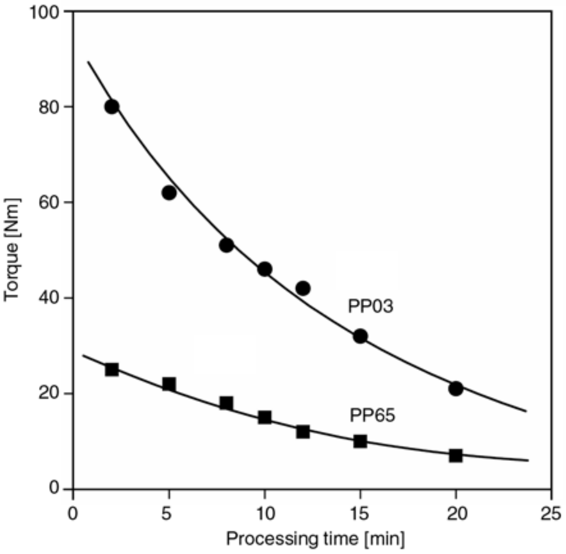

Figure 1. Effect of processing time and the molecular weight of the matrix polymer on the viscosity (torque) of layered silicate composite melts containing 2 vol% OMMT

6.5 g/10 min. This similarity was observed in most properties, therefore we usually present only two correlations for the sake of clarity. However, the similarity of the behavior of the four polymers needs further study and explanation.

Torque decreases with time in both cases indicating changes in the structure of the composites. A definite explanation obviously cannot be given based on these correlations; one can only speculate on the possible reasons. Torque usually decreases in the first stage of the mixing until the material reaches constant temperature. In our case the decrease is continuous, thus it must be related to structural changes. Both the dispersed structure of the composite and the molecular structure of PP may change during mixing. The relatively large micron sized particles are evenly distributed in the matrix, but possible intercalation and/or exfoliation may also lead to changes in viscosity. One would expect an increase in viscosity with exfoliation, since exfoliation creates new surfaces, and strong interaction should lead to the formation of an interphase with decreased mobility. On the other hand, we know that the surface free energy of organophilic MMT is small [25], thus weak interaction with the clay may result in the disruption of entanglements and weaker interaction among the chains, like in PVC nanocomposites [26]. Naturally this latter explanation is rather improbable considering the very small surface tension of PP and the resulting weak interactions in this polymer.

Both of the polymers contain a commercial additive package, i.e. they are sufficiently stabilized for normal processing and application purposes. However, we know that PP is rather sensitive to degradation which proceeds through β-scission in this polymer resulting in the decrease of molecular weight. If the organoclay catalyses the chemical reactions occurring during the processing of the polymer and promotes degradation, chains scission may occur and molecular weigh decreases as a result. Only the analysis of further results may answer these questions.

Although extensive exfoliation is not expected in the absence of a compatibilizer in these PP/OMMT composites, structural changes may occur, which can influence their properties, including viscosity. The WAXS patterns of the composites prepared from PP03 with 2 vol% OMMT are presented in Figure 2. Although not very dramatic, but a clear change can be observed in the traces. The characteristic peak of the silicate broadens and shifts towards smaller 2θ angles. This latter change is usually explained by the intercalation of the polymer into the galleries of the silicate, while the broadening indicates less regular stacking of the layers. Accordingly, the WAXS study indicates changes in the gallery structure of the polymer and/or limited exfoliation. In order to check the dispersed structure of the composites TEM micrographs were taken from selected samples. These also corroborate our conclusion that structure changes somewhat during the processing of the composites. A very large particle of at least 5 micron size is seen in the TEM micrograph taken from the PP65 composite after 5 min processing time (Figure 3a). The particle is very compact, intercalation or exfoliation cannot be observed at all. On the other hand, structure changes considerably after 20 min homogenization as Figure 3b shows. The size of this particle is much smaller, its structure is looser and individual platelets as well as smaller fragments are also visible in the micrograph (see arrows). Longer mixing obviously resulted in the transformation of structure.

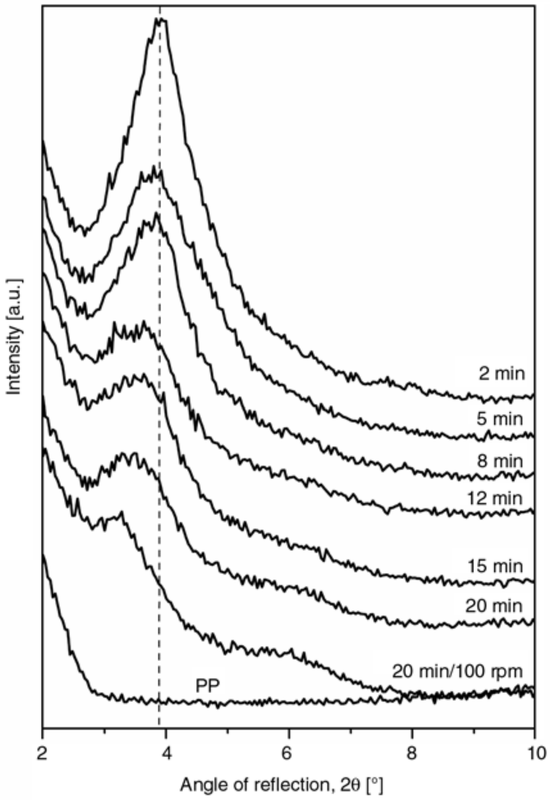

Figure 2. WAXS patterns of PP03/OMMT composites processed under various conditions. See shift and broadening of the silicate reflection.

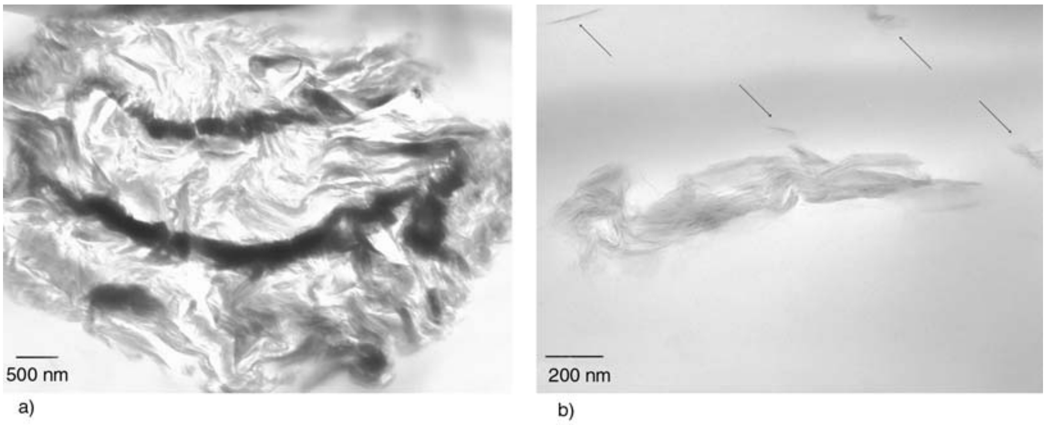

Figure 3. Changes in the gallery structure of the silicate with increasing processing time. PP65/2 vol% OMMT. a) 5 min, 50 rpm, b) 20 min, 50 rpm. Arrows indicate individual platelets or smaller particles.

However, these changes are not necessarily related to the decrease of viscosity during mixing. On the other hand, a very close correlation is obtained if we plot the intensity of the silicate reflection, characterized by the area under the peak, against the torque measured at the end of mixing (Figure 4). The tendency is clear in spite of the small differences observed among the polymers with smaller molecular weights. The arrow in the figure indicates increasing processing time. Accordingly, gallery distance increases (not shown) and the intensity of the reflection decreases with decreasing viscosity. Obviously the magnitude of shear forces does not play a determining role in these structural changes, since it decreases continuously with increasing processing time. Larger mobility of the smaller molecules may facilitate diffusion into the galleries, but the degradation of the polymer might modify interactions as well.

The changes in the structure of the composites resulted in the modification of properties as well. The Young's modulus of composites prepared with three matrices is plotted against mixing time in Figure 5. The broken line in the figure indicates the stiffness of a PP/$CaCO_3$ composite containing 5 vol% filler. $CaCO_3$ does not exfoliate thus it is used as reference for non-exfoliated PP/OMMT composites. Stiffness is determined by the crystalline structure of the polymer and by the extent of exfoliation. The correlations are very difficult to explain. Modulus increases with increasing MFI of the matrix, which would indicate the effect of chain mobility. However, the decrease of stiffness cannot be explained at all, it must be related to changing crystalline structure or increased interaction hinder-

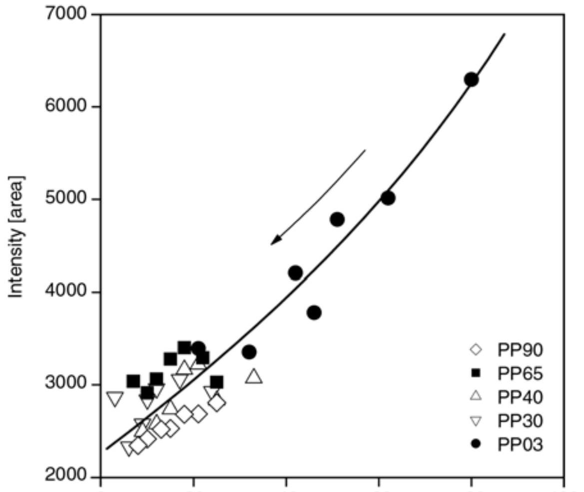

Figure 4. Correlation between the intensity of the silicate reflection and the torque (viscosity) measured at the end of the mixing

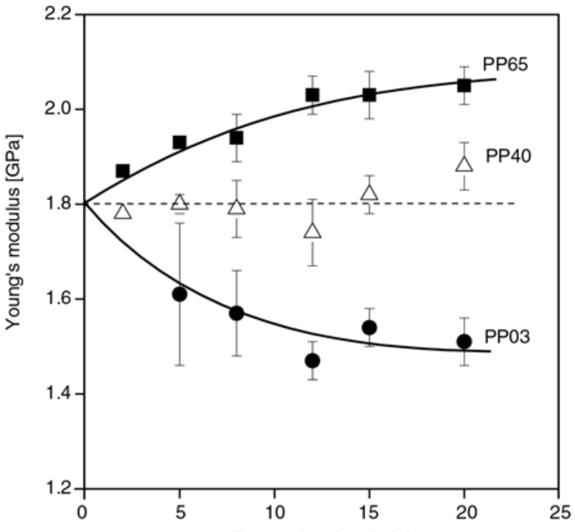

Figure 5. Effect of matrix properties and processing time on the stiffness of PP/OMMT composites

ing the crystallization of the polymer (see PP03). Both the position of the silicate reflection and its intensity decreased indicating increased intercalation and/or some exfoliation, confirmed also by the TEM study. These changes should have resulted in an increase and not a decrease in stiffness.

Figure 6 presents changes in the relative deformability of the samples with increasing processing time for composites prepared with three matrices. The elongation-at-break values of the neat polymers differ considerably due to their dissimilar molecular weight, thus relative values must be used for comparison. The results further complicate the situation and finding a plausible explanation for the changes. One would expect some correlation between molecular weight and changes in deformability here too, but the PP30 matrix maintains the largest deformability, while the PP03 polymer with the largest initial elongation-at-break has an intermediate value. At longer processing times the deformability of the PP65 polymer is close to zero. The relative order of the polymers is very difficult to understand, since the PP65 and PP03 polymers contained commercial stabilizer packages, while the PP30 polymer was not stabilized. Nevertheless, after considering all the results presented above, and those not shown, we may conclude that the degradation of the polymers and the resulting changes in their molecular structure may play a role in the determination of structure and properties.

In order to check this hypothesis, FTIR spectra were recorded on the neat polymers and on the composites. Evaluation was rather difficult in the latter case because of the intensive absorbance of the silicate. Nevertheless a peak was detected in the spectra at 1714 cm^{-1} in the range where usually carbonyl and carboxyl groups absorb. The intensity of this vibration is plotted against processing time in Figure 7. The number of carbonyl groups seems to increase considerably during processing which supports our hypothesis about the degradation of the polymer. In a further attempt to prove the role of degradation, we introduced additional amounts of stabilizer into the composite (0.1 wt% Irganox 1010). The change of torque with time is presented in Figure 8 for composites prepared with the PP03 polymer with and without additional stabilization. The difference is clear, viscosity decreases somewhat at the shorter processing times, most probably because of increasing temperature, and remains more or less constant afterwards for the stabilized sample. We must mention here that the elongation-at-break values change similarly with stabilization indicating the clear effect of molecular weight and degradation in the determination of this property. We can conclude that PP degrades in smaller or larger extent during the production of these layered silicate composites. The extent of degradation must depend on the efficiency of stabilization. The clay seems to accelerate degradation. Changing molecular structure modifies chain structure, which influ-

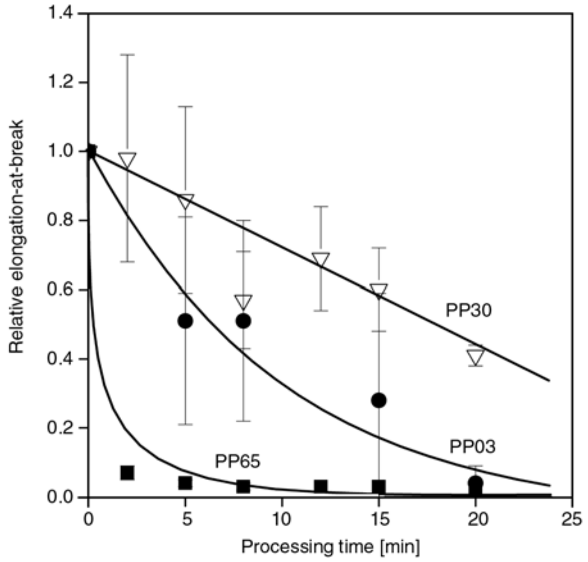

Figure 6. Changes in the relative elongation-at-break values of PP/OMMT composites with the MFI of the matrix and with increasing processing time

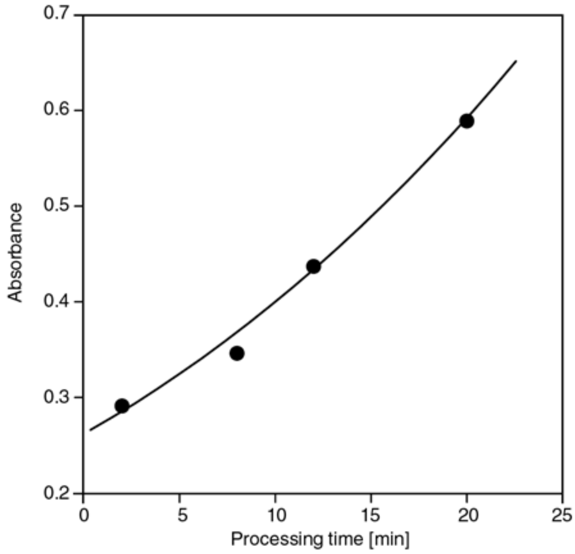

Figure 7. Increasing carbonyl content of PP03/OMMT composites with increasing time of homogenization

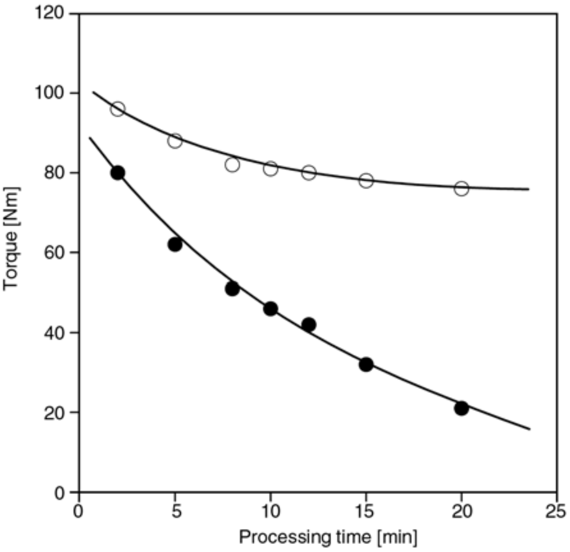

Figure 8. Effect of additional stabilization on the viscosity (torque) of PP03/PP composites. (•) without additional stabilization, (o) with 0.1 wt% Irganox 1010 stabilizer.

ences interactions and mobility, but also the structure of the composites. The degree of exfoliation is very limited but some intercalation definitely occurs in the studied PP/OMMT composites. The role of the clay in degradation processes needs further investigation.

3.2. PP/OMMT/MAPP composites

PP nanocomposites are practically always prepared with a compatibilizer in order to facilitate exfoliation. Exfoliation was very limited in the absence of MAPP indeed, as shown in the previous section. In the next series of experiments we added a small molecular weight MAPP compatibilizer with large functionality [27, 28] to the composites. The effect of the compatibilizer on the gallery structure of the composites is shown in Figure 9. The silicate peak completely disappears already after 5 min mixing time even under very moderate shear conditions (20 rpm). Further changes cannot be observed in the pattern with increasing processing load (60 min, 120 rpm). Some authors claim complete exfoliation based on the disappearance of the silicate reflection [29, 30], but several studies proved that this is not true [31, 32]. Nevertheless, the gallery structure of the composite changed considerably in the presence of the compatibilizer. This change is confirmed by the TEM micrograph taken from the sample processed at 50 rpm for 10 min (Figure 10).

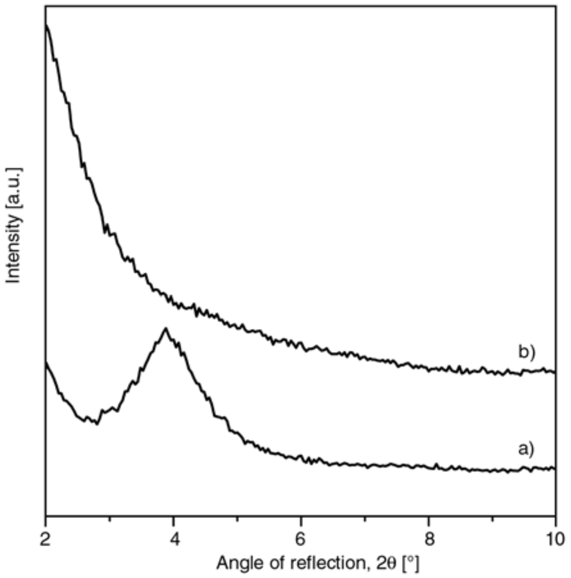

Figure 9. Influence of maleated PP compatibilizer on the gallery structure of the silicate in PP/OMMT nanocomposites. See the disappearance of the silicate reflection. a) PP/OMMT, 10 min, 50 rpm, b) PP/OMMT/MAPP, 10 min, 50 rpm.

Figure 10. TEM micrograph taken from a silicate particle in a PP/OMMT/MAPP nanocomposite. See the loose structure, changing platelet density and individual platelets

A relatively large particle, but with a very loose structure can be observed in the figure. The density of platelets increases towards the center, gallery distance is larger at the edges and at the lower end of the particle. A few individual layers can also bee seen in the upper left corner. The micrograph proves that the disappearance of the silicate does not indicate complete exfoliation, but the compatibilizer loosens up the structure and helps intercalation as well as exfoliation.

Unfortunately, the proper evaluation of properties is very difficult when this small molecular weigh compound is used as compatibilizer. Especially the rheological properties change drastically in its presence. However, the time dependence of viscosity as well as the comparison of the viscosity of PP/MAPP blends to that of PP/OMMT/MAPP composites indicates that molecular weight decreases with increasing processing time (Figure 11), but also with increasing shear rate (not shown). This result confirms and strongly supports our previous observation about the possible degradation of the polymer during the processing of these layered silicate composites. A further proof for degradation is supplied by the changes in the color of the composites with processing conditions. The yellowness index of the composite processed at 50 rpm is plotted as a function of mixing time in Figure 12. The drastic increase in color is a clear proof of chemical reactions occurring in the composite during processing. The results of two independent series of measurements unambiguously prove that degradation of the polymer occurs and influences properties.

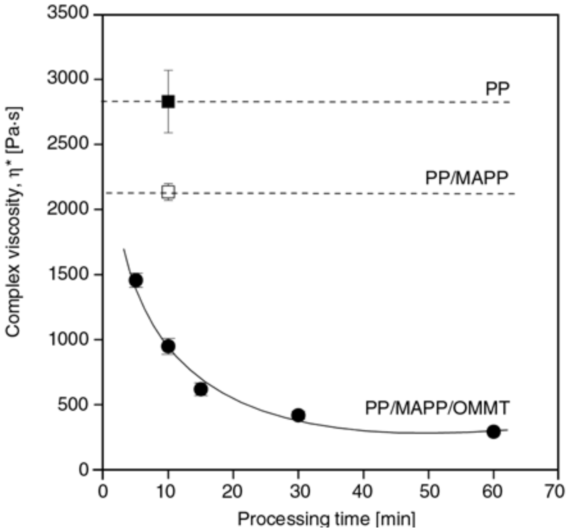

Figure 11. Effect of the compatibilizer, the clay and processing time on the complex viscosity of PP/OMMT/MAPP nanocomposites determined at 1 s^{-1} frequency. See the detrimental effect of the components.

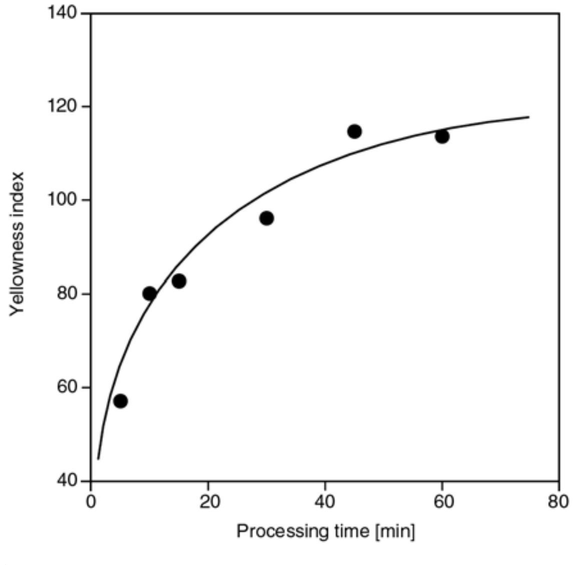

Figure 12. Increasing color of PP/OMMT/MAPP nanocomposites with increasing processing time at 50 rpm proving chemical reactions and degradation

3.3. Comparison, discussion

The stability of polymer/layered silicate nanocomposites is an often discussed topic in the literature, but not in the context encountered here. Layered silicates are claimed to improve thermal stability and the claim is usually supported by thermal gravimetric (TGA) measurements [33, 34]. Degradation temperature is supposed to increase due to the formation of a silicate layer, which hinders the diffusion of flammable gases out of and that of the oxygen into the composite. This phenomenon might be important in the burning of plastic products and flame retardancy, but not during the processing and use of such composites. Although the deteriorating effect of the components (OMMT, MAPP) was shown on the light stability of PP/layered silicate composites [35, 36], very few papers were published on thermooxidative stability. However, degradation is obviously accelerated by the organoclay and probably also by the functionalized polymer shown by both series of measurements of this study. Changing molecular structure of PP influences properties and complicates the evaluation of structure-property correlations.

The apparently contradictory results reported in the previous two sections are the results of complex processes including degradation, which modifies interactions and the kinetics of intercalation. The degradation of the polymer leads to the formation carbonyl and carboxyl groups even in the presence of stabilizers. Only a few carboxyl groups were shown to change interactions drastically in PP/$CaCO_3$ composites [37–39]. The increasing number of carbonyl groups changes the interaction of the polymer with the organophilic silicate and decreasing chain length leads to increased mobility and faster diffusion. These result in increased intercalation in PP/OMMT composites (Figures 2 and 3). However, stronger interaction modifies also crystallization and crystalline structure leading to a diverse response of modulus to changing processing conditions (Figure 5). Deformability is determined mainly by molecular weight (Figure 6).

In spite of the increasing number of carbonyl groups, intercalation and exfoliation is limited in PP/OMMT composites. The inclusion of MAPP assists intercalation, but complete exfoliation is not achieved even in this case. Degradation processes seem to be significant also in the presence of the functionalized polymer. The small molecular weight of MAPP and degradation further complicates the identification of the main factors determining structure and properties in these PP/OMMT/MAPP nanocomposites. Targeted experiments with proper experimental design are needed to separate the effects discussed here and resolve the complexity of the processes and factors playing a role in the preparation of PP nanocomposites.

4. Conclusions

The gallery structure of the organophilic silicate changed in spite of the fact that no compatibilizer was added to PP/OMMT nanocomposites. Silicate reflection shifted towards smaller 2θ angles, broadened and its intensity decreased indicating intercalation. TEM micrographs even showed individual platelets at long mixing times. However, the extent and direction of changes in the gallery structure of the silicate did not justify those observed in properties. The analysis of the results and additional experiments proved that the degradation of the polymer also takes place during processing leading to the formation of carbonyl and/or carboxyl groups, as well as to the decrease of molecular weight. The modification of chain structure influences interfacial interactions and the intercalation process. Some properties are directly determined by molecular weight (rheological properties, elongation). Both the clay and the functionalized polymer seem to accelerate degradation. Thermooxidative degradation must have disadvantageous effect during the application of PP nanocomposites and needs further study.

Acknowledgements

TVK, Süd Chemie and Clariant are acknowledged for the donation of the raw materials. We would like to express our sincere gratitude to Ágnes Ábrányi, László Százdi and Balázs Imre for their help in sample preparation and measurement. The authors are indebted to Gyeong-Man Kim for the preparation of some of the TEM micrographs. The project was partially financed by the National Scientific Research Fund of Hungary (OTKA K68748 and K67936), the support is highly appreciated.

References

[1] Alexandre M., Dubois P.: Polymer-layered silicate nanocomposites: Preparation, properties and uses of a new class of materials. Materials Science and Engineering R: Reports, **28**, 1–63 (2000).
DOI: 10.1016/S0927-796X(00)00012-7

[2] Ray S. S., Okamoto M.: Polymer /layered silicate nanocomposites: A review from preparation to processing. Progress in Polymer Science, **28**, 1539–1641 (2003).
DOI: 10.1016/j.progpolymsci.2003.08.002

[3] LeBaron P. C., Wang Z., Pinnavaia T. J.: Polymer-layered silicate nanocomposites: An overview. Applied Clay Science, **15**, 11–29 (1999).
DOI: 10.1016/S0169-1317(99)00017-4

[4] Pinnavaia T. J., Beall G. W.: Polymer-clay nanocomposites. Wiley, New York (2001).

[5] Vaia R. A., Giannelis E. P.: Lattice model of polymer melt intercalation in organically-modified layered silicates. Macromolecules, **30**, 7990–7999 (1997).
DOI: 10.1021/ma9514333

[6] Vaia R. A., Giannelis E. P.: Polymer melt intercalation in organically-modified layered silicates: Model predictions and experiment. Macromolecules, **30**, 8000–8009 (1997).
DOI: 10.1021/ma9603488

[7] Reichert P., Hoffmann B., Bock T., Thomann R., Mülhaupt R., Friedrich C.: Morphological stability of poly(propylene) nanocomposites. Macromolecular Rapid Communications, **22**, 519–523 (2001).
DOI: 10.1002/1521-3927(20010401)22:7<519::AID-MARC519>3.0.CO;2-W

[8] Kawasumi M., Hasegawa N., Kato M., Usuki A., Okada A.: Preparation and mechanical properties of polypropylene-clay hybrids. Macromolecules, **30**, 6333–6338 (1997).
DOI: 10.1021/ma961786h

[9] Kim K. N., Kim H., Lee J. W.: Effect of interlayer structure, matrix viscosity and composition of a functionalized polymer on the phase structure of polypropylene-montmorillonite nanocomposites. Polymer Engineering and Science, **41**, 1963–1969 (2001). DOI: 10.1002/pen.10892

[10] Usuki A., Kato M., Okada A., Kurauchi T.: Synthesis of polypropylene-clay hybrid. Journal of Applied Polymer Science, **63**, 137–139 (1997). DOI: 10.1002/(SICI)1097-4628(19970103)63:1<137::AID-APP15>3.0.CO;2-2

[11] Hasegawa N., Kawasumi M., Kato M., Usuki A., Okada A.: Preparation and mechanical properties of polypropylene-clay hybrids using maleic anhydride intercalation-modified polypropylene oligomer. Journal of Applied Polymer Science, **67**, 87–90 (1998). DOI: 10.1002/(SICI)1097-4628(19980103)67:1<87::AID-APP10>3.0.CO;2-2

[12] Zhang Y-Q., Lee J. H., Jang H-J., Nah C-W.: Preparing PP/clay nanocomposites using a swelling agent. Composites Part B: Engineering, **35**, 133–138 (2004). DOI: 10.1016/S1359-8368(03)00068-4

[13] Liu X. H., Wu Q. J.: PP/claynanocomposites prepared by grafting-melt intercalation. Polymer, **42**, 10013–10019 (2001). DOI: 10.1016/S0032-3861(01)00561-4

[14] Ishida H., Campbell S., Blackwell J.: General approach to nanocomposite preparation. Chemistry of Materials, **12**, 1260–1267 (2000). DOI: 10.1021/cm990479y

[15] Poisson C., Guerengomba J., Lacrampe M. F., Krawczak P., Gupta B., Miri V., Lefebvre J. M.: Mechanical, optical and barrier properties of PA6/nanoclay-based single- and multilayer blown films. Polymers and Polymer Composites, **16**, 349–358 (2008).

[16] Yilmazer U., Ozden Y.: Polystyrene-organoclay nanocomposites prepared by melt intercalation, in situ, and masterbatch methods. Polymer Composites, **27**, 249–255 (2006). DOI: 10.1002/pc.20191

[17] Hasegawa N., Usuki A.: Silicate layer exfoliation in polyolefin/clay nanocomposites based on maleic anhydride modified polyolefins and organophilic clay. Journal of Applied Polymer Science, **93**, 464–470 (2004). DOI: 10.1002/app.20459

[18] Modesti M., Lorenzetti A., Bon D., Besco S.: Effect of processing conditions on morphology and mechanical properties of compatibilized polypropylene nanocomposites. Polymer, **46**, 10237–10245 (2005). DOI: 10.1016/j.polymer.2005.08.035

[19] Dennis H. R., Hunter D. L., Chang D. H., Kim S. Y., White J. L., Cho J. W., Paul D. R.: Nanocomposites: The importance of processing. Plastics Engineering. **57**, 56–60 (2001).

[20] Dennis H. R., Hunter D. L., Chang D. H., Kim S. Y., White J. L., Cho J. W., Paul D. R.: Effect of melt processing conditions on the extent of exfoliation in organoclay-based nanocomposites. Polymer, **42**, 9513–9522 (2001). DOI: 10.1016/S0032-3861(01)00473-6

[21] Chavarria F., Shah R. K., Hunter D. L., Paul D. R.: Effect of melt processing conditions on the morphology and properties of nylon 6 nanocomposites. Polymer Engineering and Science, **47**, 1847–1864 (2007). DOI: 10.1002/pen.20894

[22] Lertwimolnun W., Vergnes B.: Influence of compatibilizer and processing conditions on the dispersion of nanoclay in a polypropylene matrix. Polymer, **46**, 3462–3471 (2005). DOI: 10.1016/j.polymer.2005.02.018

[23] Lertwimolnun W., Vergnes B.: Effect of processing conditions on the formation of polypropylene/organoclay nanocomposites in a twin screw extruder. Polymer Engineering and Science, **46**, 314–323 (2006). DOI: 10.1002/pen.20458

[24] Lertwimolnun W., Vergnes B.: Influence of screw profile and extrusion conditions on the microstructure of polypropylene/organoclay nanocomposites. Polymer Engineering and Science, **47**, 2100–2109 (2007). DOI: 10.1002/pen.20934

[25] Kádár F., Százdi L., Fekete E., Pukánszky B.: Surface characteristics of layered silicates: Influence on the properties of clay/polymer nanocomposites. Langmuir, **22**, 7848–7854 (2006). DOI: 10.1021/la060144c

[26] Pozsgay A., Csapó I., Százdi L., Pukánszky B.: Preparation, structure, and properties of PVC/montmorillonite nanocomposites. Materials Research Innovations, **8**, 138–139 (2004).

[27] Kaempfer D., Thomann R., Mülhaupt R.: Melt compounding of syndiotactic polypropylene nanocomposites containing organophilic layered silicates and in situ formed core/shell nanoparticles. Polymer, **43**, 2909–2916 (2002). DOI: 10.1016/S0032-3861(02)00113-1

[28] Misheva M., Djourelov N., Zamfirova G., Gaydarov V., Cerrada M. L., Rodríguez-Amor V., Pérez E.: Effect of compatibilizer and electron irradiation on free-volume and microhardness of syndiotactic polypropylene/clay nanocomposites. Radiation Physics and Chemistry, **77**, 138–145 (2008). DOI: 10.1016/j.radphyschem.2007.04.007

[29] Hasegawa N., Okamoto H., Kawasumi M., Kato M., Tsukigase A., Usuki A.: Polyolefin-clay hybrids based on polyolefins and organophilic clay. Macromolecular Materials and Engineering, **280**, 76–79 (2000). DOI: 10.1002/1439-2054(20000801)280:1<76::AID-MAME76>3.0.CO;2-#

[30] Tang Y., Hu Y., Wang S. F., Gui Z., Chen Z. Y.: Preparation of poly(propylene)/clay layered nanocomposites by melt intercalation from pristine montmorillonite (MMT). Polymers for Advanced Technologies, **14**, 733–737 (2003).
DOI: 10.1002/pat.420

[31] Wagener R., Reisinger T. J. G.: A rheological method to compare the degree of exfoliation of nanocomposites. Polymer, **44**, 7513–7518 (2003).
DOI: 10.1016/j.polymer.2003.01.001

[32] Morgan A. B., Gilman J. W.: Characterization of polymer-layered silicate (clay) nanocomposites by transmission electron microscopy and X-ray diffraction: A comparative study. Journal of Applied Polymer Science, **87**, 1329–1338 (2003).
DOI: 10.1002/app.11884

[33] Zhang J., Jiang D. D., Wilkie C. A.: Thermal and flame properties of polyethylene and polypropylene nanocomposites based on an oligomerically-modified clay. Polymer Degradation and Stability, **91**, 298–304 (2006).
DOI: 10.1016/j.polymdegradstab.2005.05.006

[34] Zhang Y-Q., Lee J-H., Rhee J. M., Rhee K. Y.: Polypropylene-clay nanocomposites prepared by in situ grafting-intercalating in melt. Composites Science and Technology, **64**, 1383–1389 (2004).
DOI: 10.1016/j.compscitech.2003.10.014

[35] Mailhot B., Morlat S., Gardette J-L., Boucard S., Duchet J., Gérard J-F.: Photodegradation of polypropylene nanocomposites. Polymer Degradation and Stability, **82**, 163–167 (2003).
DOI: 10.1016/S0141-3910(03)00179-4

[36] Morlat-Therias S., Mailhot B., Gonzalez D., Gardette J-L.: Photooxidation of polypropylene/montmorillonite nanocomposites. 2. Interactions with antioxidants. Chemistry of Materials, **17**, 1072–1078 (2005).
DOI: 10.1021/cm040172l

[37] Demjén Z., Pukánszky B., Nagy J. Jr.: Possible coupling reactions of functional silanes and polypropyelene. Polymer, **40**, 1763–1773 (1998).
DOI: 10.1016/S0032-3861(98)00396-6

[38] Demjén Z., Pukánszky B., Nagy J. Jr.: Evaluation of interfacial interaction in polypropylene/surface treated $CaCO_3$ composites. Composites Part A: Applied Science and Manufacturing, **29**, 323–329 (1998).
DOI: 10.1016/S1359-835X(97)00032-8

[39] Demjén Z., Pukánszky B.: Effect of surface coverage of silane treated $CaCO_3$ on the tensile properties of polypropylene composites. Polymer Composites, **18**, 741–747 (1997).
DOI: 10.1002/pc.10326

eXPRESS Polymer Letters Vol.3, No.11 (2009) 703–712
Available online at www.expresspolymlett.com
DOI: 10.3144/expresspolymlett.2009.88

Highly organosoluble and transparent polyamides containing cyclohexane and trifluoromethyl moieties: Synthesis and characterization

P. H. Li, C. Y. Wang, G. Li[*], *J. M. Jiang*

State Key Laboratory for Modification of Chemical Fibers and Polymer Materials College of Material Science and Engineering, Donghua University, Shanghai 201620, China

Received 6 July 2009; accepted in revised form 19 August 2009

Abstract. New aromatic diamine with cyclohexane moiety substituted with trifluoromethyl group in the side chain, 4,4'-(cyclohexane-1,4-diylbis(oxy))bis(3-(trifluoromethyl)aniline) (**2**), was successfully synthesized through the Williamson reaction of 1,4-cyclohexanediol and 2-chloro-5-nitrobenzotrifluoride, to yield the intermediate dinitro compound **1**, followed by catalytic reduction with hydrazine and Pd/C to afford the diamine **2**. This diamine monomer leads to a series of organic-soluble polyamides (**4a–d**) when reacted with different commercially available aromatic diacids (**a–d**) via a direct polycondensation with triphenyl phosphite and pyridine. The resulting polymers had inherent viscosities ranging from 0.89 to 1.29 dl/g. All the polymers showed outstanding solubility and could be easily dissolved in amide-type polar aprotic solvents and even dissolved in less polar solvents. All the polymers formed transparent, strong, and flexible films with tensile strengths of 54–68 MPa, Young's moduli of 1.6–1.9 GPa, and elongations at break of 13.3–15.5%. These polyamide films have low dielectric constants of 2.15–2.88 at 1 MHz and low water absorptions of 1.96–2.84%. Wide-angle X-ray diffraction measurements revealed that these polyamides were amorphous in nature.

Keywords: *polymer synthesis, molecular engineering, solubility, optical transparency, dielectric constant*

---

1. Introduction

Commercial wholly aromatic polyamides have been well known for their high temperature stability, excellent mechanical strength and good chemical resistance, which qualify them as high-performance polymeric materials [1–8]. However, these wholly aromatic polyamides usually shows poor solubility in common organic solvents and their extremely high melting temperatures, which lie above their decomposition temperatures, give rise to processing difficulties and so limit their applications. In order to overcome these drawbacks, considerable efforts have been made to modify their chemical structure to improve processability and solubility, so that to facility their use in a specific field. There are various approaches for improvement of the solubility and processability of polyamides without sacrificing their high thermal stability and mechanical properties, such as, the incorporation of the flexible linkages (e.g. –O–, –SO_2–, etc.) [9, 10], cardo groups (such as cyclododecylidene, pyrene, and naphthalene, etc.) [11–13], or molecular asymmetry (*ortho*, *meta* versus linkages) [14–16] into the backbone or addition of bulky side group (such as *tert*-butyl, norbornane units) [17–21]. For example, the bis(ether amine)s and its aromatic polymer with cyclohexane group was synthesized and showed solubility in organic and polar solvents [22, 23]. Moreover, it was also proved that polyamides with trifluoromethyl-sub-

---

[*] Corresponding author, e-mail: lig@dhu.edu.cn

stituted benzene in the side chain could enhance the solubility, reduce dielectric constant and moisture absorption, and raise the optical transparency [24–30]. Therefore, this work is focused on the synthesis of a new CF_3-containing aromatic diamine **2** with cyclohexane moiety, and the preparation of fluorinated polyamides polycondensed with various diacids (**a–d**). The basic properties of the fluorinated polyamides were investigated.

2. Experimental section

2.1. Materials

1,4-cyclohexanediol (cis+trans, 98+%, from Alfa Aesar), 2-chloro-5-nitrobenzotrifluoride (98%, from ACROS), sodium hydride (60%, from Alfa Aesar) as well as 10% Pd/C (from MERCK) were used as received. Commercially obtained anhydrous calcium chloride ($CaCl_2$) was dried under vacuum at 180°C for 8 h. Reagent-grade aromatic dicarboxylic acids such as terephthalic acid (TPA), isophthalic acid (IPA), 4,4'-oxydibenzoic acid (OBA) and, 2,2-bis(4-carboxy-phenyl)hexafluoropropane (6FA) were purified by recrystallization. *N*-Methy-2-pyrrolidone (NMP), Pyridine (Py), *N*,*N*-dimethylacetamide (DMAc), *N*,*N*-dimethylformamide (DMF) and triphenyl phosphite (TPP) all from Alfa were purified by distillation under reduced pressure over calcium hydride. All other chemicals and solvents were reagent-grade and used without further purification unless otherwise noted.

2.2. Monomer synthesis

2.2.1. Synthesis of 1,4-bis(4-nitro-2-(trifluoromethyl)phenoxy)cyclohexane (1)

NaH (6.4 g, 0.16 mol) was firstly placed into a 250 ml, three-necked round-bottom flask equipped with a mechanical stirrer, N_2 inlet, and dropping funnel. A mixture of 1,4-cyclohexanediol (6.5 g, 0.056 mol) and *N*,*N*-dimethylformamide (50 ml) was added dropwise through the dropping funnel at 0°C. After stirring at 0°C for 2 hours, the mixture of 2-chloro-5-nitrobenzotrifluoride (25.9 g, 0.115 mol) and *N*,*N*-dimethylformamide (50 ml) was then added dropwise, and the reaction mixture was stirred at 5°C for 20 hours. Then the mixture was poured into 300 ml distilled water. Some yellow solids precipitated out which were filtered and washed with ethanol for several times. The crude product obtained was recrystallized from DMF/ethanol to give fine, light yellow crystals (20.07 g, 72.5%). The properties of the product were found to be as follow. Melting point: 247–248°C [differential scanning calorimetry (DSC) at a scanning rate of 10°C/min]. FT-IR (KBr): 1518, 1333 ($C–NO_2$ stretching); 1286, 1211, 1140, 1117 cm^{-1} (C–O and C–F stretching). ^1HNMR ($CDCl_3$, δ): 8.56 (d, $J = 2.57$ Hz, 2H, H_1), 8.45 (dd, $J_1 =$ 9.18 Hz, $J_2 = 2.65$ Hz, 2H, H_2), 7.14 (d, $J =$ 9.24 Hz, 2H, H_3), 4.96 (s, 2H, H_4), 2.15 (m, 2H, H_5), 2.03 (m, 4H, H_6). Elemental analysis ($C_{20}H_{16}F_6N_2O_6$): Calcd. C, 48.59%; H, 3.26%; N, 5.67%. Found C, 49.01%; H, 3.45%; N, 5.94%.

2.2.2. Synthesis of 4,4'-(cyclohexane-1,4-diylbis(oxy))bis(3-(trifluoromethyl)aniline) (2)

The purified dinitro compound **1** (14.8 g, 0.03 mol), 0.3 g of 10% Pd/C and 100 ml ethanol were taken into a three-necked flask and hydrazine monohydrate (15 ml) was added dropwise over a period of 30 min at 80°C. Upon completing addition, the mixture was heated at the reflux temperature for another 3 h. The reaction solution was filtered hot to remove Pd/C and the obtained solution was concentrated. Then the precipitated white solid was filtered and washed with ethanol to yield white crystals (11.1 g, 85.1%).

The properties of the crystals were found to be as follows. Melting point: 156–157°C (differential scanning calorimetry (DSC) at a scan rate of 10°C/min). FT-IR (KBr): 3460, 3436, 3357, (N–H stretching); 1259, 1236, 1217, 1146 cm–1 (C–O and C–F stretching). ^1HNMR (DMSO-d_6, δ): 7.02 (d, $J = 8.83$ Hz, 2H, H_1), 6.83 (d, $J = 2.70$ Hz, 2H, H_2), 6.78 (dd, $J_1 = 8.74$ Hz, $J_2 = 2.59$ Hz, 2H, H_3), 5.15 (brs, 4H, $–NH_2$), 4.45 (s, 2H, H_4) 1.93 (d, $J = 8.29$ Hz, 4H, H_5), 1.58 (m, 4H, H_6). Elemental analysis ($C_{20}H_{20}F_6N_2O_2$): Calcd. C, 55.30%; H, 4.64%; N, 6.45%; Found C, 55.92%; H, 4.98%; N, 6.74%.

2.3. Polymer synthesis

A generally synthetic procedure for the polyamides was described as follows: A mixture of (0.6516 g, 1.5 mmol) of diamine **2**, 4,4'-oxydibenzoic acid ©

(0.3875 g, 1.5 mmol), 0.45 g of calcium chloride, 1.8 ml of TPP, 1.0 ml of pyridine, and 6 ml of NMP was heated in nitrogen with stirring at 120°C for 3 h. As the polycondensation proceeded, the reaction mixture became viscous gradually. The resultant solution of the polymer was poured slowly into 400 ml of stirred methanol giving rise to a tough, fiber-like polymer precipitate. The precipitate was collected, washed with hot ethanol for three times and dried at 160°C under vacuum for 6 h to give **4c** (1.03 g, 95%). FT-IR (film): 3305 cm^{-1} (N–H stretching), 1653 cm^{-1} (C=O stretching), 1246 cm^{-1} (C–O stretching), 1137, 1171 cm^{-1} (C–F stretching). ^{1}HNMR (DMSO-d_6, δ): 10.34 (s, 2H, H_7), 8.12 (s, 2H, H_1), 8.06 (d, J = 8.44, 4H, H_9), 7.97 (d, J = 7.24, 2H, H_2), 7.37 (d, J = 9.24, 2H, H_3), 7.23 (d, J = 8.00, 4H, H_8), 4.79 (s, 2H, H_4), 1.99 (m, 4H, H_5), 1.74 (d, 4H, J = 3.20, H_6).

2.4. Measurements

^{1}HNMR spectra were performed on a Bruker AV400 instrument with dimethyl sulfoxide (DMSO-d_6) or $CDCl_3$ as the solvent and tetramethylsilane (TMS) as an internal standard. FT-IR spectra were recorded on a Nicolet Magna 470 spectrometer. Ultraviolet-visible (UV-vis) spectra of the polymer films (~10 µm thickness) were recorded on a Lambda 35 (Perkin Elmer) spectrophotometer at room temperature. Elemental analysis was carried out on a Carlo Erba1106 system. Differential scanning calorimetry (DSC) analysis was performed on a PE Diamond DSC instrument at a heating rate of 10°C/min in nitrogen atmosphere. Glass transition temperatures (T_g) were read at the middle of the transition in the heat capacity from the second heating scan. Thermogravimetric analysis (TGA) of the polymer samples was measured on a Netzsch TG 209F1 instrument at a heating rate of 20°C/min in nitrogen atmosphere, and T_{10} is reported as the temperatures where 10% weight losses was observed. Inherent viscosities ($\eta_{inh} = \ln\eta_r/c$) were measured at a concentration of 0.5 g/dl in DMAc at 30°C with an Ubbelohde viscometer. Mechanical properties of the films were investigated with an AGS-500ND tensile tester at a crosshead speed of 5 mm/min. An average of at least five individual specimens was used. Wide-angle X-ray diffraction (WAXD) was conducted on a Rigaku D/Max-2550PC X-ray diffraction with Cu/$K_{\alpha1}$ radiation, operated at 40 kV and 300 mA. The dielectric constants (round shape samples, D = 15 mm) were measured on a HP4291B at a frequency region of 1 MHz–1.1 GHz and 25°C. The equilibrium water uptake was determined by the weighing of the changes in vacuum-dried film specimens before and after immersion in deionized water at 25°C for three days.

3. Results and discussion

3.1. Monomers synthesis and characterization

The new CF_3-subsititued bis (ether amine) **2** was prepared in a two-step reaction process as shown in Figure 1. The first step is the Williamson reaction of 2-chloro-5-nitrobenzotrifluoride with 1,4-cyclohexanediol in anhydrous DMF in the presence of sodium hydride. The target diamine **2** was obtained by the catalytic reduction of **1** with hydrazine hydrate and Pd/C catalyst in refluxing ethanol. The structure of the dinitro compound **1** and the diamine monomer **2** were investigated by elemental analysis as well as FT-IR and ^{1}HNMR spectroscopy. The FT-IR spectra of dinitro compound **1** and diamine **2** are showed in Figure 2. The nitro groups in compound **1** gave two characteristic bands at 1518 and 1333 cm^{-1} (–NO_2 asymmetric and symmetric stretching). After reduction, the characteristic absorptions of the nitro group disappeared, and the amino group occurred at bands in 3300–3500 cm^{-1} showing typical of N–H stretching. Figure 3 illustrates the ^{1}HNMR spectra of dinitro compound **1** and diamine **2** respectively. From the ^{1}HNMR spectra **1** and **2**, the absorption signals

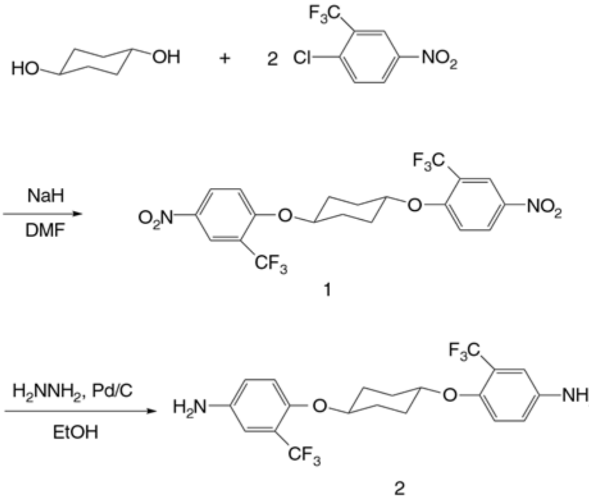

Figure 1. Synthetic route to the diamine monomer **2**

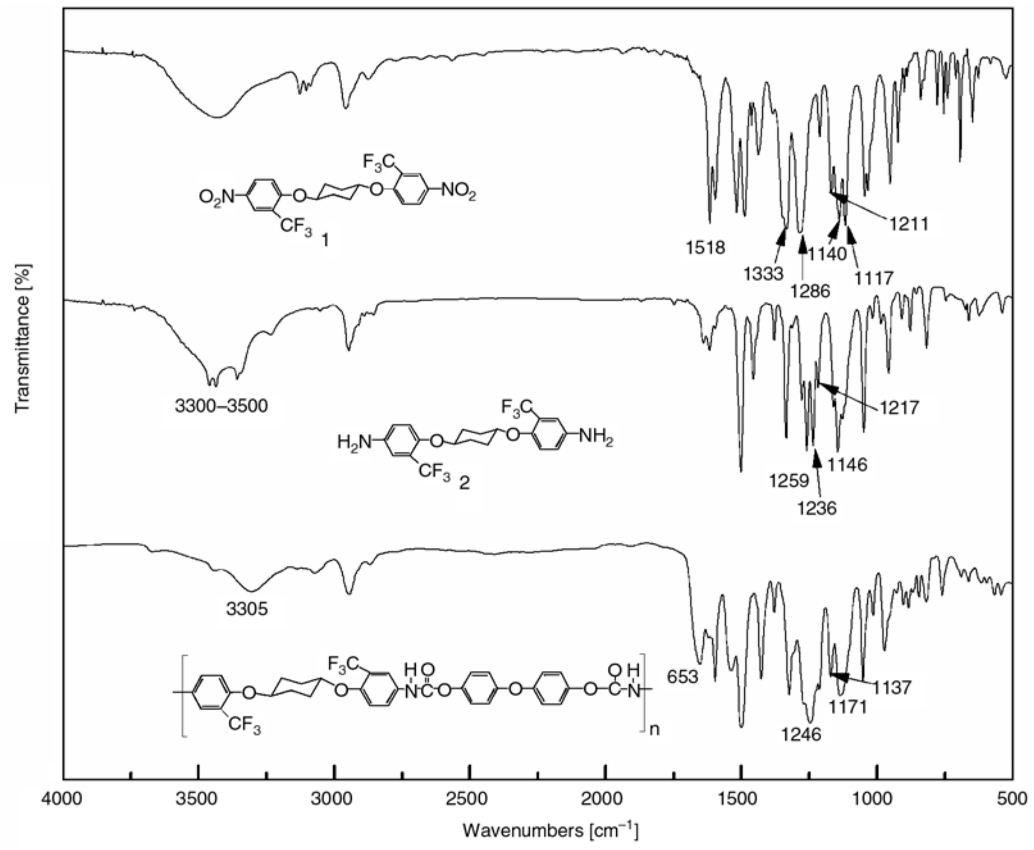

Figure 2. FT-IR spectra of dinitro **1**, diamine **2** and polyamide **4c**

of aromatic and cyclohexane protons of **1** appeared in the region of 7.14–8.56 and 2.03–4.96 ppm respectively; and those of **2** shifted to a higher field between 6.78–7.02 and 1.58–4.45 ppm respectively. The protons H_1 of **1** resonated at the farthest downfield, which is due to the inductive effect of electron withdrawing of $-NO_2$ and $-CF_3$ groups. And the protons H_3 and H_4 affected by the electron donating behavior of ether group shifted to the upfield. After reduction, the H_1 and H_2 of **2** shifted to the upfield because of the electron-donating property of the amino group.

3.2. Polymer synthesis

Polyamides were prepared by Yamazaki-Higashi phosphorylation polyamidation technique [31]. Diamine **2** was polymerized with four different aromatic dicarboxylic acids-TPA, IPA, OBA, and 6FA to produce polyamides **a**, **b**, **c**, and **d**, respectively (Figure 4). The inherent viscosities (Table 1) of the polyamides are in the range of 0.89–1.29 dl/g. The structures of polyamides were confirmed by elemental analysis, FT-IR and ^{1}HNMR spectroscopies. The results of the elemental analyses (Table 1) were almost in good agreement with the calculated values of the proposed structures.

Table 1. Inherent viscosity and elemental analysis of polyamides

Polyamides		Elemental analysis [%] of polyamides				
Code	**η_{inh}^a [dl/g]**	**Formula (formula weight)**		**C**	**H**	**N**
4a	0.90	$(C_{30}H_{28}F_6N_2O_4)_n$	Calcd	60.60	4.75	4.71
		$(594.54)_n$	Found	59.71	4.68	4.77
4b	0.89	$(C_{30}H_{28}F_6N_2O_4)_n$	Calcd	60.60	4.75	4.71
		$(594.54)_n$	Found	59.57	4.62	4.74
4c	1.29	$(C_{36}H_{32}F_6N_2O_5)_n$	Calcd	62.97	4.70	4.08
		$(686.64)_n$	Found	62.04	4.63	4.01
4d	1.18	$(C_{39}H_{32}F_{12}N_2O_4)_n$	Calcd	57.08	3.93	3.41
		$(820.66)_n$	Found	55.72	3.87	3.35

[a]Measured at a concentration of 0.5 g/dl in DMAc at 30°C

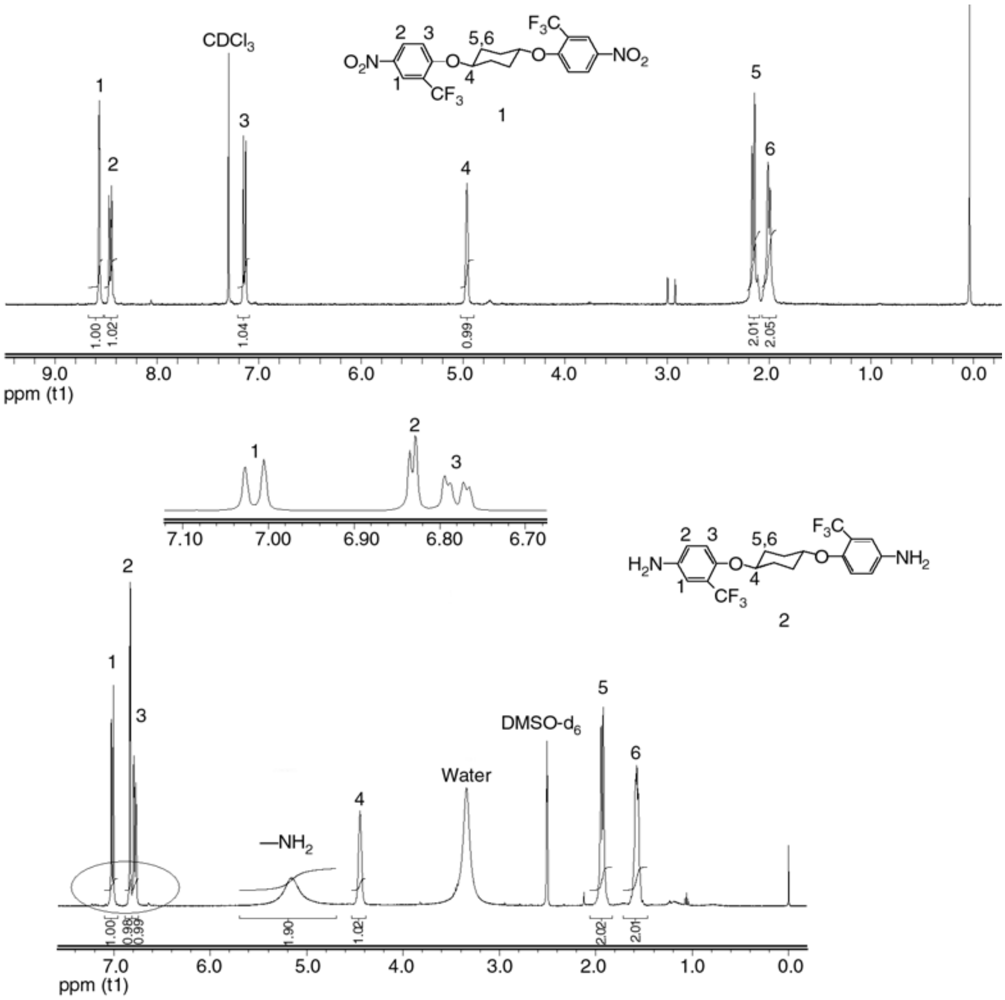

Figure 3. The ¹HMNR spectra of dinitro **1** and diamine **2**

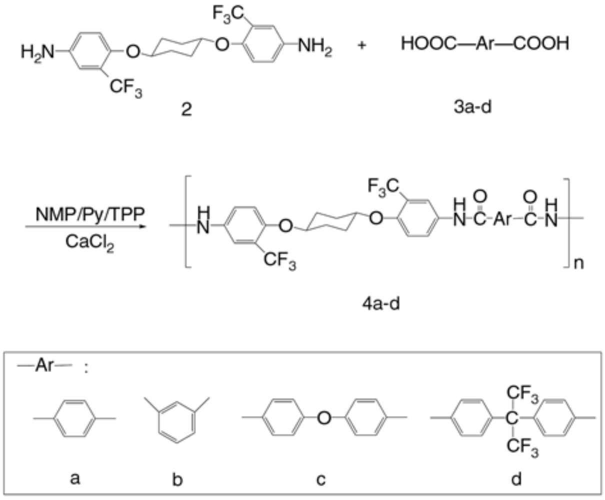

Figure 4. Synthesis of the fluorinated polyamides

The FT-IR spectra of the polyamides showed the characteristic absorptions around 3300 cm^{-1} and 1658 cm^{-1}, which are characteristic of N–H stretching and carbonyl stretching(C=O), respectively. A strong absorption band was observed around 1250 cm^{-1} due to the C–O–C linkage. In addition, the strong C–F absorptions between 1000 and 1200 cm^{-1} are also found in all of the polymers.

All protons in **4b** are identified as number, and their integral values are in good agreement with the anticipated proton numbers. Furthermore the formation of amide groups was verified by ^{1}HNMR, the resonance signals of amide protons appeared at δ10.34. Generally, the protons *ortho*-to the –CF$_3$ group (H$_1$) appear at the farthest downfield in the spectra due to the effect of the electron-withdrawing –CF3 group. In Figure 5, the protons in the cyclohexane (H$_4$, H$_5$, H$_6$) all show absorptions at the farthest upfield area.

3.3. Polymer solubility

Table 2 summarizes the solubilities of the fluorinated polyamides. It can be seen that the obtained polyamides were soluble at a concentration of over 10% in the amide type solvents such as NMP,

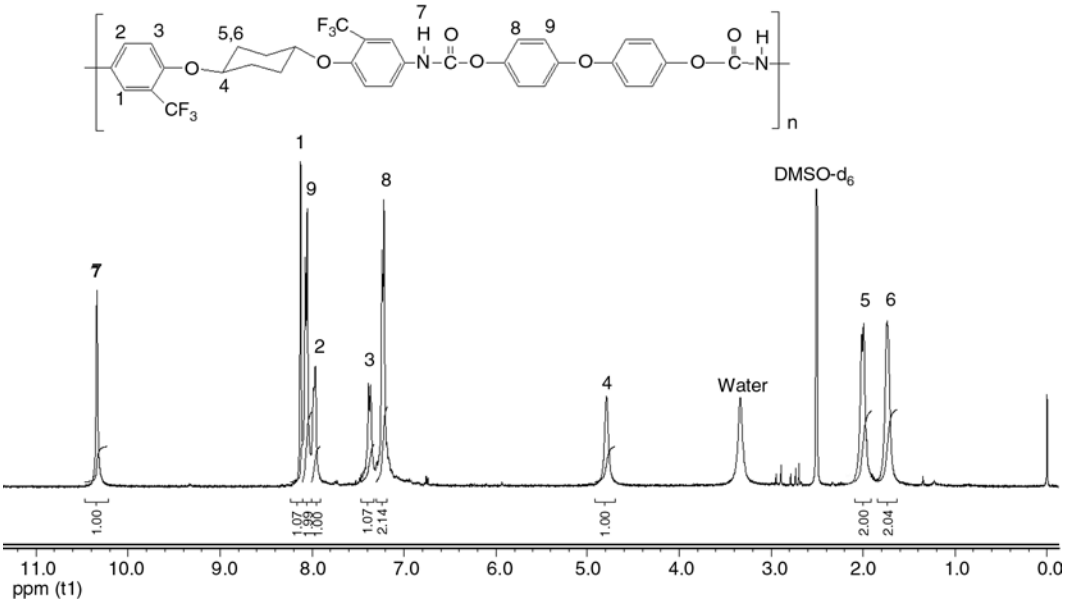

Figure 5. The ^{1}HMNR spectrum of **4c** in DMSO-d_6

Table 2. Solubility behavior of the polyamides

Polymers[a]	Solvents[b]							
	NMP	DMAc	DMF	Py	DMSO	THF	Cy	CH_2Cl_2
4a	+++	+++	+++	++	++	++	+	+
4b	+++	+++	+++	++	++	++	+	+
4c	+++	+++	+++	++	++	++	+	+
4d	+++	+++	+++	++	++	++	+	+

[a] +++, 100 mg sample dissolved in 1 ml solvent (10%); ++, soluble at 5%; +, soluble at 1%

[b] Abbreviations: NMP – *N*-methyl-2-pyrrolidinone; DMAc – *N*,*N*-dimethylacetamide; DMF – *N*,*N*-dimethylformamide; DMSO – dimethyl sulfoxide; Py – pyridine; THF – tetrahydrofuran; Cy – Cyclohexanone

DMAc, and DMF, 5% in pyridine, DMSO and THF, and 1–5% in CH_2Cl_2 and cyclohexanone. Their good solubility and amorphous nature may be apparently due to the presence of the pendent trifluoromethyl groups and ether links in macromolecular chains, which might disrupt the interaction of polymer chains by enlarging the distance between polymer chains, thereby leading to a decrease in packing density and an increase in solubility. The excellent solubility could make these polyamides easy to be processed and benefit their practical applications.

3.4. Mechanical and optical properties

All the obtained polyamides could be readily processed to flexible, creasable, and essentially colorless films by casting from solutions in DMAc. The tensile properties of the polyamides films are summarized in Table 3. Their tensile strengths, elongations at break, and initial moduli of polymer films were in the range of 54–68 MPa, 13.3–15.4%, and 1.6–1.9 GPa, respectively. The optical performances of these fluorinated polymides films are also given in Table 3, and the UV-Vis spectra of these films, are shown in Figure 6. It can be seen from Table 3 that these fluorinated polyamides films exhibited good transparency, the UV cutoff wavelength ($\lambda_{\text{cut off}}$) was in the range of 338–357 nm,and the transparency at 450 nm (T_{450}) was higher than 84%. As expected, the introduction of bulky pendant groups effectively disrupt the dense packing of molecular chains and lead to low color and high optical transparent polymer films.

Table 3. Mechanical and optical properties of the polyamides films

Polymer code	Tensile strength [MPa]	Tensile modulus [GPa]	Elongation at break [%]	$\lambda_{\text{cut off}}$ [nm]	T_{450} [%]
4a	54	1.6	13.3	357	84
4b	64	1.9	14.1	339	87
4c	68	1.6	15.5	335	86
4d	58	1.7	15.4	338	87

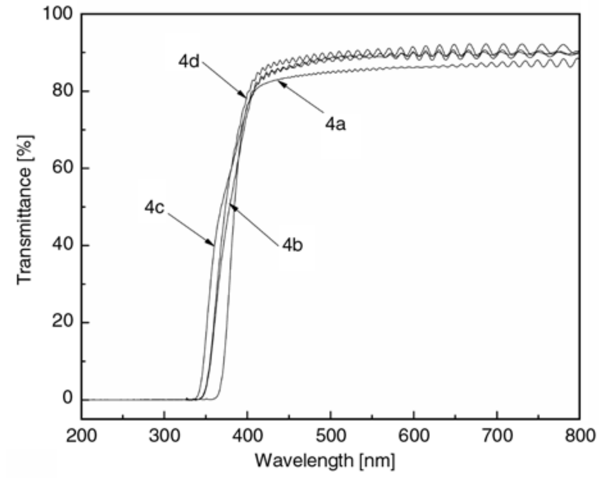

Figure 6. UV-visible spectra of the polyamide films

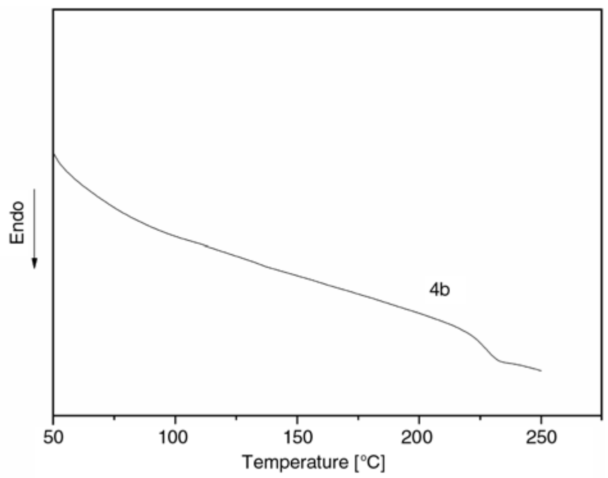

Figure 8. DSC curve of **4b** in air at a scanning rate of 20°C/min

3.5. Thermal properties

The thermal properties of the polyamides were evaluated with TGA and DSC. The results are tabulated in Table 4. Owing to amorphous nature, the T_g values of all the polyamides could be easily identified in the DSC traces. The values for the polyamides were found to be in the range of 203–225°C, depending on the stucture of the chain flexibility and the CF_3 hindrance of the polymer backbones Figure 7 presents typical TGA curves of **3b** and the 10% weight loss temperature (T_{10}) as well as the anaerobic char yield at 800°C in nitrogen were also summarized in Table 4. All the polymers exhibited good thermal stability. Figure 8 shows the DSC curve of **4b** in air atmosphere. The T_{10} of the polyamides stayed between 330–364°C in nitrogen and 308–350°C in air, onset decomposition temperature in the range of 330–342°C, and the char yield of all the polyamides at 800°C were in the range of 40–42%. It implied that these polyamides with trifluoromethyl groups in the polymer backbone showed good thermal stability.

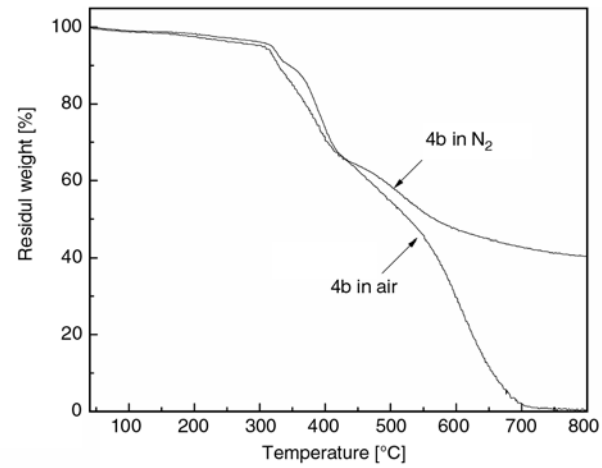

Figure 7. TGA curves of **3b** at a heating rate of 20°C/min

3.6. X-Ray diffraction of the polyamides

The WAXD studies of polyamides **4a–d** indicated that all of these polymers were essentially amorphous as showed in Figure 9. The obtained polymers displayed almost amorphous patterns in nature, this could be attributable to the presence of pendants which reduce attraction between molecules and hindrance macromolecular packing regularly. Generally, these polymers with similar struc-

Table 4. Thermal properties of polyamides

Polymer code	T_g[a] [°C]	T_d[b] [°C]	T_{10}[c][°C]		Char yield[d] [%]
			In N_2	In Air	
4a	219	330	340	330	40
4b	225	331	345	331	41
4c	213	321	356	335	40
4d	224	342	364	350	42

[a] From DSC measurements conducted at a heating rate of 10°C/min

[b] Onset decomposition temperature in TGA at a heating rate of 20°C/min in nitrogen atmosphere

[c] Temperature at 10% weight loss (T_{10}) were determined by TGA in nitrogen atmosphere at a heating rate of 20°C/min

[d] Residual weight [%] at 800°C in nitrogen

Table 5. Dielectric constant and water absorption of various fluorinated polyamides films

Polymer code	Film thickness [µm]	Dielectric constant (dry)				Water absorption [%]
		1 MHz	10 MHz	100 MHz	1000 MHz	
4a	53	2.25	2.10	2.07	2.05	2.33
4b	63	2.88	2.82	2.78	2.75	2.57
4c	47	2.77	2.59	2.56	2.52	2.84
4d	54	2.15	2.03	2.00	1.97	1.96

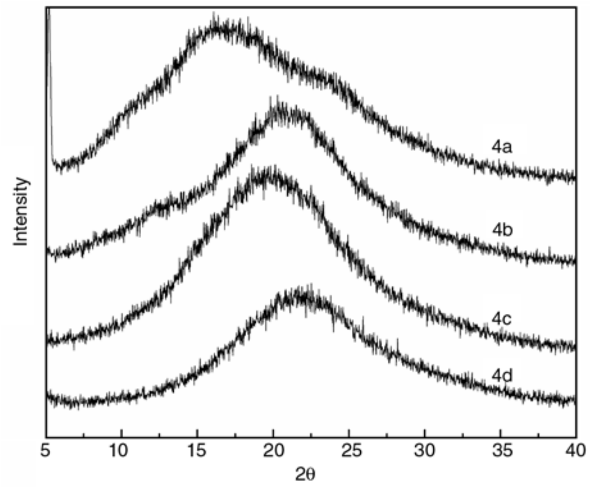

Figure 9. Wide-angle X-ray diffraction patterns of the polyamides

ture containing $–CF_3$ groups are amorphous [32–35].

3.7. Dielectric constant and water absorption

Table 5 summmarizes the results of dielectric constants and moisture absorption. **4d** showed lower dielectric constants of 2.15 at 1 MHz than the others because of the higher fluorine content in the repeat unit. The decreased dielectric constants could be attributed to the presence of bulky CF_3 groups, which resulted in the strong electronegativity of fluorine results in very low polarizability of C–F bonds. In addition, the polymer also exhibited lower water absorptions (1.96–2.84%) due to the hydrophobic nature of the trifluoromethyl groups. The low water absorptions also ensured that these polyamides possess stable dielectric performance.

4. Conclusions

A series of new organosoluble alicyclic polyamides containing trifluoromethyl and cyclohexane groups were prepared by polycondensation. The obtained polyamides show an excellent solubility in many solvents and they could be easily processed to flexible and tough films by casting of their solutions. These polyamides derived from diamine **2** exhibited amorphous nature, excellent optical properties, good mechanical properties, as well as good thermal stability. Moreover, these polyamides display low dielectric constants and water absorption; thus, these obtained polyamides possessed an eminent combination of several desired properties and could be used as potential high-temperature resistant materials for optical or microelectronic applications.

Acknowledgements

The authors would like to thank the National Natural Science Foundation of China (50673017) and Program of Introducing Talents of Discipline to Universities (111-2-04).

References

[1] Cassidy P. E.: Thermally stable polymers. Marcel Dekker, New York (1980).

[2] Yang H. H.: Aromatic high-strength fibers. Wiley, New York (1989).

[3] Tamami B., Yeganeh H.: Synthesis and characterization of novel aromatic polyamides derived from 4-aryl-2,6-bis(4-aminophenyl) pyridines. Polymer, **42**, 415–420 (2001).
DOI: 10.1016/S0032-3861(00)00276-7

[4] Lee H. S., Kim S. Y.: Synthesis of poly(arylene ether amide)s containing CF_3 groups by nitro displacement reaction of AB-type monomers. Macromolecular Rapid Communications, **23**, 666–671 (2002).
DOI: 10.1002/1521-3927(20020801)23:12<665::AID-MARC665>3.0.CO;2-A

[5] Negi Y. S., Suzuki Y-I., Kawamura I., Kakimoto M-A., Imai Y.: Synthesis and characterization of soluble polyamides based on 2,2-bis[4-(4-aminophenoxy) phenyl]hexafluoropropane and 2,2-bis[4-(4-aminophenoxy)phenyl]propane and diacid chlorides. Journal of Polymer Science Part A: Polymer Chemistry, **34**, 1663–1668 (1996).
DOI: 10.1002/(SICI)1099-0518(19960715)34:9<1663::AID-POLA3>3.0.CO;2-T

[6] Varma I. K., Kumar R., Bhattacharyya A. B.: Effect of structure on properties of aromatic polyamides. Journal of Applied Polymer Science, **40**, 531–542 (1990). DOI: 10.1002/app.1990.070400319

[7] Wu S-C., Shu C-F.: Synthesis and properties of soluble aromatic polyamides derived from 2,2'-bis(4-carboxyphenoxy)-9,9'-spirobifluorene. Journal of Polymer Science Part A: Polymer Chemistry, **41**, 1160–1166 (2003). DOI: 10.1002/pola.10657

[8] Liaw D-J., Liaw B-Y., Yang C-M.: Synthesis and properties of new polyamides based on bis[4-(4-aminophenoxy)phenyl]diphenylmethane. Macromolecules, **32**, 7248–7250 (1999). DOI: 10.1021/ma990545h

[9] Mehdipour-Ataei S., Heidari H.: Synthesis and characterization of novel soluble and thermally stable polyamides based on pyridine monomer. Macromolecular Symposia, **193**, 159–168 (2003). DOI: 10.1002/masy.200390049

[10] Feger C., Khojasteh M. M., McGrath J. E.: Polyimides: materials, chemistry, and characterization. Elsevier, Amsterdam (1989).

[11] Liaw D-J., Liaw B-Y.: Synthesis and properties of new polyimides derived from 1,1-bis[4-(4-aminophenoxy)phenyl]cyclododecane. Polymer, **40**, 3183–3189 (1999). DOI: 10.1016/S0032-3861(98)00494-7

[12] Cheng L., Jian X. G., Mao S. Z.: Aromatic polyamides derived from unsymmetrical diamines containing the phthalazinone moiety. Journal of Polymer Science Part A: Polymer Chemistry, **40**, 3489–3496 (2002). DOI: 10.1002/pola.10426

[13] Liaw D-J., Wang K-L., Chang F-C.: Novel organosoluble poly(pyridine-imide) with pendent pyrene group: Synthesis, thermal, optical, electrochemical, electrochromic, and protonation characterization. Macromolecules, **40**, 3568–3574 (2007). DOI: 10.1021/ma062546x

[14] Yang C. P., Su Y. Y.: Properties of organosoluble aromatic polyimides from 3'-trifluoromethyl-3,4'-oxydianiline. Polymer, **44**, 6311–6322 (2003). DOI: 10.1016/S0032-3861(03)00684-0

[15] Eastmond G. C., Paprotny J., Irwin R. S.: Melt-processable poly(ether imide)s based on catechol bis(ether anhydride). Macromolecules, **29**, 1382–1388 (1996). DOI: 10.1021/ma951007h

[16] Sciannamea V., Catala J-M., Jérôme R., Detrembleur C.: Controlled radical polymerization of styrene mediated by the *C*-phenyl-*N*-tert-butylnitrone/AIBN pair: Kinetics and electron spin resonance analysis. Journal of Polymer Science Part A: Polymer Chemistry, **45**, 1219–1235 (2007). DOI: 10.1002/pola.21889

[17] Yang C-P., Hsiao S-H., Yang H-W.: Synthesis and characterization of aromatic polyamides based on a bis(ether-carboxylic acid) or a dietheramine derived from tert-butylhydroquinone. Macromolecular Chemistry and Physics, **200**, 1528–1534 (1999). DOI: 10.1002/(SICI)1521-3935(19990601)200:6<1528::AID-MACP1528>3.0.CO;2-D

[18] Kim H-S., Kim Y-H., Ahn S-H., Kwon S-K.: Synthesis and characterization of highly soluble and oxygen permeable new polyimides bearing a noncoplanar twisted biphenyl unit containing tert-butylphenyl or trimethylsilyl phenyl groups. Macromolecules, **36**, 2327–2332 (2003). DOI: 10.1021/ma0214557

[19] Yang C-P., Lin J-H.: Syntheses and properties of aromatic polyamides and polyimides based on 3,3-bis[4-(4-aminophenoxy)phenyl]-phthalimidine. Polymer, **36**, 2607–2614 (1995). DOI: 10.1016/0032-3861(95)91208-O

[20] Espeso J. F., de la Campa J. G., Lozano A. E., de Abajo J.: Synthesis and characterization of new soluble aromatic polyamides based on 4-(1-adamantyl)-1, 3-bis(4-aminophenoxy)benzene. Journal of Polymer Science Part A: Polymer Chemistry, **38**, 1014–1023 (2000). DOI: 10.1002/(SICI)1099-0518(20000315)38:6<1014::AID-POLA11>3.0.CO;2-H

[21] Espeso J. F., Ferrero E., de la Campa J. G., Lozano A. E., de Abajo J.: Synthesis and characterization of new soluble aromatic polyamides derived from 1,4-Bis(4-carboxyphenoxy)-2, 5-di-*tert*-butylbenzene. Journal of Polymer Science Part A: Polymer Chemistry, **39**, 475–485 (2001). DOI: 10.1002/1099-0518(20010215)39:4<475::AID-POLA1016>3.0.CO;2-I

[22] Salamone J. C.: Polymeric material encyclopedia. CRC Press, New York (1996).

[23] Yang C-P., Chen R-S., Yu C-W.: Preparation and characterization of organosoluble polyimides based on 1,1-bis[4-(3,4-aminophenoxy)phenyl]cyclohexane and commercial aromatic dianhydrides. Journal of Applied Polymer Science, **82**, 2750–2759 (2001). DOI: 10.1002/app.2128

[24] Takashi K., Atsushi S., Shoji T.: New aromatic diamine and polyimide. Japanese Patent 2000-297067, Japan (2000).

[25] Myung B. Y., Kim J. J., Yoon T. H.: Synthesis and characterization of novel 3,6-di[3',5'-bis(trifluoromethyl)phenyl]pyromellitic dianhydride for polyimide synthesis. Journal of Polymer Science Part A: Polymer Chemistry, **40**, 4217–4227 (2002). DOI: 10.1002/pola.10512

[26] Myung B. Y., Kim J. S., Kim J. J., Yoon T. H.: Synthesis and characterization of novel polyimides with 2,2-bis[4(4-aminophenoxy)phenyl]phthalein-3',5'-bis(trifluoromethyl)anilide. Journal of Polymer Science Part A: Polymer Chemistry, **41**, 3361–3374 (2003). DOI: 10.1002/pola.10924

[27] Banerjee S., Madhra M. K., Salunke A. K., Jaiswal D. K.: Synthesis and properties of fluorinated polyimides. 3. Derived from novel 1,3-bis[3'-trifluoromethyl-4'(4"-amino benzoxy) benzyl] benzene and 4,4-bis[3'-trifluoromethyl-4'(4-amino benzoxy) benzyl] biphenyl. Polymer, **44**, 613–622 (2003). DOI: 10.1016/S0032-3861(02)00801-7

[28] Wang C-Y., Li P-H., Li G., Jiang J-M.: High optical transparency and low dielectric constant of novel organosoluble poly(ether ketone amide)s derived from an unsymmetrical diamine containing trifluoromethyl and methyl pendant groups. Colloid and Polymer Science, **287**, 495–500 (2009). DOI: 10.1007/s00396-009-2007-2

[29] Liaw D-J., Chen W-H., Hu C-K., Lee K-R., Lai J-Y.: High optical transparency, low dielectric constant and light color of novel organosoluble polyamides with bulky alicyclic pendent group. Polymer, **48**, 6571–6580 (2007). DOI: 10.1016/j.polymer.2007.08.041

[30] Hsiao S-H., Yang C-P., Tsai C-Y., Liou G-S.: A novel class of organosoluble and light-colored fluorinated polyamides derived from 2,2'-bis(4-amino-2-trifluoromethylphenoxy)biphenyl or 2,2'-bis(4-amino-2-trifluoromethylphenoxy)-1,1'-binaphthyl. European Polymer Journal, **40**, 1081–1094 (2004). DOI: 10.1016/j.eurpolymj.2004.01.001

[31] Yamazaki N., Matsumoto M., Higashi F.: Studies on reactions of the N-phosphonium salts of pyridines. XIV. Wholly aromatic polyamides by the direct polycondensation reaction by using phosphites in the presence of metal salts. Journal of Polymer Science: Polymer Chemistry Edition, **13**, 1373–1380 (1975). DOI: 10.1002/pol.1975.170130609

[32] Sheng S-R., Pei X-L., Huang Z-Z., Liu X-L., Song C-S.: Novel soluble fluorinated aromatic polyamides derived from 2-(4-trifluoromethylphenoxy)terephthaloyl chloride with various aromatic diamines. European Polymer Journal, **45**, 230–236 (2009). DOI: 10.1016/j.eurpolymj.2008.10.023

[33] Qiu Z., Wang J., Zhang Q., Zhang S., Ding M., Gao L.: Synthesis and properties of soluble polyimides based on isomeric ditrifluoromethyl substituted 1,4-bis(4-aminophenoxy)benzene. Polymer, **47**, 8444–8452 (2006). DOI: 10.1016/j.polymer.2006.10.031

[34] Liu B. J., Hu W., Chen C. H., Jiang Z. H., Zhang W. J., Wu Z. G., Matsumoto T.: Soluble aromatic poly(ether ketone)s with a pendant 3,5-ditrifluoromethylphenyl group. Polymer, **45**, 3241–3247 (2004). DOI: 10.1016/j.polymer.2004.03.015

[35] Yang C-P., Chen Y-P., Woo E. M: Thermal behavior of 1,4-bis(4-trimellitimido-2-trifluoromethyl phenoxy)benzene (DIDA) solvated with polar organic solvents and properties of DIDA-based poly(amide-imide)s. Polymer, **45**, 5279–5293 (2004). DOI: 10.1016/j.polymer.2004.05.035

eXPRESS Polymer Letters Vol.3, No.11 (2009) 713–723
Available online at www.expresspolymlett.com
DOI: 10.3144/expresspolymlett.2009.89

Theoretical prediction of hysteretic rubber friction in ball on plate configuration by finite element method

L. Pálfi[*], *T. Goda, K. Váradi*

Department of Machine and Product Design, Budapest University of Technology and Economics, Műegyetem rkp. 3., H-1111, Budapest, Hungary

Received 15 June 2009; accepted in revised form 26 August 2009

Abstract. This paper has investigated theoretically the influence of sliding speed and temperature on the hysteretic friction in case of a smooth, reciprocating steel ball sliding on smooth rubber plate by finite element method (FEM). Generalized Maxwell-models combined with Mooney-Rivlin model have been used to describe the material behaviour of the ethylene-propylene-diene-monomer (EPDM) rubber studied. Additionally, the effect of the technique applied at the parameter identification of the material model and the number of Maxwell elements on the coefficient of friction (COF) was also investigated. Finally, the open parameter of the Greenwood-Tabor analytical model has been determined from a fit to the FE results. By fitting, as usual, the Maxwell-model to the storage modulus master curve the predicted COF, in a broad frequency range, will be underestimated even in case of 40-term Maxwell-model. To obtain more accurate numerical prediction or to provide an upper limit for the hysteretic friction, in the interesting frequency range, the Maxwell parameters should be determined, as proposed, from a fit to the measured loss factor master curve. This conclusion can be generalized for all the FE simulations where the hysteresis plays an important role.

Keywords: *rubber, FE modelling and simulation, hysteretic friction, viscoelasticity*

1. Introduction

In the design of many mechanical engineering applications it is important to know the mechanical behaviour and tribological properties of components sliding on each other. The situation is the same if one of the sliding surfaces is made of rubber or a rubber-like material, such as sliding seals contacting with a metal or polymer surface, sliding contact between a windscreen wiper and the windscreen, or contact between a tyre and the asphalt. For the majority of sliding components applied in mechanical engineering practice, the non-lubricated operation is avoided; however, the quantity of lubricant required in maintenance free machine components is even more frequently minimized by special coatings. In the event that there is no lubricant between the rubber and the counter surface, friction is due to two physical phenomena. One of them is adhesion between the surfaces, the other one is hysteresis loss in the rubber [1–4]. For instance, if the rubber slides on a rough surface which is rigid compared to the rubber, the asperities of the counter surface repeatedly deform the surface of the rubber, leading to energy loss due to the internal friction (hysteresis) of the rubber. In this case, the energy transformed into heat as a consequence of hysteresis must be continuously supplemented if the sliding speed is intended to be constant. The majority of rubbing components made of rubber and applied in machine design operate under lubrication, to separate rubbing surfaces and thereby to reduce the impact of adhesion, as well as to reduce the exciting effect of asperities by filling up the valleys with the lubricant. When

---

[*] Corresponding author, e-mail: palfi.laszlo@gt3.bme.hu

lubricant is used, the lubricant itself also acts as a source of friction because force is needed for shearing of the fluid film. In general, the fluid film is extremely thin, therefore in reality boundary lubrication occurs, where the source of friction is the shearing of the fluid film and of the boundary layer.

In the literature, a number of articles deal with the analytic and semi-analytic determination of friction force induced by from hysteresis. Grosch [1] perform pioneering work by revealing that the two main sources of the friction force are adhesion between the surfaces and the energy loss generated in the material, that is, hysteresis. In addition, he stated that both physical phenomena are closely connected to internal friction (hysteresis) of the rubber.

Persson [2] and Klüppel and Heinrich [4] studied rubber when it is sliding on a hard, rough substrate and the surface asperities of the substrate exert oscillating forces on the rubber surface leading to energy 'dissipation' via the internal friction of the rubber. This contribution to the friction force was estimated and the results were compared with the experimental data of Grosch. Persson concluded that rubber friction on rough surfaces, in presence of lubricant, is mainly due to the viscoelastic deformations of rubber.

In spite of intensive research work in the subject, so far there have been only few attempts to predict hysteretic friction by the finite element (FE) method. For instance, in [5, 6] the hysteretic friction at asperity level was studied by FE technique.

When modelling rough surfaces the topography of the 'real' surface can be replaced by sine waves or their combination. In [7] the rough surface was modelled by a single sine wave, while [8] presented a study on the combination of sine waves by using the repetitive symmetry. In the latter case, the effect of the viscoelastic material model on the predicted coefficient of friction was also investigated. In addition, [8] consists of recommendations for the parameter identification of the generalized Maxwell-models.

In [9], Felhős *et al.* analysed friction force arising from hysteresis in case of a ball rolling on a rubber plate. Measurements were also modelled by FE method, where a 15-term generalized Maxwell-model – fitted to the storage modulus master curve yielded by DMTA measurement – was used to describe viscoelastic material behaviour. His measurement results showed good agreement with the results of FE simulation.

In [10], the authors investigated the measurement configuration to be modelled in this study at three sliding speeds. The measurement was modelled by FE technique as well and it was investigated, using a 40-term generalized Maxwell-model fitted to the measured storage modulus master curve, what proportion of the friction force came from hysteresis. The coefficient of friction (COF) characterising lubricant shearing was determined by an iterative method and integrated into the FE model, using a prescribed Coulomb type coefficient of friction.

In measurements belonging to the current FE study (see [10]) the rubber/metal contact pair was lubricated. Consequently, the effect of adhesion on friction force can be neglected and thus rubber friction is, first of all, due to hysteresis at macroscopic and microscopic level, fluid shearing and boundary lubrication. This study is intended to estimate, using the FE technique, the hysteresis dissipation excited by an ideally smooth steel ball (macroscopic hysteretic friction) performing reciprocating sliding motion in the function of sliding speed and temperature by applying various Maxwell-models. In other words, the aim of FE analysis is to estimate contribution of the macroscopic hysteresis to the friction force.

2. Description of the FE model

The experiment is intended to determine, on the one hand, the magnitude of friction force generated by a steel ball sliding on a rubber plate, as a consequence of the internal friction of the rubber (hysteresis), at various sliding speeds and temperatures; and on the other hand, to establish how calculation results are influenced by the technique applied for parameter identification of generalized Maxwell-models – used for the FE modelling of rubber-like materials and describing viscoelastic behaviour – and by the number of the Maxwell elements. The configuration studied consists of a steel bearing ball and a rubber plate [10] where the steel ball of 2 mm diameter was pressed into an EPDM rubber plate of 10 mm×4 mm×2 mm. Then the ball was forced to perform reciprocating motion with an amplitude of $A = 0.3$ mm at different, sinusoidally varying speeds through six cycles. The normal force was $F_n = 100$ mN while the maximums of the sinusoidally varying sliding speeds were $v_{\max}$ = 0.01, 0.1, 1, 10, and 100 mm/s.

The ball, pressed into the surface of the rubber and sliding thereon, generates various COFs due to the hysteresis depending on the excited volume and on the sliding speed, that is, the excitation frequency. In order to predict the friction resistance caused by hysteresis, 3D FE modes were developed in the MSC.MARC FE system [11].

In order to describe the viscoelastic behaviour of rubber, a 15-term and a 40-term generalized Maxwell-model were used, which were produced by being fitted to storage modulus master curves determined by DMTA measurements and pertaining to –50, +25 and +150°C, respectively, and, through subsequent manual modification, by being fitted to a loss factor master curve.

The FE model was built in MSC.MARC finite element system. The rubber plate was modelled using incompressible ($\upsilon = 0.5$) elements, whereas the steel ball was modelled as an ideally rigid component. To spare with the CPU time only half of the rubber plate was modelled using symmetry condition, so the nodes in the symmetry plane were fixed in *z*-direction (Figure 1). The bottom of the rubber plate was fixed, i.e. the nodes on this plane were constrained in *x*-, *y*- and *z*-direction.

At first, the steel ball was pressed downwards (in negative *y*-direction) into the rubber plate with the force specified, that was built up linearly. Afterwards, the ball was drawn horizontally (in negative *x*-direction) at sinusoidally varying speed according to the measurement [10], at an amplitude of $A = 0.3$ mm, through six cycles. Figure 2 shows the position of the ball as a function of time in the case of a maximum sliding speed of 1 mm/s. The excitation frequency induced by the ball performing reciprocating motion can be estimated by the Equation (1):

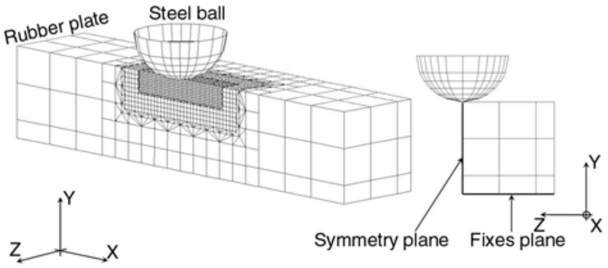

Figure 1. FE model (only half of the rubber plate was modelled due to the symmetry)

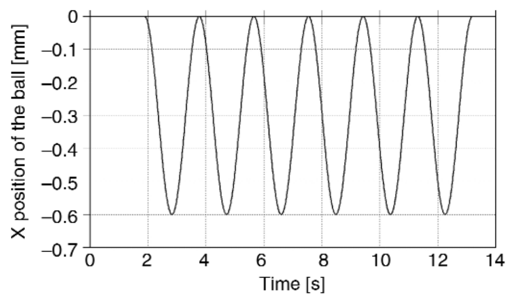

Figure 2. Displacement control curve in the direction *x*, pertaining to the maximum sliding speed of $v_{\max}$ = 1 mm/s

$$f = \frac{2}{2 \cdot \dfrac{\pi}{\omega}} = \frac{v_{\max}}{\pi \cdot A} \tag{1}$$

where ω is the angular frequency, and A is the amplitude of the reciprocating sliding ball. The grey band in Figures 4–9 indicates the range between the lowest and the highest frequency to be calculated from the equation above.

2.1. Viscoelastic material model

In order to be able to model the mechanical behaviour of structural components made of rubber or rubber-like material, first of all a material model is required which can describe both the static and dynamic behaviour of the material at the same time. The mechanical behaviour of rubber-like materials is principally characterized by a non-linear stress-strain curve and time and temperature dependency. In the present study, a large strain generalized Maxwell model (Figure 3) was used to describe the complex material behaviour of rubber. The short-time (instantaneous) behavior of the generalized Maxwell-model applied is specified by an energy density function (W^0) that is given, in our case, by a two-term Mooney-Rivlin material model. Thus our

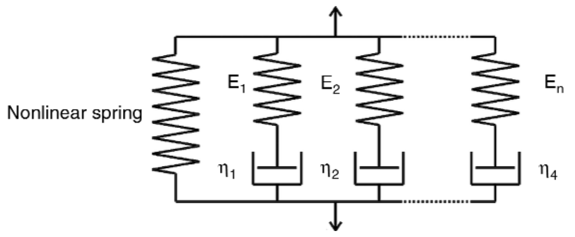

Figure 3. The n-term generalized Maxwell-model (E_i – elastic modulus of the *i*-th spring, η_i – viscosity of the *i*-th dashpot)

large-strain viscoelastic model shows nonlinearity between stresses and strains that, at the same time, depends on time. The instantaneous strain energy density is distributed among the branches of our spring-dashpot model by assuming that the instantaneous strain energy in the *i*-th Maxwell element can be calculated by Equation (2):

$$W_i = e_i \cdot W^0 \tag{2}$$

where e_i is the non-dimensional energy parameter of the *i*-th Maxwell element and W^0 is the instantaneous strain energy defined by the Mooney-Rivlin model. The interrelation among the energy parameters can be written according to Equation (3):

$$e_\infty + \sum_{i=1}^{N} e_i = 1 \tag{3}$$

where e_∞ is the energy parameter of the spring – that determines the relaxed response of the rubber – connected parallel to the Maxwell elements and N is the number of the Maxwell branches. As it is resulted from the above expressions the second Piola-Kirchhoff stress response of the generalized Maxwell model applied, in case of uniaxial tension/compression, can be expressed by Equations (4) and (5):

$$S_i(t) = S_\infty(t) + \sum_{i=1}^{M} S_i(t) \tag{4}$$

$$S_i(t) = \int_{\tau=0}^{\tau=t} e_i \cdot S^0(t) \cdot e^{-\frac{(t-\tau)}{\lambda}} \, \mathrm{d}\tau \tag{5}$$

where $S_\infty(t)$ is the stress in the separate spring, $S_i(t)$ is the stress in the *i*-th Maxwell element or branch, $S^0(t)$ is the stress response of the model for instantaneous deformations and λ_i is the relaxation time of the *i*-th Maxwell element. As it is known from continuum mechanics stresses can be calculated by differentiation of the proper strain energy density function with respect to the Green-Lagrange strains. For instance, $S^0(t)$ is obtained by differentiation of W^0. For more detail on the large strain viscoelastic model applied see [11].

The DMTA measurement results of EPDM rubber in [9] were used for producing the *n*-term Maxwell-model.

DMTA measurements yield storage modulus vs. frequency and loss factor vs. frequency isotherms, from which a storage modulus vs. frequency and a loss factor vs. frequency master curve can be constructed at the previously selected reference temperature using the time-temperature superposition principle. These master curves show the mechanical properties of rubber in a broad frequency range at the reference temperature. The ViscoData software [12] was applied to fit 15- and 40-term generalized Maxwell-models to the storage modulus master curve produced. In order to take all the three different temperatures into account, three master curves were produced for each material model, and the material models were fitted to them separately. The reason why the authors used three different material model at the three different temperatures (T = –50, 25 and 150°C) is that the WLF equation with universal constants (C_1 = 17.4, C_2 = 51.6°C) provided inaccurate material behavior at temperatures significantly larger than the glass transition temperature ($T_g \approx$ –45°C). The WLF equation was able to describe the temperature dependency of the material behavior when the temperature is close to T_g. At temperatures far away T_g (eg. at T = 25°C) WLF overestimated considerably the horizontal shift needed. Instead of making attempt to find proper C_1, C_2 constants for the WLF equation three different master curves were created at the three different temperatures studied. Figure 4 and Figure 5 show the measured and fitted storage modulus vs. frequency curves, while Figure 6 and Figure 7 show the loss factor vs. frequency curves in case of the 15- and 40-term generalized Maxwell-models fitted to the storage modulus, at three different temperatures.

The magnitude of hysteretic friction is basically determined by two factors: one of them is the magnitude of the loss factor, and the other is the excited volume. Hysteretic dissipation is determined by the joint effect of these two factors. The first factor can obviously be handled by a good correspondence between the measured loss factor vs. frequency curve and the one used in modelling; while the second factor is determined by the storage modulus, that is, how rigid the material is and how deeply the rigid counter surface can penetrate into it, meaning the volume forced to deform.

It is intended to produce a viscoelastic model which closely approaches both the storage modulus vs. frequency and the loss factor vs. frequency curves measured.

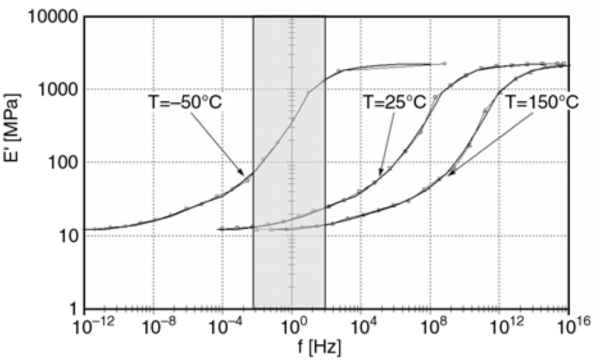

Figure 4. Comparison of the measured and simulated storage modulus vs. frequency curves in case of a 15-term generalized Maxwell-model fitted to the storage modulus (strain amplitude = 0.01%).
— measurement T = –50°C, -◇-T = –50°C, fitted to the E', — measurement T = 25°C, -□- T = 25°C, fitted to the E', — measurement T = 150°C, -△- T = 150°C, fitted to the E'.

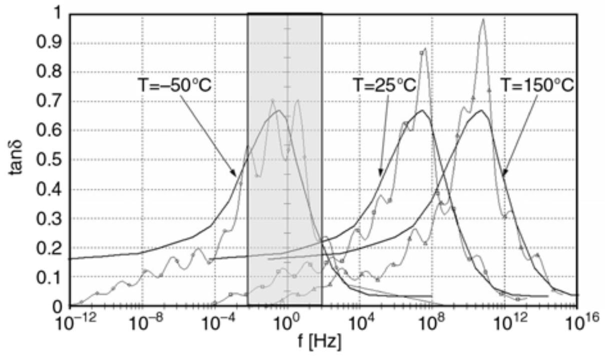

Figure 6. Comparison of the measured and simulated loss factor vs. frequency curves in case of a 15-term generalized Maxwell-model fitted to the storage modulus.
— measurement T = –50°C, -◇-T = –50°C, fitted to the tanδ, — measurement T = 25°C, -□- T = 25°C, fitted to the tanδ, — measurement T = 150°C, -△- T = 150°C, fitted to the tanδ.

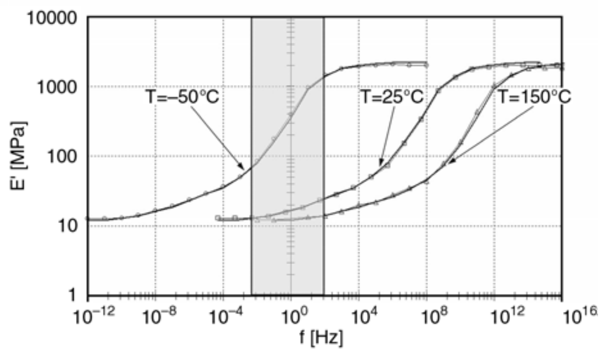

Figure 5. Comparison of the measured and simulated storage modulus vs. frequency curves in case of a 40-term generalized Maxwell-model fitted to the storage modulus (strain amplitude = 0.01%).
— measurement T = –50°C, -◇-T = –50°C, fitted to the E', — measurement T = 25°C, -□- T = 25°C, fitted to the E', — measurement T = 150°C, -△- T = 150°C, fitted to the E'.

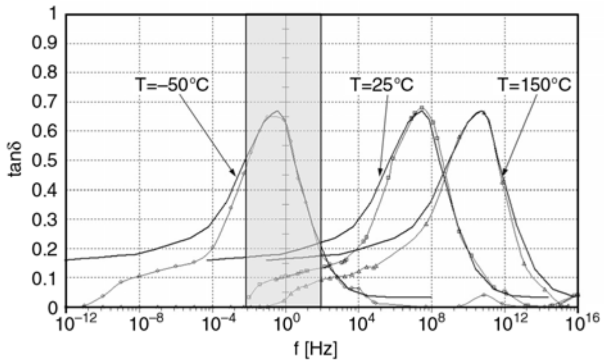

Figure 7. Comparison of the measured and simulated loss factor vs. frequency curves in case of a 40-term generalized Maxwell-model fitted to the storage modulus.
— measurement T = –50°C, -◇-T = –50°C, fitted to the tanδ, — measurement T = 25°C, -□- T = 25°C, fitted to the tanδ, — measurement T = 150°C, -△- T = 150°C, fitted to the tanδ.

In case of the 15-term generalized Maxwell-model it can be observed that there is good correspondence between the measurement and the fitted models as regards the storage modulus (Figure 4), but the loss factor produces large oscillation (Figure 6). By increasing the number of Maxwell elements to 40, the fluctuation becomes smaller; however, even in this case, the model strongly underestimates the value of the loss factor within a broad frequency range (Figure 7). It can be stated that the 15-term generalized Maxwell-model cannot describe, with adequate accuracy, either the nature of the loss factor or its numerical value. The generalized Maxwell-model fitted to a 40-term storage modulus already properly represents the loss factor vs. frequency curve determined from the measurement in terms of quality – and also in terms of quantity at most frequencies – but it still cannot provide an adequate numerical solution in case of certain frequencies. It can be further stated that following adjustment of the material model it is not sufficient to be satisfied with a good correspondence between the storage modulus curves of the measured and fitted material models, but it is necessary to check the loss factor vs. frequency curve as well. No reliable hysteretic dissipation can be calculated by the FE technique unless the material model can properly represent both the storage modulus and loss factor master curves determined by measurement. In order to model the measured

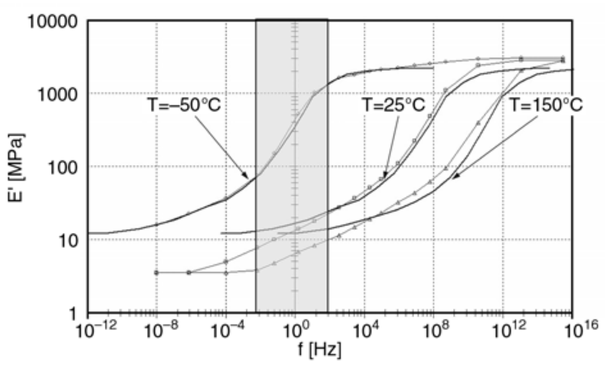

Figure 8. Comparison of the measured and simulated storage modulus vs. frequency curves in case of a 40-term generalized Maxwell-model fitted to the loss factor (strain amplitude = 0.01%).
— measurement $T = -50$°C, -◇-$T = -50$°C, fitted to the E', — measurement $T = 25$°C, -□- $T = 25$°C, fitted to the E', — measurement $T = 150$°C, -△- $T = 150$°C, fitted to the E'.

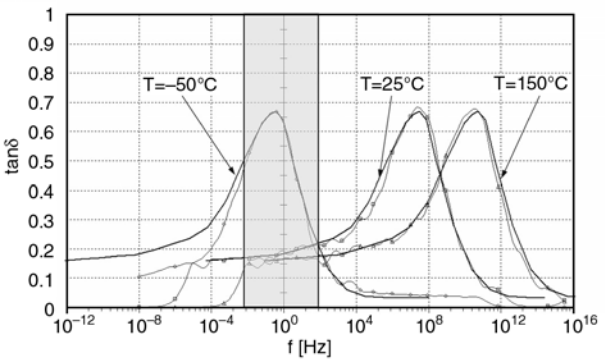

Figure 9. Comparison of the measured and simulated loss factor vs. frequency curves in case of a 40-term generalized Maxwell-model fitted to the loss factor.
— measurement $T = -50$°C, -◇-$T = -50$°C, fitted to the tanδ, — measurement $T = 25$°C, -□-$T = 25$°C, fitted to the tanδ, — measurement $T = 150$°C, -△- $T = 150$°C, fitted to the tanδ.

material behaviour more accurately, a 40-term Maxwell-model was produced by manual modification [8], fitted to the loss factor. Figure 8 and Figure 9 show, at three different temperatures, the measured storage modulus vs. frequency and loss factor vs. frequency curves of the 40-term generalized Maxwell-model and those fitted to the loss factor.

In the course of adjustment to the loss factor, correspondence with the storage modulus curve will not be as good as in the case of adjusting the material model to the measured storage modulus master curve. The parameters of the material model can be considered as optimal when the model can describe, with acceptable accuracy, both master curves (E', tanδ) determined by measurement. Figure 9 shows that as a result of manual modification, the material model can describe the measured tanδ curve with acceptable accuracy. Furthermore, it can be stated in the case of all the three Maxwell-models that the material models cannot describe the storage modulus and the loss factor master curves with constant accuracy within the entire frequency range, therefore care must be taken at what excitation frequency and at what temperature the material model is used.

2.2. Non-linear material model

In the FE model, the non-linear stress-strain curve of rubber was defined by the frequently applied Mooney-Rivlin material law with two parameters. The two Mooney-Rivlin parameters were defined on the basis of [11], using the Equations (6) and (7):

$$E_0 = 6 \cdot (C_{01} + C_{10}) \tag{6}$$

$$\frac{C_{01}}{C_{10}} = \frac{1}{4} \tag{7}$$

where E_0 is the glassy modulus. The two parameters used for the calculations were C_{10} = 289.33 MPa and C_{01} = 72.33 MPa in case of the 15- and 40-term generalized Maxwell-models fitted to the storage modulus; their value was C_{10} = 406.66 MPa and C_{01} = 101.66 MPa, respectively, in case of the generalized Maxwell-model fitted to the loss factor. The non-dimensional energy parameters (e_i) of the Maxwell model fitted to the loss factor (tanδ) master curve were obtained by manual modification from the energy parameters of the Maxwell model fitted to the storage modulus master curve. Due to this modification the sum of the energy parameters of the Maxwell elements ($\sum_{i=1}^{40} e_i$) has been changed. Consequently, if we used the same glassy Mooney parameters in both cases, we would obtain an accurate relaxed modulus at the Maxwell model fitted to E' while, at the Maxwell model fitted to tanδ, the relaxed modulus would be considerably underestimated in the interesting frequency range. To minimize this underestimation i.e. to approach E' the real values, the glassy Mooney parameters have been changed. Thus we obtain higher glassy modulus than the measured one but the agreement, within the interesting frequency range, between the modeled and measured E' values will be better than in the case of same Mooney parameters. In our case, the change in $\sum_{i=1}^{40} e_i$ at –50°C was smaller than at 25 and 150°C as it can be seen in Figure 8. At T = 25°C (see Figure 7) the Maxwell model fitted to the E' master curve by ViscoData, contrary to the measurement, provides zero or very small loss factor values at low frequencies. As it can be seen in Figure 9 the new model (fitted to tanδ) created by the manual modification of Maxwell parameters provided by ViscoData shows good agreement with the measured tanδ curve. During creation of the new material model authors had to redistribute one part of the relaxation times also.

3. Results and discussion

3.1. FE results

Tables 1–3 show the penetration depths (h) and the radius of the contact area (a) calculated by the FE technique and the COFs induced by hysteresis ($\mu_{hysteresis}$). In case of the 15-term Maxwell-model it can be observed that at –50°C, the penetration depth of the ball reduces from 9.7 to 1.78 μm as the speed increases, due to the fact that the storage modulus of the material rises as the speed increases. For similar reasons, a decrease of penetration depth by the increase of speed can be observed in case of all the material models and temperatures applied. In case of the 15- and 40-term material models fitted to the storage modulus, the value of the penetration depth is approximately the same, but in case of the 40-term material model fitted to the loss factor, penetration depth may be as much as 60% bigger at low speeds as a result of manual modification. Taking speeds into consideration, it can bee stated that the biggest penetration values can be calculated at 150°C. However, as it can be seen in Table 1 and 2, at low speeds (v = 0.01 and 0.1 mm/s) differences between the penetration values calculated at T = 25 and 150°C are within accuracy of the numerical solution.

As regards COFs resulting from hysteresis, it can be stated that in case of material models fitted to the storage modulus the FE model surely underestimates hysteresis as there is a considerable difference between the loss factor curves measured and those defined by the material model. Exceptions only include the COFs provided at –50°C by the 40-term Maxwell-model adjusted to E' (see Table 2). In this case, there is good correspondence between the measured and the simulated material behaviour both as regards E' and tanδ (Figure 5 and

Table 1. Values of the penetration depth (h), radius of the contact area (a) and the hysteretic coefficient of friction ($\mu_{hysteresis}$) in case of 15-term Maxwell-model fitted to the measured storage modulus master curve

Temperature [°C]	v_{max} [mm/s]	0.01	0.1	1	10	100
–50	h [μm]	9.70	6.67	4.13	2.47	1.78
	a [μm]	98.47	81.68	64.28	49.65	42.19
	$\mu_{hysteresis}$	0.0180	0.0160	0,0090	0,0050	0.0040
25	h [μm]	27.03	25.94	24.12	23.06	19.93
	a [μm]	164.40	161.07	155.29	151.86	141.18
	$\mu_{hysteresis}$	0.0051	0.0073	0.0108	0.0118	0.0113
150	h [μm]	26.16	26.16	26.04	25.61	24.87
	a [μm]	161.75	161.74	161.37	160.04	157.69
	$\mu_{hysteresis}$	0.0001	0.0006	0.0029	0.0041	0.0073

Table 2. Values of the penetration depth (h), radius of the contact area (a) and the hysteretic coefficient of friction ($\mu_{hysteresis}$) in case of 40-term Maxwell-model fitted to the measured storage modulus master curve

Temperature [°C]	v_{max} [mm/s]	0.01	0.1	1	10	100
–50	h [μm]	6.70	5.38	5.11	3.55	4.20
	a [μm]	83.65	73.32	71.45	59.60	64.71
	$\mu_{hysteresis}$	0.0120	0.0080	0.0050	0.0020	0.0007
25	h [μm]	25.94	25.60	24.59	22.78	20.65
	a [μm]	161.04	159.85	156.82	150.93	143.71
	$\mu_{hysteresis}$	0.0041	0.0078	0.0087	0.0106	0.0111
150	h [μm]	25.90	25.90	25.88	25.56	24.74
	a [μm]	160.94	160.94	160.89	159.86	157.30
	$\mu_{hysteresis}$	0.0004	0.0010	0.0031	0.0079	0.0088

Table 3. Values of the penetration depth (h), radius of the contact area (a) and the hysteretic coefficient of friction ($\mu_{hysteresis}$) in case of 40-term Maxwell-model fitted to the measured loss factor master curve

Temperature [°C]	v_{max} [mm/s]	0.01	0.1	1	10	100
–50	h [µm]	9.74	6.62	4.02	2.54	1.82
	a [µm]	98.68	81.35	63.38	50.40	42.72
	$\mu_{hysteresis}$	0.0210	0.0180	0.0070	0.0030	0.0008
25	h [µm]	42.51	36.28	30.79	25.79	21.61
	a [µm]	206.18	190.48	175.48	160.60	147.02
	$\mu_{hysteresis}$	0.0203	0.0177	0.0184	0.0176	0.0173
150	h [µm]	57.22	55.37	49.44	42.51	36.28
	a [µm]	239.22	235.32	222.34	206.18	190.48
	$\mu_{hysteresis}$	0.0208	0.0237	0.0279	0.0212	0.0177

7). The calculated COFs can be considered as acceptably accurate. In this case, any subsequent modification of the Maxwell-parameters will impair the accuracy of numerical results (see the results at –50°C in Table 3). In this case, less accurate results are yielded as a consequence of the less accurate modelling of the measured storage modulus. In case of the 15-term material model, the highest hysteresis can be observed at –50°C at the first two speeds, in spite of a small penetration depth, as a result of a high loss factor. At 25 and 150°C, hysteresis increases as the speed increases, as suggested by the rising loss factor curves (Figure 6). In case of the 40-term Maxwell-model fitted to the storage modulus, the highest hysteresis can be calculated at –50°C at the lowest speed (Table 2), due to the high loss factor. In case of the other speeds, hysteresis is the highest at 25°C, increasing as the speed increases. In case of the 40-term Maxwell-model fitted to the loss factor (see Table 3) the highest hysteresis can be observed at 150°C at each speed, due to a low elastic modulus and a significant loss factor. The absolutely highest hysteresis was calculated at 1 mm/s. As shown in Figure 7, the Maxwell-model fitted to the storage modulus can only model developments in the measured loss factor very inaccurately within the frequency range indicated by grey colour. Accordingly, the results figuring in the second and third lines of Table 2 can only be considered as rough lower estimates. To the contrary, the 40-term Maxwell-model fitted to the loss factor and shown in Figure 8 and 9 models the loss factor accurately but underestimates the measured storage modulus. In case of increasing frequencies, the degree of underestimation gradually decreases. As a result of the underestimated elastic modulus, the results in Table 3 for 25 and 150°C can be considered as upper estimates as regards the COF. Based on Figure 8 and 9, it can be stated that the COF result in Table 3, pertaining to 25°C and v_{max} = 100 mm/s can be considered as acceptably accurate. In this case, the COF value is more than 50% higher than the COF value in the last column of the second row in Table 2, determined using the 40-term Maxwell-model fitted to the storage modulus.

3.2. Comparison of the FE results to a simple analytical model

The correlation to estimate the hysteretic coefficient of friction presented in [13] was used for interpreting FE results; this way changes in the coefficient of friction can be analyzed in quantitative terms. Greenwood and Tabor demonstrated that in case of a rigid ball sliding on rubber, the hysteretic coefficient of friction can be estimated by Equations (8) and (9):

$$\mu = \frac{9\cdot\pi}{64}\cdot\frac{1-\nu^2}{\hat{E}}\cdot p_{av}\cdot\alpha \tag{8}$$

$$\frac{1}{\hat{E}} = \frac{1-\nu_1^2}{E_1} + \frac{1-\nu_2^2}{E_2} \tag{9}$$

where ν is the Poisson ratio; $\hat{E}$ is the equivalent elastic modulus of the contacting bodies defined by the Equation (9); p_{av} is the average contact pressure; and α is the number characterizing the energy dissipation resulting from hysteresis in the rubber, specifying what proportion of the work required to deform the rubber in front of the sliding ball is dissipated as a consequence of hysteresis. The authors did not publish further correlations to determine the value of α. The average contact pressure can be calculated by Equation (10):

$$p_{av} = \frac{F_n}{a^2 \cdot \pi} \tag{10}$$

where F_n is the force on the ball, and a is the radius of the contact area. To determine $\hat{E}$, the complex Young modulus was determined from the storage modulus and loss factor master curves for each given frequency according to Equation (11) and it was substituted for $(1 - \nu^2)/E$:

$$E^* = \frac{E'}{\cos\delta} \tag{11}$$

If the left side of Equation (8) is replaced by the coefficients of friction calculated by the FE method ($\mu_{hysteresis}$), then parameter α in the Greenwood-Tabor model can be determined in the function of sliding speed and temperature. Figures 10 and 11 show the frequency dependence of factor α and of the loss factor of the rubber with reference to 40-term material models and various temperatures. It can be observed in terms of tendency that the values of α properly follow the changes in tanδ at each temperature, in the function of frequency. Greenwood and Tabor [13] made an attempt to determine α from cyclic tests having strain rate comparable to those occurring in sliding experiments. In their interpretation, the energy loss due to hysteresis was defined as α times the total elastic energy of deformation. We assumed that α is influenced by the phase shift between stress and strain as, in case of cyclic tension/compression, the hysteretic loss per cycle and per unit volume is influenced by sinδ. Since the tendency of sinδ and tanδ, within the loss factor range measured by DMTA, is similar we

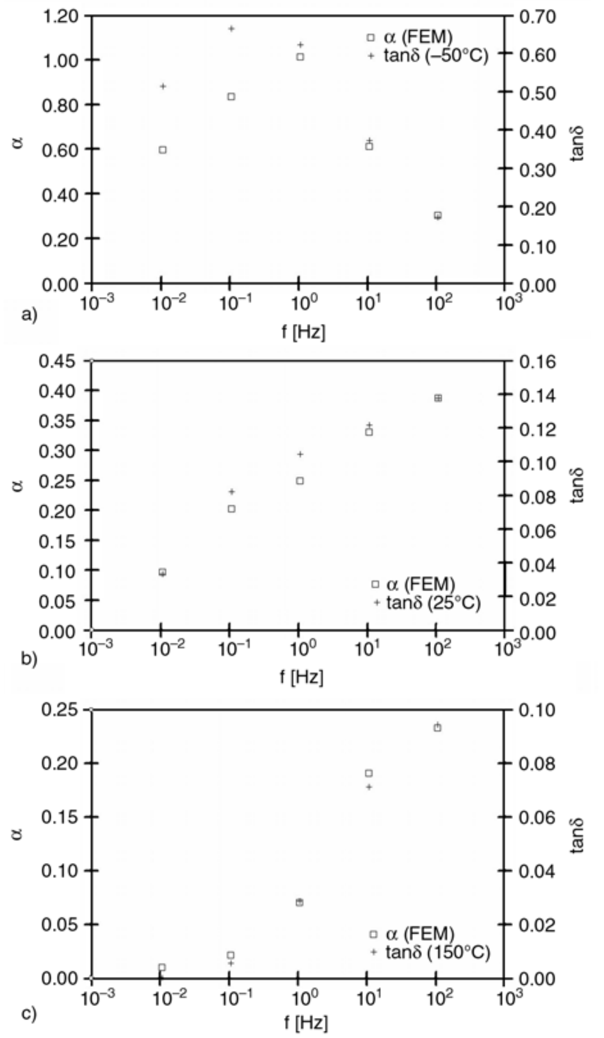

Figure 10. Variation of α and tanδ in function of frequency (40-term Maxwell-model fitted to the storage modulus master curve): a) T = –50°C, b) T = 25°C, c) T = 150°C

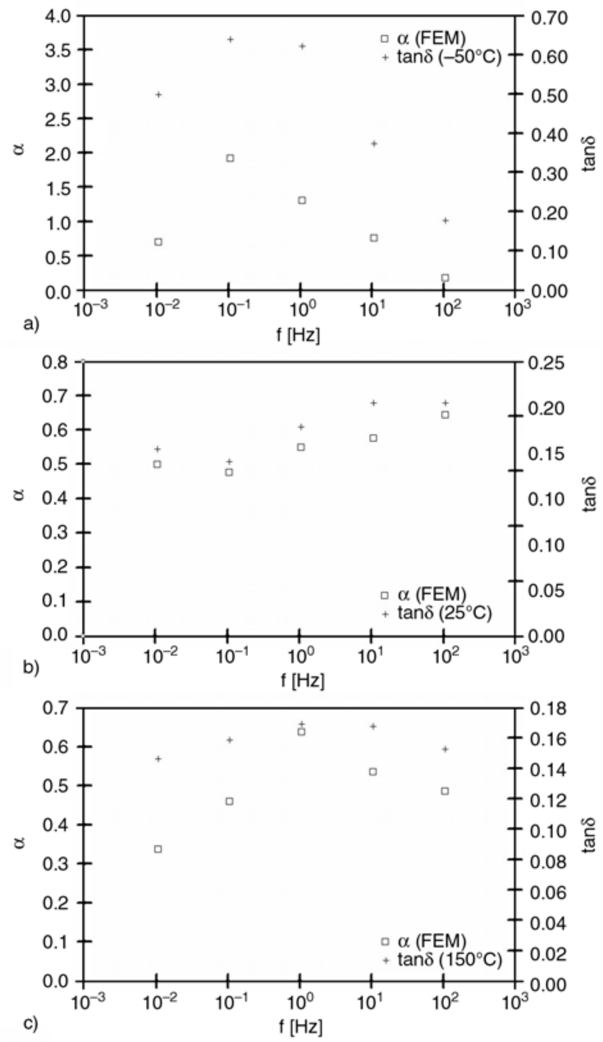

Figure 11. Variation of α and tanδ in function of frequency (40-term Maxwell-model fitted to the loss factor master curve): a) T = –50°C, b) T = 25°C, c) T = 150°C

used tanδ for comparison with α. Based on these, Equation (8) can be used for a qualitative description of changes in the hysteretic coefficient of friction if α is substituted by tanδ.

$$\mu \approx \frac{9\cdot\pi}{64}\cdot\frac{1-\mu^2}{\hat{E}}\cdot p_{av}\cdot\tan\delta \qquad (12)$$

Figures 12 and 13 compare the coefficients of friction calculated by FE method and by Equation (12). As expected, COFs calculated by Equation (12), in every case are smaller than the ones predicted by the numerical method. In respect of the tendencies, the values calculated by the two different methods are in a good agreement.

4. Conclusions

1. An FE model has been developed for the prediction of hysteretic friction force in case of a reciprocating steel ball sliding on a rubber plate.
2. It can be concluded that because of the high oscillation in the tanδ curve the 15-term generalized Maxwell-model fitted to the whole frequency range is not able to characterize the time- and temperature-dependent behaviour of the rubber. To avoid this oscillation Maxwell-models with 40-term were constructed.
3. It can also be concluded that, within a certain frequency range, even the 40-term Maxwell-model fitted to the storage modulus master curve under-

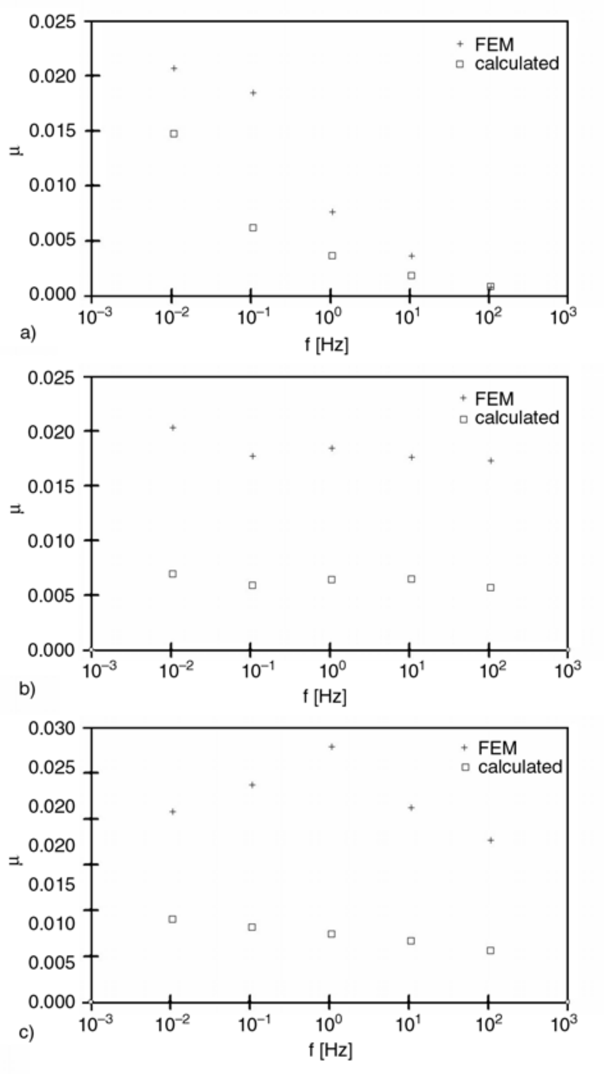

Figure 12. Comparison of the coefficients of friction predicted by FEM and Equation (8) (40-term Maxwell-model fitted to the storage modulus master curve): a) *T* = –50°C, b) *T* = 25°C, c) *T* = 150°C

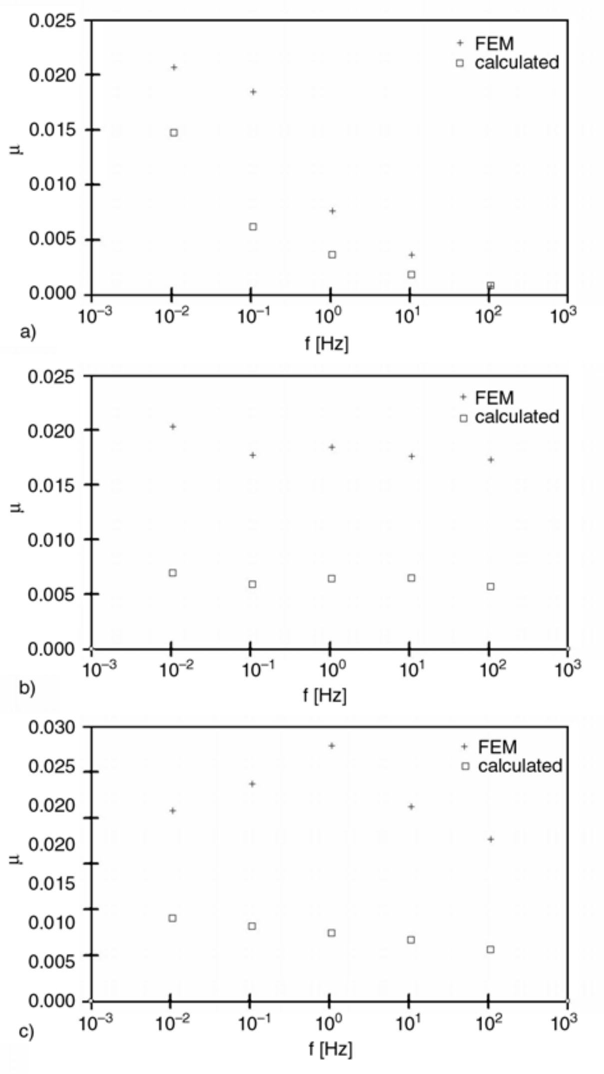

Figure 13. Comparison of the coefficients of friction predicted by FEM and Equation (8) (40-term Maxwell-model fitted to the loss factor master curve): a) *T* = –50°C, b) *T* = 25°C, c) *T* = 150°C

estimates the hysteretic friction because the loss factor provided by the material model is about the half of the one measured. The accuracy of the numerical prediction depends not only on the excitation frequency but also on the operational temperature as it shifts the master curves horizontally according to the time-temperature superposition. This conclusion is extremely important because the viscoelastic material model parameters usually are determined from a fit to the storage modulus master curve in the literature.

4. In order to predict the hysteretic friction more accurately or to provide below and/or upper limit for the hysteretic coefficient of friction one has to construct a material model that describes both the storage modulus and the loss factor master curves measured with sufficient accuracy. By using the proposed technique i.e. fitting the material model to the measured loss factor master curve the accuracy of the numerical prediction can be improved significantly in several cases.
5. From fit to the numerical predictions the open parameter of the Greenwood-Tabor model (α) has been determined as a function of frequency and temperature. Its value ranges from 0.01 to 2. Without specifying parameter α properly the Greenwood-Tabor model can not be used to predict hysteretic friction generated by a sliding ball.

Acknowledgements

The authors wish to acknowledge the support of the Partners of the Kristal project and the European Commission for their support in the integrated project 'Knowledge-based Radical Innovation Surfacing for Tribology and Advanced Lubrication' (EU Project Reference NMP3-CT-2005-515837).

References

[1] Grosch K. A.: The relation between the friction and viscoelastic properties of rubber. Proceedings of the Royal Society of London, Series A, **274**, 21–39 (1963).
DOI: 10.1098/rspa.1963.0112

[2] Persson B. N. J.: Theory of rubber friction and contact mechanics. The Journal of Chemical Physics, **115**, 3840–3861 (2001).
DOI: 10.1063/1.1388626

[3] Persson B. N. J., Albohr O., Creton C., Peveri V.: Contact area between a viscoelastic solid and a hard, randomly rough, substrate. The Journal of Chemical Physics, **120**, 8779–8793 (2004).
DOI: 10.1063/1.1697376

[4] Klüppel M., Heinrich G.: Rubber friction on self-affine road tracks. Rubber Chemistry and Technology, **73**, 779–797 (2000).

[5] Bui Q. V., Ponthot J. P.: Estimation of rubber sliding friction from asperity interaction modelling. Wear, **252**, 150–60 (2002).
DOI: 10.1016/S0043-1648(01)00864-X

[6] Soós E., Goda T.: Numerical analysis of sliding friction behaviour of rubber. Materials Science Forum, **537–538**, 615–621 (2007).
DOI: 10.4028/www.scientific.net/MSF.537-538.615

[7] Nettingsmeier J., Wriggers P.: Frictional contact of elastomer materials on rough rigid surface. PAMM, **4**, 360–361 (2004).
DOI: 10.1002/pamm.200410161

[8] Pálfi L., Goda T., Váradi K., Garbayo E., Bielsa J. M., Jiménez M. A.: FE prediction of hysteretic component of rubber friction. Meccanica, in press (2009).

[9] Felhős D., Xu D., Schlarb A. K., Váradi K., Goda T.: Viscoelastic characterization of an EPDM rubber and finite element simulation of its dry rolling friction. Express Polymer Letters, **2**, 157–164 (2008).
DOI: 10.3144/expresspolymlett.2008.21

[10] Pálfi L., Fernández B., Váradi K.: FE modelling of oscillating sliding friction between a steel ball and an EPDM plate. in 'Proceedings of Sixth Conference on Mechanical Engineering. Budapest, Hungary' on CD p. 11 (2008).

[11] MSC. Marc user manual, Version 2007R1: MSC. Software corporation, Santa Ana (2007).

[12] Herdy M.: Introductory theory manual ViscoData and ViscoShift. IBH-Ingenierbüro, Grafschaft (2003).

[13] Greenwood J. A., Tabor D.: The friction of hard sliders on lubricated rubber: The importance of deformation losses. Proceedings of the Physical Society, **71**, 989–1001 (1958).
DOI: 10.1088/0370-1328/71/6/312

eXPRESS Polymer Letters Vol.3, No.11 (2009) 724–732
Available online at www.expresspolymlett.com
DOI: 10.3144/expresspolymlett.2009.90

Effects of bromination on the viscoelastic response of vinyl ester nanocomposites

A. Almagableh[1*], *P. R. Mantena*[2], *A. Alostaz*[3], *W. Liu*[4], *L. T. Drzal*[4]

[1]University of Mississippi, PO. Box 3967, MS 38677, USA
[2]University of Mississippi, 201 D Carrier Hall, MS 38677, USA
[3]University of Mississippi, 202 Carrier Hall, MS 38677, USA
[4]Composite Materials and Structures Center, Michigan State University, 2100 Engineering Bldg, East Lansing, MI 48824, USA

Received 25 May 2009; accepted in revised form 1 September 2009

Abstract. Fire, smoke and toxicity are of significant concern for composite materials used in marine applications. Bromination of vinyl ester resin imparts fire retardancy as manifested by a reduction in the amount of smoke, carbon monoxide, and corrosive combustion products. In this research, the viscoelastic properties, modulus (stiffness) and damping (energy dissipation), of 1.25 and 2.5 wt. percent nanoclay and exfoliated graphite nanoplatelet (xGnP) reinforced non-brominated and brominated vinyl ester have been studied over a range of temperature and frequency. Effects of frequency on the viscoelastic behavior were investigated using a Dynamic Mechanical Analyzer (DMA) by sweeping the frequency over three decades: 0.01, 0.1, 1 and 10 Hz, and temperature range from 30–150°C at a step rate of 4°C per minute. Master curves were generated by time-temperature superposing the experimental data at a reference temperature. The nano reinforced composites showed a drop in initial storage modulus with bromination. Nanocomposites with 1.25 and 2.5 wt. percent graphite had the highest storage modulus among brominated specimens. Bromination was also found to significantly increase the glass transition temperature (T_g) and damping for all nanocomposites. Among the brominated specimens, 1.25 wt. percent graphite platelet reinforced vinyl ester exhibited the best viscoelastic response with high damping and glass transition temperature, along with superior storage modulus over a longer time period.

Keywords: *nanocomposites, viscoelastic properties, bromination*

1. Introduction

Thermoset vinyl ester matrices are becoming increasingly important in industrial applications due to their enhanced mechanical properties. They exhibit characteristics similar to epoxy resins, as well as unsaturated polyester resins. Advantages include high tensile strength and stiffness, low cost, process versatility and good chemical resistance. However, vinyl ester still has some challenges like poor resistance to crack propagation, brittleness and large shrinkage that occurs during polymerization. Therefore, introducing good interfacial bonding between nanofillers and the resin is often used to alleviate volume shrinkage, void formation and improving surface dispersion along with toughness. Methods of incorporating nanoparticles into polymer matrices could be *ex-situ*, like dispersion of the synthesized nanoparticles into resin solution, or *in-situ* monomer polymerization process in the presence of the nanoparticles [1]. The interaction between the nanoparticles and matrix for the *ex-situ* fabricated composites are normally van der waals

---

[*] Corresponding author, e-mail: amalmag1@olemiss.edu

forces, steric interaction. However, the *in-situ* synthesis methods may create strong chemical bonding within the composite.

Optical and mechanical properties of vinyl ester polymer reinforced with ZnO nanoparticles, functionalized with a bi-functional coupling agent methacryloxypropyl-trimethoxysilane (MPS) were investigated by Guo *et al.* [2]. The existence of MPS at the interface between the matrix and particles results in improved interfacial interaction which in turn improves UV shielding, modulus and strength significantly.

The physical properties of vinyl ester reinforced with unmodified CuO nanoparticles and those functionalized with a bi-functional coupling agent methacryloxypropyl-trimethoxysilane (MPS) were studied by Guo *et al.* [3]. Increase in both thermal stability and mechanical properties were attributed to good nanoparticles dispersion at the interface and the resulting chemical bonding between the functionalized nanoparticles and the matrix.

Vinyl ester thermosetting nanocomposites reinforced with iron oxide nanoparticles were prepared and characterized by Guo *et al.* [4]. Iron oxide nanoparticles functionalized with a bi-functional coupling agent was observed to increase the adhesion and dispersion of the nano filler into the matrix resulting in increased thermal stability, lower curing temperature and improved mechanical properties. The nanocomposites became also magnetically stronger and were independent of particles functionalization.

Schroeder *et al.* [5] analyzed morphologically thermoset materials obtained from styrene/vinyl ester resins of different molecular weights modified with polymethyl methacrylate (PMMA). It was found that different morphologies including dispersion of thermoplastic rich particles in a thermoset resin, continuity of network structure were highly dependent on molecular weight of vinyl ester, curing temperature and concentration of the PMMA additives. The addition of the thermoplastic PMMA increased the fracture resistance without significantly affecting both volume shrinkage reduction and the thermal-mechanical properties of the modified thermosets.

Recent interest in the use of organic-matrix composite materials in US Navy submarines and ships has generated the requirement for significant improvement in the flammability performance of these materials including reduction in the amount of smoke, carbon monoxide, and corrosive combustion products. New fire retardant approaches for organic-matrix composite materials are needed to address the smoke issues and to further reduce the flammability of these composites. Focus of our research is on developing stronger, safer and more cost-effective structures for the new generation naval ships; especially nanoparticle reinforced glass/carbon polymeric based composites and structural foams for blast/shock/impact mitigation. Fire, smoke and toxicity are of significant concern in ship structures. The US Navy is currently using brominated vinyl ester matrix resin with glass reinforcement for composite applications in topside surface ship structures [6]. This matrix resin was selected due to its good corrosion resistance and toughness. Bromine is an effective flame retardant, especially when combined with antimony oxide. Bromination of vinyl ester resin imparts fire retardancy as manifested by flame spread and lower heat release rates. However, this fire-retardant system functions primarily in the gas phase causing incomplete combustion. As such, brominated resins produce dense smoke, an increase in the yield of carbon monoxide, and hydrogen bromide.

The work reported here is an extension of previous work [7] on the viscoelastic behavior of non-brominated vinyl ester nanocomposites. DMA measurements are usually carried out under constant displacement amplitude in a fixed-frequency deformation mode, in which the mechanical properties are function of temperature only. Other measurements that provide more information may include frequency sweep with temperature steps, to which time-temperature superposition (TTS) applied to predict the long-term time dependent properties of the material [8]. An attempt has been made to experimentally characterize the dynamic storage modulus (E') and damping of brominated and non-brominated vinyl ester reinforced with 1.25 and 2.5 wt. percent nano-clay and exfoliated graphite nanoplatelets (xGnP) as a function of temperature and frequencies. Dynamic mechanical testing has been used to perform multi-frequency (accelerated temperature measurements) and theoretical time-temperature superposition treatment of the data. Effects of bromination on the viscoelastic response of these vinyl ester nanocomposites are discussed.

2. Theory

The time-temperature superposition principle is based on the fact that processes involved in molecular motion occur at larger rates at elevated temperatures. The change in property which occurs relatively quickly at higher temperatures can be made to appear as if they occurred at longer times or lower frequencies simply by shifting the data with respect to time (1/frequency) [8]. By shifting the data with respect to frequency to a reference curve, a master curve is generated, which covers time (frequencies) outside the accessible range.

The shifting mechanism used to shift a set of data upon a reference curve follows WLF [8] model. This model assumes that the fractional free volume increases linearly with respect to temperature in the transition region, and when the free volume increases, its viscosity decreases. In this model, the degree of shifting was calculated according to Equation (1);

$$\log a_T = \frac{-C_1(T-T_0)}{C_2+(T-T_0)} \qquad (1)$$

For both resin systems (with and without bromination), C_1 and C_2 were found to be around 103.9 and 399 K, respectively. Relationship between the shifting factor (a_T) versus T is plotted in Figure 1 for pure and brominated vinyl ester.

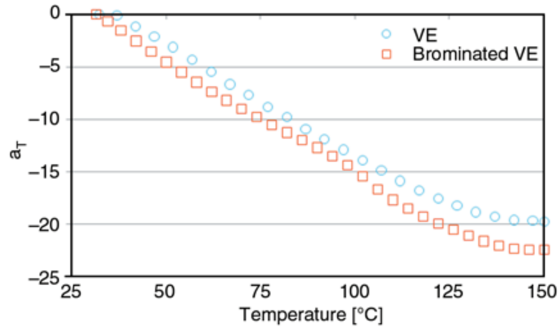

Figure 1. Relationship between shifting factor (a_T) and temperature for pure and brominated vinyl ester based on the WLF model

3. Experimental

3.1. DMA setup

Dynamic measurements were carried out using the TA Instrument model Q800 DMA on prismatic specimens deformed in a single-cantilever clamping mode, with a span length of 17.5 mm. Stress and strain with the single-cantilever clamp used in model Q800 DMA are calculated with Equations (2) and (3), respectively [8], assuming linear viscoelastic behavior.

$$\sigma_x = \frac{6PL}{wt^2} \qquad (2)$$

$$\varepsilon_x = \frac{3\delta t F_c}{L^2\left[1+\frac{12}{5}(1+\upsilon)\left(\frac{t}{L}\right)^2\right]} \qquad (3)$$

where L – clamp span length
t – sample thickness
w – width of the specimen
ν – Poisson's ratio
F_c – clamping correction factor
σ_x – stress
ε_x – strain
P – applied force
δ – amplitude of deformation

3.2. Test description

The 1.25 and 2.5 wt. percent nanocaly and xGnP reinforced non-brominated and brominated vinyl ester nanocomposites were characterized by performing a multi-frequency isothermal mode, in which the sample is equilibrated at different temperatures and subjected to a series of frequencies. Specimens with dimensions of 35×10×1.6 mm were subjected to frequencies of: 0.01, 0.1, 1 and 10 Hz with a temperature step rate of 4°C per minute starting from 30°C (RT) to 150°C. A very small displacement amplitude (25 μm was applied since the analysis assumes linear viscoelastic characterization, and two specimens were tested from each configuration. The raw data was then fed to the Rheology data analysis software to generate the master curves.

3.3. Materials and sample preparations

The polymeric matrix used was a vinyl ester resin (manufactured and supplied by Ashland specialty chemical, Division of Ashland INC (Columbus, OH)). DERAKANE 411-350-(non-brominated) is a mixture of 45 wt.% styrene and 55 wt.% vinyl ester. Styrene allows the chain extension because of its single unsaturated carbon-carbon double bond, while the vinyl ester resin with two reactive vinyl

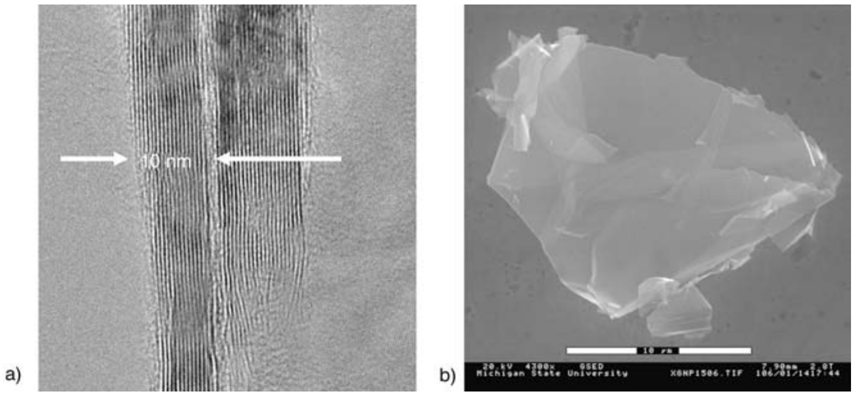

Figure 2. Morphology of xGnP using (a) edge view (TEM), and (b) Lateral view (SEM)

end groups enables the crosslinking for network. DERAKANE 510A-40 (brominated) vinyl ester resin is a brominated bisphenol-A based vinyl ester consisting of 38 wt.% styrene, and modified to produce the maximum degree of fire retardancy combined with enhanced chemical resistance and toughness. These additives are Butanone peroxide, N,N-Dimethylaniline, Cobalt Naphthenate, and 2-4-Pentanedione, all supplied from Sigma Aldrich (St. Louis, Mo).

Exfoliated graphite nanoplatelets (xGnP) were produced according to the method described in [9]. The nanoclay was Cloisite 30B from Southern Clay Products, Inc (Gonzales, TX). Figures 2a and 2b show a morphology using TEM and SEM for both edge and lateral views of xGnP inside a polymer. These xGnP nanocomposites have exfoliated and dispersed graphite platelets with 1 nm thickness and several hundred nanometers widths. Distance between layers is in the range of 10~30 Å and size of the layered graphite extends from several hundred nanometers to several microns.

The samples were prepared by dispersing about 3000 g of epoxy vinyl ester resin solution with different percentages of nanoclay or nanographite in a 1 gal container for 4 hours, followed by 4 passes through a flow cell connected to a 100 W sonicator. 1% Butanone peroxide, 0.2% of 2-4 Pentanedione, 0.1% N,N-Dimethylaniline, and 0.2% Cobalt Naphthenate were added to the mixed vinyl ester resin solution in order and mixed for 10 min. The above mixed resin solution was mixed for 2 min with FlackTek speed mixer at 3000 RPM. The well-mixed vinyl ester resin solution with nanoclay or nanographite was poured into a 13×13×0.4” mold, let stand for 30 minutes at room temperature and then was post cured at 80°C for 3 hours. Prismatic samples with nominal dimension of 35×10×1.6 mm size were prepared from these plates and tested in a DMA using the single-cantilever clamp fixture.

4. Results and discussion

4.1. Densities

As shown in Figure 3, the densities of brominated vinyl ester nanocomposites are greater than that of the non-brominated samples. It should be noted that bromine is a heavy atom and there are four bromine atoms bonded in one molecule, which results in density being higher for brominated specimens. Specific gravity of 510A-40 brominated vinyl ester is about 1.23 while that of the non-brominated version 411-350 is 1.046.

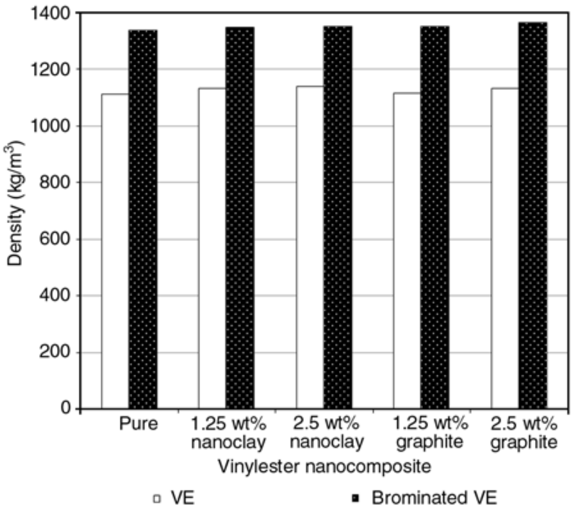

Figure 3. Densites of non-brominated (411-350) and brominated (510A-40) vinyl ester nanocomposites

4.2. Modulus

The storage modulus versus temperature curve provides valuable information about the stiffness of a material as a function of temperature, and it is sensitive to structural changes such as molecular weight, fiber-matrix bonding and degree of crosslinking density. Crosslink density, typically given as the average molecular weight between crosslinks (M_c), is an important factor governing the physical properties of cured thermoset resins. Moreover, it can be changed by adjusting the styrene content in the resins, molecular weight of vinyl ester oligomers, altering the state of conversion, and control of the cure conditions [10]. Crosslinking densities of the two resin systems (non-brominated and brominated) resulting from different styrene contents were calculated [10] as 1116 and 597 mol/m^3, respectively, based on Equation (4):

$$V = \frac{G_0^n}{RT} \tag{4}$$

where V – crosslinking density
R – gas constant
G_0^n – plateau modulus from master curve of the shear modulus versus frequency.

Calculation of crosslinking density for nanocomposites using this equation is invalid, because contribution of nanoparticles in the crosslinking mechanism is unknown.

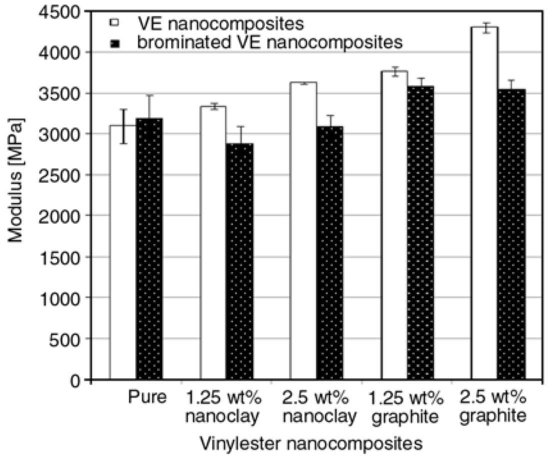

Figure 4. Initial storage modulus for non-brominated and brominated nanocompsoites at 1 Hz frequency

Higher initial storage modulus in fiber reinforced composite materials are in general attributed to good fiber/matrix bonding (cross linking), or higher initial molecular weight [11]. Figure 4 shows initial storage modulus (30°C) for vinyl ester nanocomposites, with and without bromination. Initial modulus was observed to increase with addition of nanoparticles in the non-brominated system. On the other hand, bromination resulted in a reduction of the initial storage modulus with addition of nanoparticles. Among the brominated specimens, gain in glassy (initial) modulus was observed with xGnP reinforcement, and a loss in glassy modulus was associated with the addition of nanoclay particles. Loss in storage moduli with the brominated nanoclay composites could be due to weak interfacial bonding between the nanoclay particles and brominated resin. However, the 1.25 wt.% xGnP appears to be bonding better with the brominated resin resulting in higher storage modulus compared to pure brominated vinyl ester.

Figures 5–7 show the storage modulus (E') evolution with temperature for some of the vinyl ester nanocomposites, with and without bromination. Bromination effect modifies the dynamic mechanical behavior for VE and its nanocomposites. Drop

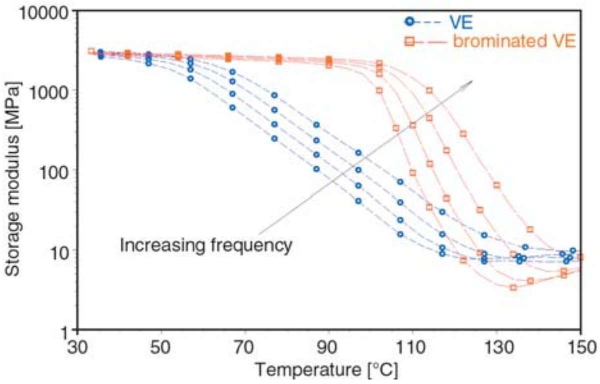

Figure 5. Storage modulus for pure vinyl ester with and without bromination

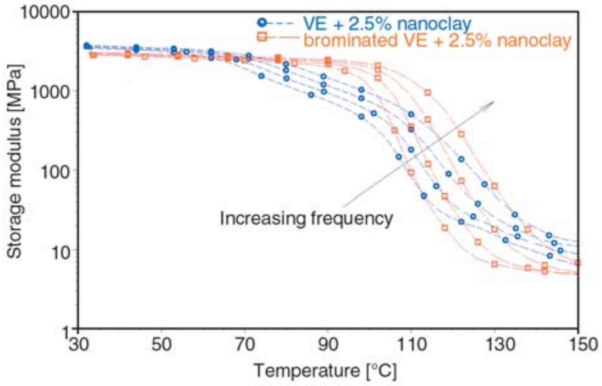

Figure 6. Storage modulus for 2.5 wt. percent nanoclay reinforced vinyl ester with and without bromination

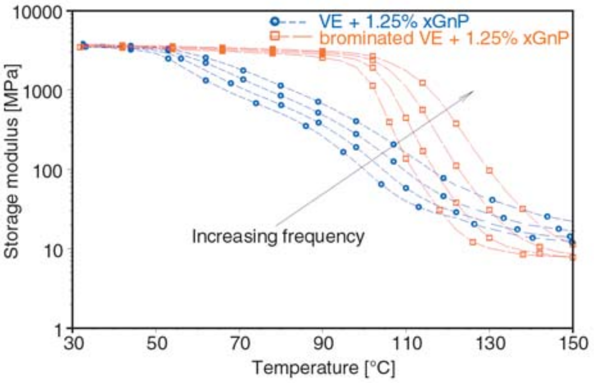

Figure 7. Storage modulus for 1.25 wt. percent xGnP reinforced vinyl ester with and without bromination

in modulus in the transition region is shifted to higher temperature. It is interesting to note that no major variation appears in the value of the rubbery modulus in both systems (brominated and non-brominated) with the addition of nanoparticles. This indicates that the crosslinking density of both networks has not been significantly affected with the addition of nanoparticles.

4.3. Damping

Tanδ, defined as the ratio of loss modulus to storage modulus, is a measure of the inherent material damping. Peak of tanδ is the region over which the material experiences a transition from glassy to a leathery behavior, associated with the onset of short range molecular segments motion, of which all are initially fixed. Bromination in general resulted in greater value of tanδ peak for all the nano reinforcements including pure vinyl ester (300% increase) suggesting that more material is involved in the relaxation (Figures 8–10). Two relaxations were observed for non-brominated vinyl ester, one at around 60°C and another between 110–120°C, which corresponds to the transition of St-resin rich phase at higher temperature. Varying the nanoclay concentration from 0 to 2.5 wt. percent produced a significant increment in the height of the corresponding loss factor peak (Figure not shown). However, significant drop of tanδ peak was associated with the addition of 2.5 wt.% xGnP to brominated resin. The greater amount of xGnP added to the brominated resin, more brittle material behavior was observed.

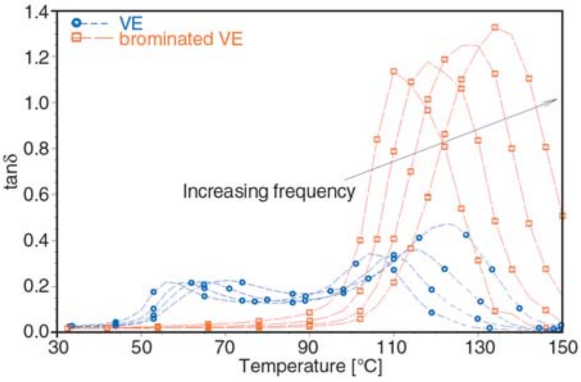

Figure 8. Tanδ curves for pure vinyl ester, with and without bromination

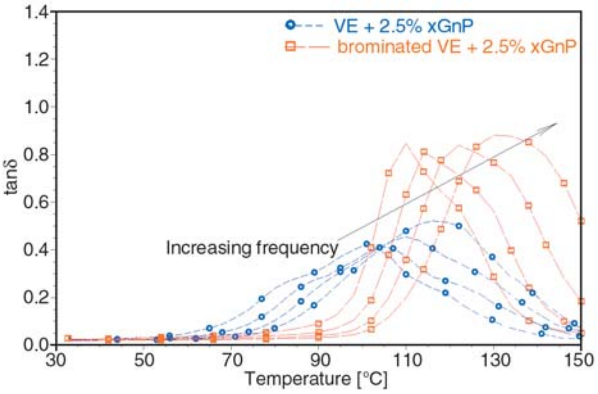

Figure 9. Tanδ curves for vinyl ester reinforced with 2.5 wt.% xGnP, with and without bromination

Area under tanδ curve (with units of °C) over the temperature range (30–150°C) was also calculated, as it is another good indicator of the total energy absorbed by the material [12]. The higher the area under tanδ curve, the greater the degree of molecular rearrangement, which enables the material to better absorb and dissipate energy. Brominated nanocomposites in general exhibited higher area under tanδ curves compared to the non-brominated

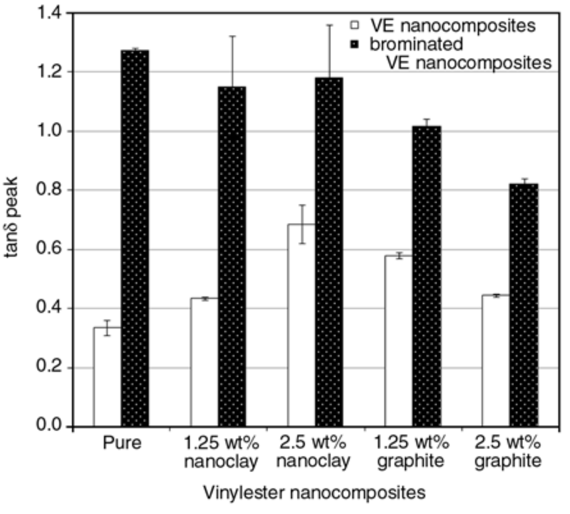

Figure 10. Tanδ peak for brominated and non-brominated vinyl ester nanocomposites at 1 Hz frequency

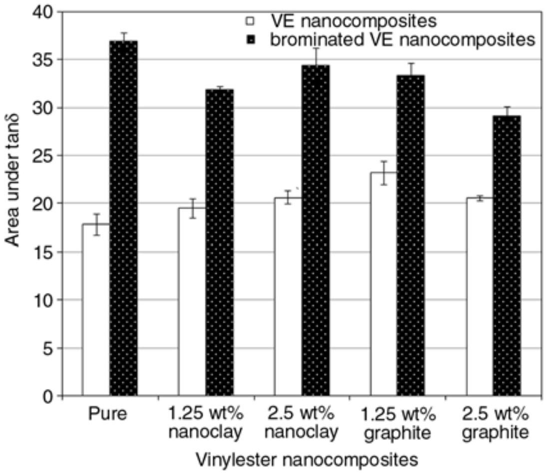

Figure 11. Area under tanδ curves for brominated and non-brominated vinyl ester nanocomposites at 1 Hz frequency

samples (Figure 11). From Figure 10, the higher tanδ peak value observed with the addition of 2.5 wt. percent nanoclay compared to 2.5 wt. percent graphite for brominated specimens, indicates greater molecular mobility in nanoclay brominated composites. Besides, the greatest loss in storage modulus along with the superior tanδ peak associated with the addition of nanoclay particles to brominated resin indicates that this reinforcement may be adversely affecting the interfacial bonding. Consequently, graphite nanoplatelets appear to form better interfacial bonding with brominated resin than nanoclay reinforcements.

4.4. Glass transition temperature, T_g

Figure 12 shows the loss modulus curves for the pure and brominated vinyl ester, as a function of frequency. Brominaton system produced network with higher glass transition temperature (temperature corresponding to peak of loss modulus) than the non-brominated case. For example, T_g, for pure vinyl ester increased by about 80% with bromination. Glass transition temperature for the non-brominated vinyl ester nanocomposite system increased with increasing content of nanoparticles. Whereas in case of brominated vinyl ester nanocomposite system, it did not change with addition of nanoparticles. Furthermore, the glass transition temperature of the brominated samples for both pure resin and the nanocomposites was still higher than that of the non-brominated samples.

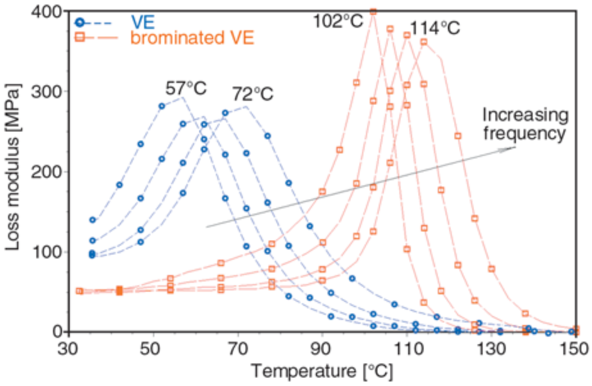

Figure 12. Loss modulus for pure vinyl ester, with and without bromination, as a function of frequency

The significant increase in, T_g, achieved with bromination is probably due to higher initial density (molecular weight). As molecular weight increases with bromination, the glass transition region is displaced to longer time or temperature, because chain movement is expected to suppress when molecular entanglement is increased [13].

4.5. Time-temperature superposition

Since the glass transition temperature for nanocomposites with and without bromination is found to be varying, for this work a reference temperature of 50°C was chosen to generate master curves for the storage modulus. To perform this, data from higher temperature experiments in the lower portion of the plot are shifted to the left (lower frequencies) and curves corresponding to the temperatures lower than 50°C are shifted to the right [8]. Figure 13 shows the generated master curves of storage modulus over an extended period of time. From Figure 13a, the brominated vinyl ester is observed to maintain its rigidity (at 50°C) with an average dynamic storage modulus of (2.5 GPa) over a period of 10^{10} secs (321.5 years), where as the non-brominated vinyl ester starts to loose it's stiffness gradually just after 10^3 secs (17 minutes). This is a significant improvement on the long term behavior of vinyl ester with bromination. Similarly, the brominated 1.25 wt. percent xGnP reinforced specimens exhibit superior average modulus of 2.7 GPa over 321.5 years (Figure 13b). In contrast, all the specimens with 2.5 wt. percent nanoreinforcement, both with and without bromination, show a stable dynamic response with an average storage modulus of 2.5 GPa (Figure 13c) for the first 10^8 sec (3.2 years) only.

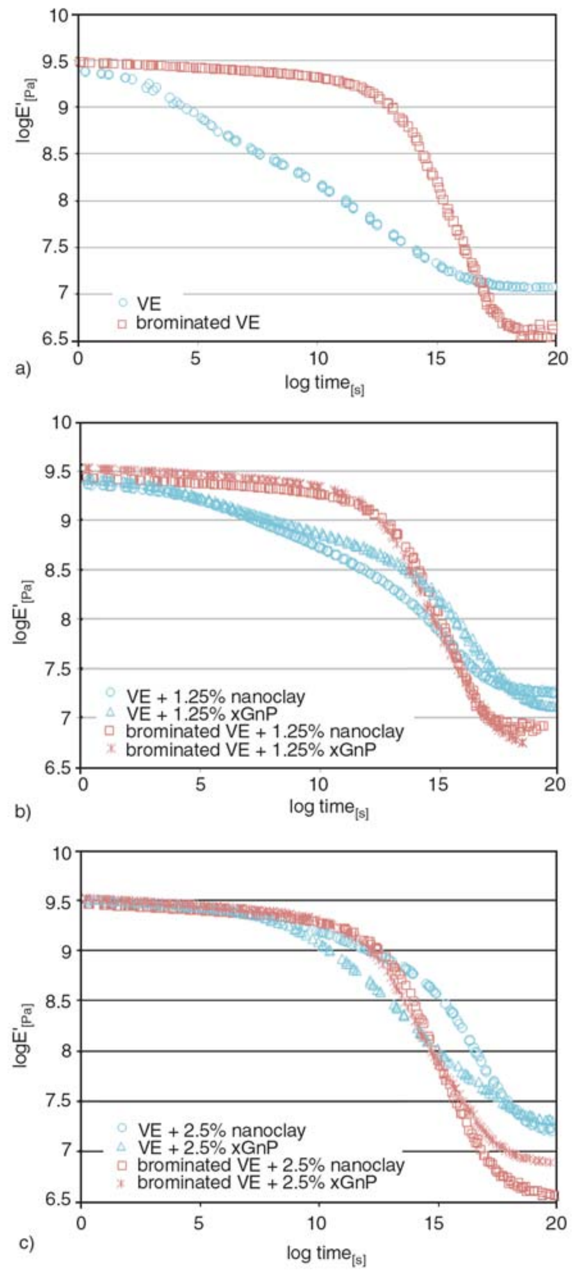

Figure 13. Master curves of storage modulus at a reference temperature of 50°C as a function of log time for a) pure vinyl ester, b) 1.25 wt. percent and c) 2.5 wt. percent nanoparticles

5. Conclusions

Bromination of vinyl ester resin imparts fire retardancy as manifested by a reduction in the amount of smoke, carbon monoxide, and corrosive combustion products. The effect of bromination on the viscoelastic behavior of Derakane 411-350 (non-brominated) vinyl ester reinforced with 1.25 and 2.5 wt. percent nanoclay and graphite nanoplatelets was investigated with a DMA. Frequency sweep across three decades: 0.01, 0.1, 1 and 10 Hz was performed over temperature range from 30 to 150°C at a step rate of 4°C/min. The time-temperature superposition principle was applied to create master curves of dynamic storage modulus at a reference temperature of 50°C.

Initial modulus was observed to increase with addition of nanoparticles in the non-brominated system. However, bromination resulted in a reduction of initial storage modulus with the addition of nanoparticles. Among the brominated specimens, gain in glassy (initial) modulus was observed with xGnP reinforcement, and a loss in glassy modulus was associated with the addition of nanoclay particles.

Both the pure vinyl ester and nanocomposites with bromination exhibited higher tanδ peak values and larger areas under the tanδ curves. From the storage modulus and damping results, it is surmised that graphite platelets appear to form better interfacial bonding with the brominated resin than the nanoclay reinforcements. Brominaton was also found to significantly increase the glass transition temperature for both pure vinyl ester (up to 80%) and the nanocomposites. The brominated vinyl ester reinforced with 1.25 wt. percent graphite platelets exhibited the best viscoelastic response with high damping and glass transition temperature, along with superior storage modulus over a longer time period.

Acknowledgements

The authors would like to acknowledge the support received from the Department of Civil Engineering at the University of Mississippi, and funding received under a subcontract from the Department of Homeland Security-sponsored Southeast Region Research Initiative (SERRI) at the Department of Energy's Oak Ridge National Laboratory. Support for this research by ONR Grant # N00014-07-1-1010, Office of Naval Research, Solid Mechanics Program (Dr. Yapa D.S. Rajapakse, Program Manager) is also acknowledged.

References

[1] Schroeder W. F., Borrajo J., Aranguren M. I.: Poly (methyl methacrylate)-modified vinylester thermosets: Morphology, volume shrinkage and mechanical properties. Journal of Applied Polymer Science, **106**, 4007–4017 (2007).
DOI: 10.1002/app.27006

[2] Guo Z., Wei S., Shedd B., Scaffaro R., Pereira T., Hahn H. T.: Particle surface engineering effect on the mechanical, optical and photoluminescent properties of ZnO/vinyl-ester resin nanocomposites. Materials Chemistry, **17**, 806–813 (2007).
DOI: 10.1039/b613286c

[3] Guo Z., Liang X., Scaffaro R., Pereira T., Hahn H. T.: CuO nanoparticle filled vinyl-ester resin nanocomposites: Fabrication, characterization and property analysis. Composites Science and Technology, **67**, 2036–2044 (2007).
DOI: 10.1016/j.compscitech.2006.11.017

[4] Guo Z., Lei K., Li Y., Wai Ng H., Prikhodko S., Hahn H. T.: Fabrication and characterization of iron oxide nanoparticles reinforced vinyl-ester resin nanocomposites. Composites Science and Technology, **68**, 1513–1520 (2008).
DOI: 10.1016/j.compscitech.2007.10.018

[5] Schroeder W. F., Auad M. L., Vico M. A. B., Borrajo J., Aranguren M. I.: Thermodynamic, morphological, mechanical and fracture properties of poly(methyl methacrylate)(PMMA) modified divinylester(DVE)/styrene(St) thermosets. Polymer, **46**, 2306–2319 (2005).
DOI: 10.1016/j.polymer.2005.01.019

[6] Sorathia U., Ness J., Blum M.: Fire safety of composites in the US Navy. Composites Part A: Applied Science and Manufacturing, **30**, 707–713 (1999).
DOI: 10.1016/S1359-835X(98)00112-2

[7] Almagableh A., Gupta S., Mantena P. R., Alostaz A.: Dynamic mechanical analysis of graphite platelet and nanoclay reinforced vinyl ester, and MWCNT reinforced nylon 6,6 nanocomposites. in 'Proceeding of SAMPE Fall Technical Conference, Memphis, USA', M034 p.19 (2008).

[8] TA Instruments.: Thermal analysis application brief, 144: Application of time-temperature superposition principles to DMA. TA Instruments, Newcastle (2004).

[9] Drzal L. T., Fukushima H.: Expanded graphite products produced therefrom. US Patent 7550529, USA (2009).

[10] Li H., Burts E., Bears K., Ji Q., Lesko J. J., Dillard D. A., Riffle J. S., Puckett P. M.: Network structure and properties of dimethacrylate-styrene matrix materials. Journal of Composite Materials, **34**, 1512–1528 (2000).
DOI: 10.1106/Q064-0U44-FWDJ-9LET

[11] Kuzak S. G., Shanmugam A.: Dynamic mechanical analysis of fiber-reinforced phenolic. Journal of Applied Polymer Science, **73**, 649–658 (1999).
DOI: 10.1002/(SICI)1097-4628(19990801)73:5<649::AID-APP5>3.0.CO;2-B

[12] Gupta S., Mantena P. R., Al-Ostaz A.: Dynamic mechanical and impact property correlation of nanoclay and graphite platelet reinforced vinyl ester nanocomposites. Journal of Reinforced Plastics and Composites, in press, (2009).
DOI: 10.1177/0731684409341762

[13] Hertzberg W. R.: Deformation and fracture mechanics of engineering materials. Wiley, New York (1989).

eXPRESS Polymer Letters Vol.3, No.11 (2009) 733–742
Available online at www.expresspolymlett.com
DOI: 10.3144/expresspolymlett.2009.91

Sulfated cellulose thin films with antithrombin affinity

*R. Grombe[1], M. F. Gouzy[1], U. Freudenberg[1], T. Pompe[1], S. Zschoche[1], F. Simon[1], K.-J. Eichhorn[1], A. Janke[1], B. Voit[1,2], C. Werner[1,2,3]**

[1]Leibniz Institute of Polymer Research Dresden e.V., Max Bergmann Center of Biomaterials Dresden, Hohe Str. 6, 01069 Dresden, Germany
[2]Center for Regenerative Therapies Dresden (CRTD), Tatzberg 47, 01187 Dresden, Germany
[3]Institute of Biomaterials and Biomedical Engineering, University of Toronto, 5 King's College Road, M5S 3G8 Toronto, Ontario, Canada

Received 8 June 2009; accepted in revised form 1 September 2009

Abstract. Cellulose thin films were chemically modified by *in situ* sulfation to produce surfaces with anticoagulant characteristics. Two celluloses differing in their degree of polymerization (DP): CEL I (DP 215–240) and CEL II (DP 1300–1400) were tethered to maleic anhydride copolymer (MA) layers and subsequently exposed to $SO_3{\cdot}NMe_3$ solutions at elevated temperature. The impact of the resulting sulfation on the physicochemical properties of the cellulose films was investigated with respect to film thickness, atomic composition, wettability and roughness. The sulfation was optimized to gain a maximal surface concentration of sulfate groups. The scavenging of antithrombin (AT) by the surfaces was determined to conclude on their potential anticoagulant properties.

***Keywords:** biocompatible polymers, cellulose, sulfation, maleic anhydride copolymer*

1. Introduction

Cellulose is one of the most widely used materials of natural origin [1]. The biopolymer was also one of the first biomaterials used [2] and cellulosic membranes still play an important role in extracorporeal life support [3]. However, the blood compatibility of cellulosic materials is limited [4, 5]. Among the related processes thrombosis is a major problem [6]. Thrombus formation is a life-threatening event resulting from a series of enzymatic hydrolysis steps known as the blood coagulation cascade. The serpin antithrombin (AT) is the most important regulator of the coagulation enzymes under physiological conditions. Its activity is drastically enhanced after complexation with polyanionic polysaccharides such as heparin [7]. Although chemically bound heparin shows a reduced biological activity compared to free heparin [8], the blood compatibility of cellulosic membranes was found to be improved upon heparinization [9]. Beyond that, partially sulfated cellulose was considered promising for biomaterials coatings [10]. Due to their action on AT, such coatings were demonstrated to reduce the coagulation processes at the blood/material interface [11–13]. Such coatings could be useful for the surface-selective modification of catheters and several other devices temporarily applied in direct blood contact. However, neither the degree of polymerization (DP) of the cellulose chain nor the degree of sulfation (DS) were so far systematically studied with respect to the bioactivity of the obtained coatings. Since these characteristics influence the structure and AT affinity of the cellulose layers knowledge about the relevance of these parameters appeared important for the intended application of this approach in the sur-

---

*Corresponding author, e-mail: werner@ipfdd.de face modification of biomaterials we performed a series of experiments to explore the impact of these features.

Maleic anhydride copolymer (MA) thin films were shown to be a versatile platform for the biomolecular functionalization of solid supports [14]. Previous studies included the covalent attachment of cellulose on MA pre-coatings via an esterification reaction [15]. This approach was applied in the present work to gain thin and stable cellulose coatings using two types of cellulose CEL I (DP 215–240) and CEL II (DP 1300–1400). Based on that, we report a straightforward modification of cellulose layers by in situ sulfation of the cellulosic hydroxyl groups.

A schematic representation of the derivatized poly(ethylene-alt-maleic anhydride) copolymer (PEMA) thin films is displayed in Figure 1. The shown three different types of investigated surfaces – Group A: PEMA-HYDRO, hydrolyzed PEMA; Group B: PEMA-CEL I, II, cellulosic PEMA; Group C: PEMA-CEL I, II-sulf, sulfated cellulosic PEMA (R=OH, SO_3^-) – shall present a systematic approach towards heparinoid interfaces. Several reaction parameters (concentration of the sulfation reagent $SO_3{\cdot}NMe_3$, reaction temperature, and reaction time) were varied to investigate their influences on the sulfation process and the resulting surface properties. Changes in film thickness, elemental composition, wettability, and morphology were thoroughly investigated. In particular, the degree of sulfation was assessed from XPS (X-ray photoelectron spectroscopy) data. As a measure of the bioactivity of the films, the AT adsorption onto the sulfated cellulose layers was determined and compared.

2. Experimental section

2.1. Materials

All solvents and reagents were used without further purification. Aqueous ammonia solution (Acros Organics, Geel, Belgium) and hydrogen peroxide solution (Merck, Darmstadt, Germany) were employed for the pre-cleaning of the silicon wafers and glass coverslips.

Poly(ethylene-alt-maleic anhydride) copolymer (PEMA, M_w = 125 000 g/mol, Sigma-Aldrich, Munich, Germany) was used for solid support coating. The immobilized native cellulose types were CEL I (DP 215–240, Aldrich-Fluka Chemicals) and CEL II (DP 1300–1400, kindly provided by Membrana GmbH, Wuppertal, Germany). The solvents dimethyl sulfoxide (DMSO), 4-methylmorpholine-4-oxide monohydrate (NMMO), and dimethylformamide (DMF) as well as the sulfur trioxide-trimethylamine complex $SO_3{\cdot}NMe_3$ were purchased from Aldrich-Fluka Chemicals. Human antithrombin (AT) was supplied by Sigma-Aldrich Chemie GmbH (Steinheim, Germany). Normal donkey serum (NDS, Jackson ImmunoResearch Laboratories Inc., USA) was used as blocking

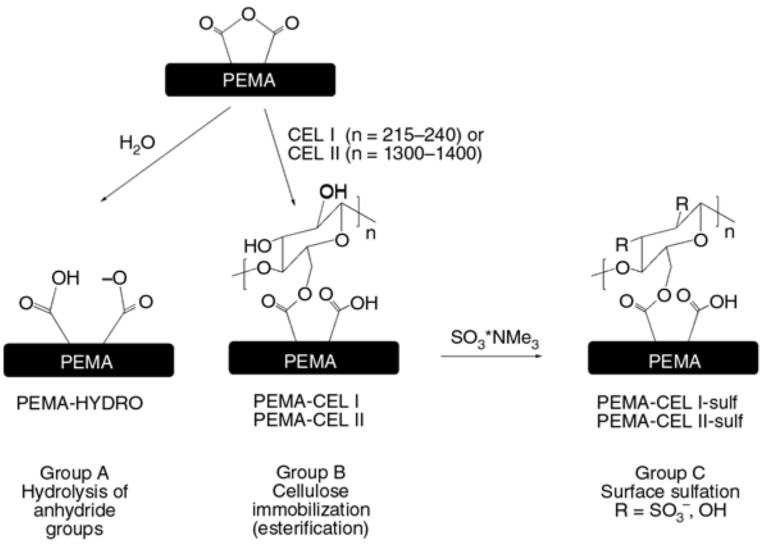

Figure 1. Schematic representation of the surfaces investigated in this study. The modified poly (ethylene-alt-maleic anhydride) copolymer (PEMA) thin films are divided into three groups. Group A: PEMA-HYDRO, hydrolyzed PEMA; Group B: PEMA-CEL I, II, cellulosic PEMA; Group C: PEMA-CEL I, II-sulf, sulfated cellulosic PEMA (R=OH, SO_3^-). The comonomer units (ethylene) as well as the linkage to the solid support are not drawn.

buffer. Fluorescein isothiocyanate (FITC) conjugated sheep anti-human AT was purchased from Cedarlane Laboratories LTD (Hornby, Canada). The substances used during the AT adsorption experiments were dissolved in Phosphate buffered saline buffer (PBS, Sigma, Schnelldorf, Germany).

2.2. Surface preparation and modification

Stable copolymer thin films were prepared by spin-coating (RC5, Suess Microtec, Garching) of a 0.15 wt% solution of PEMA in acetone/THF (1/2) onto previously cleaned and amino-silanized silicon wafers (10×20 mm) or glass coverslips (22×22 mm) following a procedure described elsewhere [14]. The two celluloses (CEL I, CEL II) were subsequently immobilized onto the PEMA films. A 0.5 wt% solution of cellulose (CEL I or CEL II) in dimethyl sulfoxide/4-methylmorpholine-4-oxide monohydrate (solution of 40 wt% DMSO and 60 wt% NMMO) was used for immobilization following a published procedure [15]. The polymer-coated (Si wafer or glass) carriers were tempered at 120°C for 2 h just prior to spin coating to regenerate the anhydride form of the copolymers. Subsequently, the carriers (preheated at 45–50°C) were spin coated with the hot cellulose solutions (60 s, 3000 rpm, 1500 rpm/s). The samples were prepared as series at the same temperature guaranteeing equal preparation conditions. After spin coating, the samples were immersed into MilliQ water for precipitation of the cellulose layers. Air drying overnight followed by vacuum-drying for 2 h at 120°C. Solvent residues were removed by immersion of the samples in MilliQ water (twice for 1 h). The samples were dried then under a N_2 stream. Prior to the introduction of the sulfate groups, the cellulose-PEMA samples were dried at 70°C for 1 h in a vacuum oven. The samples were then immersed into a $SO_3{\cdot}NMe_3$ solution in DMF and heated up. Three cellulosic samples were treated per different reaction condition. After cooling down to ambient temperature, the samples were washed thoroughly with DMF and immersed into a 0.01 N NaOH solution for 10–15 min. Afterwards, the sulfated films were kept in deionized water overnight, dried under a N_2 stream, and placed at 120°C for 2 h.

2.3. Methods

The layer thickness values were determined by ellipsometry on polymer-coated Si wafers in the dry state. Investigations were carried out on a variable angle spectroscopic ellipsometer M-2000VI (371–1680 nm, Woollam Inc., Lincoln, USA) in a polarizer compensator sample analyzer (PCSA) configuration. Two samples were measured and at least three measurements on each wafer were performed. The two Stokes parameters Δ (phase shift) and Ψ (amplitude ratio) were calculated using an optical 4 phases model (Si/SiO_2/polymer/ambient) [16]. The optical constants of Si and SiO_2 were taken from the literature [17, 18]. The best fit results (without roughness correction) gave the effective refractive indices and thickness values for the overall polymer layer system on the wafer surface.

X-ray photoelectron spectroscopy (XPS) measurements were performed to determine the elemental composition of the polymer films. XPS spectra of cellulose bearing surfaces were recorded on an Axis Ultra spectrometer (Kratos Analytical, Manchester, United Kingdom). Monochromatic AlKα X-rays of 300 W at 20 mA were applied. The kinetic energy of photoelectrons was measured using a hemispherical analyzer (take-off angle of 0°) having a constant energy pass of 160 eV for survey spectra and 20 eV for high-resolution spectra. All spectra were referenced to 285.0 eV (C_xH_y binding energy). Quantitative elemental compositions were determined from the peak areas of the survey spectra using experimentally determined sensitivity factors and the spectrometer transmission function. The high-resolution spectra were deconvoluted by means of Kratos Analytical software. The following parameters were fitted: binding energy, peak height, full width at half-maximum, and Gaussian-Lorentzian ratio of the component peaks.

The surface densities [mol/cm^2] of anhydride groups (Γ_{PEMA}) and of cellulose repeating units AGU (Γ_{CEL}) were estimated using a model developed by Pompe *et al.* [19]. Estimations from the elemental composition determined by XPS were executed based on a linear regression analysis assuming a density of 2.85 g/cm^3 of the detected SiO_2 from the silicon wafer substrate and a mean attenuation length of the XPS signal in the substrate and the surface layer of about 3 nm [20, 21]. Within this routine the elemental compositions (C_xH_y, C–OH, COOH, N, Si) of the layer components (SiO_2, PEMA, PEMA-CEL I or PEMA-CEL II) were fitted to the XPS data in a least square sense. The grafting yields (Φ) were defined as the ratio of the surface densities of cellulose units (AGU) and the PEMA repeating units ($\Gamma_{CEL}/\Gamma_{PEMA}$). The degree of sulfation (DS) was calculated from XPS data (C1s and S 2p), Φ and the carbon number of a modified MA unit.

Dynamic contact angle measurements were carried out on an optical contact angle device OCA 30 (Dataphysics, Filderstadt, Germany). Droplets of deionized water were placed onto freshly annealed samples. At least three measurements on each sample were performed. The data presented as mean value and standard deviation.

The surface topography was investigated on one sample using a Dimension 3100 Nano-Scope IV AFM (Veeco, USA). An area of 2×2 µm was measured in tapping mode. The cantilever (Si-SPM-cantilever, BudgetSensors, Bulgaria) had a spring constant of ca. 40 N/m and a resonance frequency of ca. 300 kHz. The tip radius was lower than 10 nm. The mean surface roughness values were calculated using the Nanoscope software.

2.4. Antithrombin binding studies

Antithrombin (AT) adsorbed onto the modified surfaces was detected by immunostaining-fluorescence microscopy. Glass slides bearing sulfated coatings were placed into home-developed screening chambers having a test-material area of 2 cm². Two samples were incubated with a 0.1 U/ml AT solution in PBS buffer for 30 min at room temperature. As reference a third sample was incubated in PBS buffer for 30 min at room temperature. After incubation, the three samples were rinsed twice with PBS, thereafter incubated with 60 mg/ml normal donkey serum solution for 30 min and subsequently washed twice using a 0.1% PBS-donkey serum buffer (PBS-NDS). The surfaces were then incubated with a 7 µg/ml solution of FITC-conjugated sheep anti-human AT in 0.1% PBS-NDS for 1 h. Finally, the samples were washed twice with 0.1% PBS-NDS, then mounted on microscopy slides, and imaged using a confocal laser scanning microscope (TCS SP, Leica, Bensheim, Germany) having a 40× oil immersion objective. The microscope settings were kept constant to allow a direct comparison of the fluorescence intensities measured on the different surfaces. The images were quantified using Image J software (freeware, http://rsb.info.nih.gov/ij/). The experiments were performed in duplicate and the relative fluorescence intensities are reported as average of at least 5 measurements on each slide. The results are shown as mean value and standard deviation.

3. Results and discussion

3.1. Cellulose-grafted PEMA surfaces

Prior to cellulose attachment, the PEMA pre-coatings had a film thickness of 6.3 ± 1.1 nm. The cellulose immobilization resulted in thin films of 14.9 ± 1.3 nm (PEMA-CEL I) and 19.0 ± 1.5 nm (PEMA-CEL II). The refractive indices (measured at a wavelength of λ = 630 nm) of PEMA-CEL I (1.56 ± 0.02) and PEMA-CEL II (1.52 ± 0.02) were slightly different.

The atomic composition of PEMA-CEL I and PEMA-CEL II was determined by XPS (see Table 1). Based on detailed XPS investigations previously reported [15], 4 types of carbon atoms with different chemical environment were defined within the cellulosic layers and are listed in Table 2. The related high-resolution C1s spectrum of a cellulose film on a PEMA support is given in Figure 2a. The C1s spectrum deviates from the typical shape expected for cellulosic materials, however similar spectra were previously obtained for

Table 1. Atomic concentrations (at %) of the survey XPS spectra of PEMA-CEL I and PEMA-CEL II (for preparation condition of cellulosic surface see chapter 2.2); binding energies: C1s: 286.7 eV, O1s: 533.0 eV, Si2p : 103.4 eV, N1s: 401.2 eV

	C1s	O1s	Si 2p	N1s
at $\%_{\text{PEMA-CEL I}}$	57.8±1.4	38.6±1.1	2.4±0.6	1.2±0.1
at $\%_{\text{PEMA-CEL II}}$	57.0±0.2	42.1±0.2	0.4±0.0	0.8±0.4

Table 2. Components of the C1s peak of the cellulosic PEMA thin films, R = organic rest

Components	Binding energy [eV]	Chemical group
A	285.0	aliphatic carbons
B	286.6	–CH(H,R)OH
C	288.1	–O–CHR–O–, CHO
D	289.1	–COOR, COOH, –CO–O–CO–

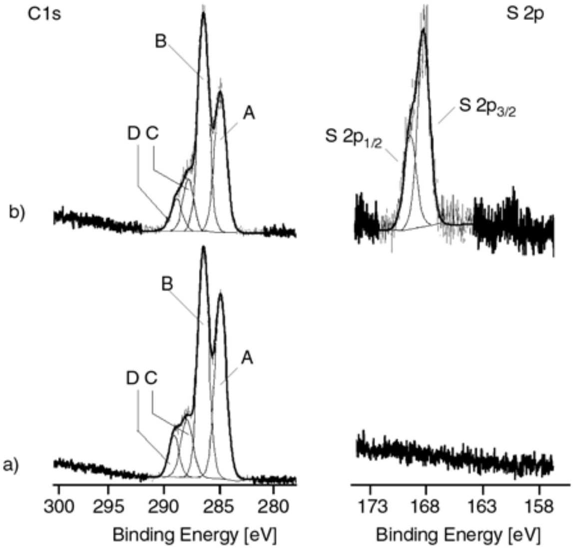

Figure 2. High-resolution C1s (left) and S 2p (right) XPS spectra of a cellulose film immobilized with PEMA on a support before (a) and after its sulfation (b); the sulfation conditions were $c_{SO_3 \cdot NMe_3}$ = 5 wt%, 90°C, 3 h

similar sample preparations [15]. Component peak A results from saturated hydrocarbons of the PEMA plus adsorbed hydrocarbon contaminations, which are commonly observed on surfaces. The reacted (ester bonds between cellulose and PEMA) and remaining anhydride groups of PEMA were assigned to component peak *D*. The two component peaks *B* and *C* mainly reflect the C–OH and C–O–C (*B*) and acetal groups of cellulose (*C*). Autocatalytic degradation of cellulose in NMMO solutions is described in the literature [22]; oxidized cellulose species, such as keto groups are produced and contribute to the component peaks *C* as well. The corresponding S 2p spectrum does not show any traces of sulfur. The atomic percentages obtained by deconvolution of the C1s signal for PEMA-CEL I and PEMA-CEL II are given in Table 3. The ratio of C–OH/–O–CHR–O (component B/component C) is about 4/1 for both types of cellulose. This value differs from the theoretical value (5/1) of pure cellulose and may indicate the occurrence of cellulosic oxidation products which contribute to component C. The cellulose surface densities obtained from the XPS data are summarized in Table 4. The anhydride density Γ_{PEMA} was calculated to be 1.43 nmol/cm^2. Surface densities of $\Gamma_{CEL\ I}$ = 0.83 nmol/cm^2 and $\Gamma_{CEL\ II}$ = 1.88 nmol/cm^2 were estimated for the PEMA-CEL I and PEMA-CEL II films, respectively. For PEMA-CEL I a grafting yield of 0.58 AGU:PEMA units was calculated whereas a value of 1.30 AGU:PEMA units was determined for PEMA-CEL II. The differences in grafting yield are attributed to the different molecular weight of the cellulose samples with CEL II being approx. 5 times bigger than CEL I. The calculated grafting yield might be considered quite low, however, its normalization to the number of PEMA units is the origin of the low value as only a few PEMA units of the PEMA layer are available for the grafting of the cellulose molecules. Hence, still a good coverage of the surface by CEL I and CEL II can be expected.

Table 3. Atomic concentrations [%] of the components of the C1s peak in PEMA-CEL I and PEMA-CEL II

Surfaces	A	B	C	D	B/C
	atomic %				
PEMA-CEL I	38.9	42.1	10.7	8.3	3.9
PEMA-CEL II	21.4	59.0	14.5	5.6	4.1

The wettability characteristics of the cellulosic films are reported in Table 5. The hydrophilicity of the layered substrates increased upon cellulose attachment: compared to the plain PEMA (65°), cellulosic layers displayed advancing contact angle of 51 and 33° for PEMA-CEL I and PEMA-CEL II, respectively. In comparison, water contact angles of 25–30° were previously reported for pure cellulose samples and cellulosic membranes used for hemodialysis were characterized with values of about 33° [23, 24]. The wettability of PEMA-CEL II, close to values of the pure cellulose, seems to indicate an almost complete coverage of PEMA by the high DP polysaccharide. The hysteresis values of 28 and 16°, found for PEMA-CEL I and PEMA-CEL II films respectively, point to a more homogenous surface coverage in the case of

Table 4. Surface densities of disaccharide units Γ_{CEL}, calculated from XPS data [19], S 2p/C1s ratio from XPS measurement (take-off angles $\Theta = 0°$), degree of sulfation (DS) of PEMA-CEL I-sulf, PEMA-CEL II-sulf, and the corresponding sulfate densities of the modified surfaces ($c_{SO_3 \cdot NMe_3}$ = 5 wt%, 90°C, 3 h)

Surfaces	Γ_{CEL} [nmol/cm^2]	S 2p/C1s ratio	DS	ρ [pmol/cm^2]
PEMA-CEL I-sulf	0.83	0.05	0.56	460
PEMA-CEL II-sulf	1.88	0.03	0.41	770

Table 5. Advancing/receding water contact angles and hysteresis values of PEMA-CEL I-sulf and PEMA-CEL II-sulf after 3 and 24 h ($c_{SO_3 \cdot NMe_3}$ = 5 wt%, 90°C)

Surfaces	Adv. contact angle ± SD [°]	Rec. contact angle ± SD [°]	Contact angle hysteresis [°]
PEMA-CEL I	50.7 ± 0.2	22.7 ± 0.1	28.0
PEMA-CEL I- sulf (3 h)	46.4 ± 0.2	19.3 ± 0.3	27.0
PEMA-CEL I- sulf (24 h)	38.4 ± 0.3	17.4 ± 0.2	21.0
PEMA-CEL II	33.3 ± 0.3	17.8 ± 0.2	15.5
PEMA-CEL II- sulf (3 h)	52.9 ± 0.2	15.8 ± 0.3	37.2
PEMA-CEL II- sulf (24 h)	51.0 ± 0.2	17.1 ± 0.1	33.9

PEMA-CEL II. The surface roughness determined from AFM measurements were 2.9 and 2.3 nm for PEMA-CEL I and PEMA-CEL II, respectively. These values are in good agreement with data on cellulose films immobilized from solutions with higher cellulose concentration (> 0.5 wt%) [15].

3.2. Sulfation of the cellulosic PEMA surfaces

The cellulose coatings were sulfated using a sulfur trioxide complex with DMF as the solvent. This experimental condition was chosen based on previous results reported for the sulfation of glycosides performed in the liquid phase [25, 26].

The high-resolution C1s and S 2p spectra of a cellulose film recorded after sulfation are reported in Figure 2b. The shape of the C1s spectrum (Figure 2b left) differs only slightly from the spectrum of the non-sulfated sample. Compared to component peak *B* the intensities of the two component peaks *A* and *D* seem to be slightly decreased. The S 2p spectrum clearly shows the presence of sulfur (Figure 2b right). The S 2p peak is composed of the S $2p_{1/2}$ and S $2p_{3/2}$ peaks. Their binding energy difference and the intensity ratio indicate that only one sulfur species is present on the sample surface. The binding energy of the S $2p_{3/2}$ peak, 168.7 eV, is typical for sulfate groups.

The sulfation conditions were optimized on PEMA-CEL I films to achieve a maximal decoration of the surface with the sulfate groups. The concentration of the sulfation reagent $SO_3 \cdot NMe_3$ in DMF ($c_{SO_3 \cdot NMe_3}$ = 1, 2.5, 5 wt%), the reaction temperature (60, 90°C) as well as the reaction time (3, 24 h) were varied. No relevant film thickness alterations were detected by ellipsometry even under the most drastic reaction conditions (5 wt% $SO_3 \cdot NMe_3$ at 90°C during 24 h).

The sulfur/carbon (S/C) ratios of PEMA-CEL I-sulf films calculated from XPS data are displayed in Figure 3. Variation of the $SO_3 \cdot NMe_3$ concentration at 60°C resulted only in minor S/C ratio changes (data not shown). The elevation of the reaction temperature had a stronger impact on the sulfation process. For a reaction time of 3 h using 5 wt% $SO_3 \cdot NMe_3$, an increase of the S/C ratio was found for 90°C (0.046) compared to 60°C (< 0.01). As the solubility of the cellulose in DMF increased with the temperature, a better penetration of the sulfation reagent into the films can be assumed. At the same reaction temperature (90°C), the total S/C value was not dependent on the reaction time: no significant changes could be observed after 24 hours compared to 3 hours. However, angle dependent XPS measurements (take-off angles Θ = 0, 60, 75°) carried out for reactions times of 3 and 24 hours (Figure 4) revealed the chemical composition of the film at different depths. For the shorter reaction time (3 h), a gradient of the S/C could be observed. The number of introduced sulfate groups was declining towards the interior of the film. For a 24 hours reaction time the S/C gradient vanished: surface and interior of the PEMA-CEL I were sulfated in a similar way. We assume that the solubility of the celluloses in DMF is kinetically controlled.

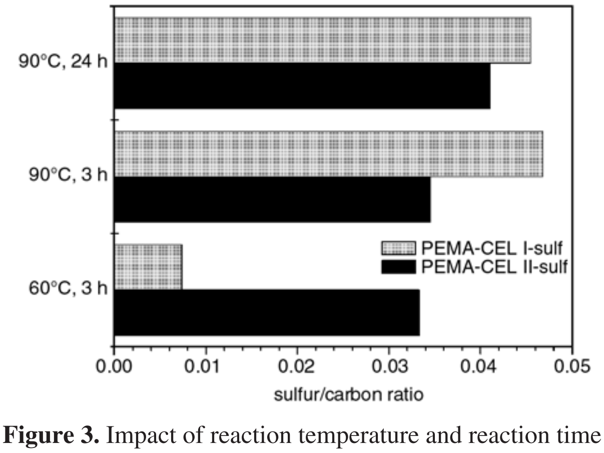

Figure 3. Impact of reaction temperature and reaction time on the sulfur/carbon ratio (XPS measurements) using $c_{SO_3 \cdot NMe_3}$ = 5 wt%

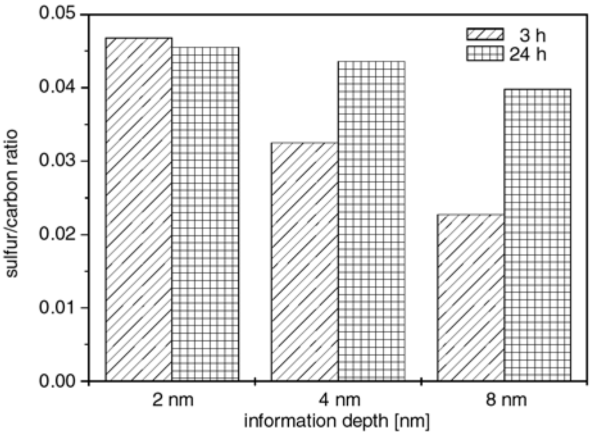

Figure 4. PEMA-CEL I-sulf ($c_{SO_3 \cdot NMe_3}$ =5 wt%, 90°C): dependency of the S2p/C1s on reaction time (3 and 24 h) at 3 different film depths

As a maximal S/C ratio of PEMA-CEL I-sulf was obtained using a 5 wt% $SO_3 \cdot NMe_3$, the same concentration was utilized to produce PEMA-CEL II-sulf. As the DP of CEL II was about 6 times the DP of CEL I, a decrease of the S/C value due to decreased solubility in DMF was expected. However, at 60°C, the S/C value of 0.033 (see Figure 3) was about 5 times higher than PEMA-CEL I-sulf which suggests a higher OH abundance at the solid-liquid interface. A marginal increase of the S/C ratio was observed for PEMA-CEL II-sulf when the temperature was increased to 90°C. This observation suggests that an almost complete sulfation of the surface hydroxyl groups was already reached at 60°C. At longer reaction times (24 hours) OH groups within the bulk volume of the film became accessible to the $SO_3 \cdot NMe_3$ complex resulting in a further increase of the S/C ratio (0.041).

From the atomic concentrations of C1s and S2p (detected by XPS) the degree of sulfation (DS) was estimated for CEL I and CEL II surface obtained using 5 wt% $SO_3 \cdot NMe_3$ at 90°C for 3 h (Table 4). Lower S/C ratios were obtained for PEMA-CEL II (0.033) when compared to PEMA-CEL I (0.046). These ratios correspond to calculated DS values of 0.41 and 0.56, respectively. Both values remain far below the DS of heparin (2.7) and correspond to about one sulfate group per disaccharide unit (which is similar to the sulfation grade of heparan sulfate molecules) [27]. Based on the DS values, the surface concentrations of the sulfate groups were calculated to be 460 pmol/cm^2 for PEMA-CEL I-sulf and 770 pmol/cm^2 in the case of PEMA-CEL II-sulf.

Low concentrations of $SO_3 \cdot NMe_3$ (1 and 2.5 wt%) did not influence the advancing contact angle values (CA) of PEMA-CEL-sulf (data not shown). As listed in Table 5 the treatment of PEMA-CEL I with a 5 wt% sulfation solution at 60°C during 3 hours led to a slight increase of the surface hydrophilicity (from 51 to 47°). A comparable value was obtained for the experimental conditions: 5 wt%, 90°C, 3 h. Significant changes were observed after increasing the reaction time from 3 to 24 h. After 24 h, decreased advancing contact angle (38°) and hysteresis (20°) were observed for PEMA-CEL I-sulf. PEMA-CEL II-sulf (5 wt%, 90°C, 3 h) displayed more hydrophobic (53°) and inhomogeneous (hysteresis = 40°) surface properties. After 24 h sulfation, the advancing contact angle decreased but remained above the values determined before sulfation i.e. the introduction of sulfate groups on the surface did not lead, as expected, to an enhanced surface wettability. Since the surface roughness did not change upon sulfation (see below) we assume rearrangements of the amourphous-crystalline structure of the cellulose layers to cause this unexpected behavior.

The AFM height images and the cross-section profiles of PEMA-CEL I-sulf and PEMA-CEL II-sulf (5 wt% $SO_3 \cdot NMe_3$, 90°C, 24 h) are given in Figure 5. Similar surfaces topographies were obtained for both surfaces. The surface roughness values did not significantly change compared to samples before sulfation.

3.3. Surface binding of antithrombin

In this study, the hydrolyzed polymer layers PEMA-HYDRO were taken as a negative reference (no sulfate groups, no polysaccharidic backbone). The total hydrolysis of the anhydride moieties was achieved by autoclaving at 120°C, under saturated water vapor during 20 min. The PEMA CEL I-sulf and CEL II-sulf were prepared under the sulfation conditions: 5 wt% $SO_3 \cdot NMe_3$ in DMF, 90°C, 3 h.

The amount of antithrombin (AT) bound to the hydrolyzed and derivatized MA substrates was estimated by immunostaining-fluorescence microscopy. The fluorescence intensities Λ measured by cLSM are shown in Figure 6. The reference values (black bars) were obtained after incubation with a fluorescent labeled antibody anti-antithrombin (anti-AT) and showed a weak non-specific adsorption of the

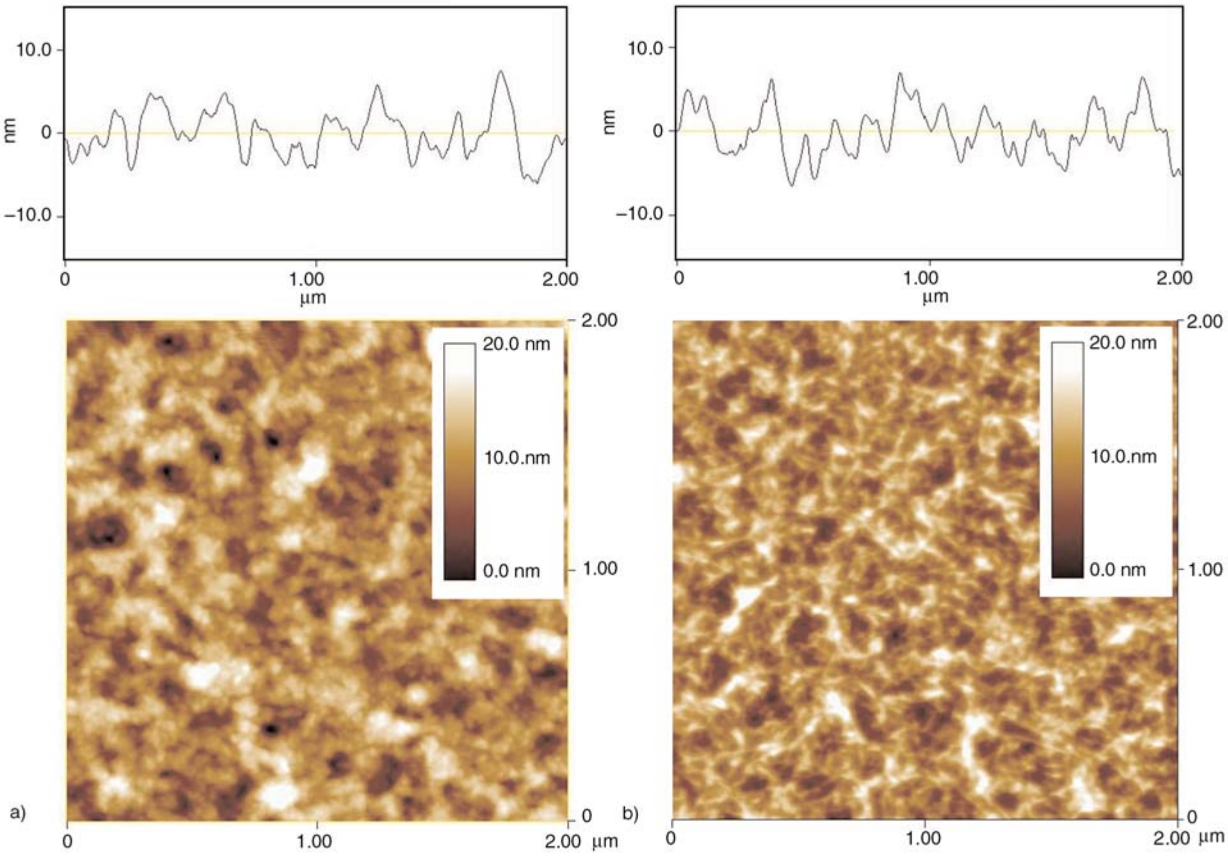

Figure 5. AFM height images and cross-section profiles of PEMA-CEL I-sulf (A) and PEMA-CEL II-sulf (B) obtained after treatment using 5 wt% $SO_3{\cdot}NMe_3$ at 90°C for 24 h

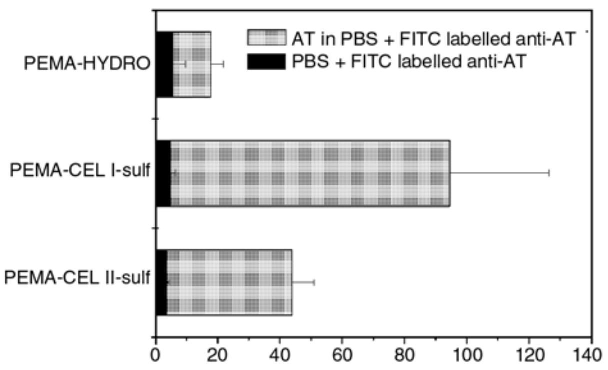

Figure 6. Adsorbed antithrombin (AT) on modified and hydrolyzed PEMA surfaces as determined by laser scanning microscopy (sulfation conditions: 5 wt% $SO_3{\cdot}NMe_3$ in DMF, 90°C, 3 h)

antibody on all the surfaces. Surface-scavenged AT was observed on all films. Hydrolyzed MA (PEMA-HYDRO) providing a highly negatively charged surface without glucose moieties or sulfate groups had the lowest AT binding capacity (18 a.u.). A significantly higher AT anchorage has been observed on a PEMA-CEL I-sulf surface (95 a.u.) while the less sulfated PEMA-CEL II-sulf scavenged comparatively almost 50% (44 a.u) less AT.

The comparison of the results obtained with sulfated CEL I and CEL II samples clearly demonstrates the importance of the DS for the AT binding: the slightly lower DS of CEL II correlates with a lower AT binding. The total sulfate density of the surfaces does not correlate with the AT binding indicating that only sulfate groups on the topmost part of the surface seem to contribute.

4. Conclusions

Systematic studies on structure-bioactivity correlations of potentially anticoagulant surfaces are required for the rational design of hemocompatible materials. In this work, two celluloses were attached onto poly(ethylene-alt-maleic anhydride) pre-coatings. The grafting of the cellulose depended on the degree of polymerization (DP) of the polysaccharide: CEL II (DP~1350) > CEL I (DP~230). The reactivity of the hydroxyl groups of the surface confined cellulose films with $SO_3{\cdot}NMe_3$ complex was found to be a function of reaction time, reaction temperature, and concentration of the sulfation agent. For the applied sulfation conditions (5 wt% $SO_3{\cdot}NMe_3$ at 90°C for 3 h) the calculated degree of sulfation (DS) of the films was lower for layers consisting of cellulose with higher DP. The cellulose films showed an enhanced antithrombin binding (compared to the highly negatively charged PEMA surface) pointing at the importance of the molecular structure for the affinity. Antithrombin binding was furthermore found to correlate well with the DS of the cellulose sample, but not with the total sulfate content of the layers. The latter observation indicates that only sulfate groups on the topmost surface of the films influence the interaction with the serpin.

Acknowledgements

This work was funded by the German Federal Ministry of Science and Education (Grant No. 03N4022: 'BMBF Kompetenzzentrum für Materialien im Blut-und Gewebekontakt'). The authors thank R. Schulze for ellipsometry measurement, D. Pleul for XPS measurements, C. Lehmann for the kind support during the preparation of the cellulose films, Dr. C. Sperling and Dr. M. F. Maitz for the fruitful discussions (all from the Leibniz Institute of Polymer Research Dresden e.V.).

References

[1] Kamide K.: Cellulose and cellulose derivatives – Molecular characterization and its application. Elsevier, Amsterdam (2005).

[2] Helenius G., Bäckdahl H., Bodin A., Nannmark U., Gatenholm P., Risberg B.: *In vivo* biocompatibility of bacterial cellulose. Journal of Biomedical Materials Research A, **76**, 431–438 (2006).
DOI: 10.1002/jbm.a.30570

[3] Baurmeister U., Vienken J., Luttrell A. W.: Cellulosic versus synthetic membranes: A reasonable comparison? Artificial Organs, **13**, 52–57 (1989).
DOI: 10.1111/j.1525-1594.1989.tb02832.x

[4] Cordonnier D. J., Forêt M.: Biocompatibility criteria in hemodialysis. Contributions to Nephrology, **71**, 30–35 (1989).

[5] Colton C. K.: Analysis of membrane processes for blood purification. Blood Purification, **5**, 202–251 (1987).
DOI: 10.1159/000169472

[6] Cheung A. K., Henderson L. W.: Effects of complement activation by hemodialysis membranes. American Journal of Nephrology, **6**, 81–91 (1986).
DOI: 10.1159/000167060

[7] Linhardt R. J., Toida T.: Heparin analogs-development and applications. in 'Carbohydrates as drugs' (eds.: Witczak Z. B., Nieforth K. A.) Marcel Dekker, New York, 277–341 (1997).

[8] Byun Y., Jacobs H. A., Kim S. W.: Mechanism of thrombin inactivation by immobilized heparin. Journal of Biomedical Materials Research, **30**, 423–427 (1996).
DOI: 10.1002/jbm.820300403

[9] Cheung A. K., Parker C. J., Janatova J., Brynda E.: Modulation of complement activation on hemodialysis membranes by immobilized heparin. Journal of the American Society of Nephrology, **2**, 1328–1337 (1992).

[10] Baumann H., Liu C., Faust V.: Regioselectively modified cellulose and chitosan derivatives for mono- and multilayer surface coatings of hemocompatible biomaterials. Cellulose, **10**, 65–74 (2003).
DOI: 10.1023/A:1023084628101

[11] Baumann H.: The role of regioselectively sulfated and acetylated polysaccharide coatings of biomaterials for reducing platelet and plasma protein adhesion. Seminars in Thrombosis and Hemostasis, **27**, 445–463 (2001).
DOI: 10.1055/s-2001-17955

[12] Baumann H., Richter A., Klemm D., Faust V.: Concepts for preparation of novel regioselective modified cellulose derivatives sulfated, aminated, carboxylated and acetylated for hemocompatible ultrathin coatings on biomaterials. Macromolecular Chemistry and Physics, **201**, 1950–1962 (2000).
DOI: 10.1002/1521-3935(20001001)201:15<1950::AID-MACP1950>3.0.CO;2-3

[13] Groth T., Wagenknecht W.: Anticoagulant potential of regioselective derivatized cellulose. Biomaterials, **22**, 2719–2729 (2001).
DOI: 10.1016/S0142-9612(01)00013-8

[14] Pompe T., Zschoche S., Herold N., Salchert K., Gouzy M-F., Sperling C., Werner C.: Maleic anhydride copolymers- A versatile platform for molecular biosurface engineering. Biomacromolecules, **4**, 1072–1079 (2003).
DOI: 10.1021/bm034071c

[15] Freudenberg U., Zschoche S., Simon F., Janke A., Schmidt K., Behrens S. H., Auweter H., Werner C.: Covalent immobilization of cellulose layers onto maleic anhydride copolymer thin films. Biomacromolecules, **6**, 1628–1634 (2005).
DOI: 10.1021/bm0492529

[16] Azzam R. M. A., Bashara N. M.: Ellipsometry and polarized light. Elsevier, Amsterdam (1987).

[17] Woollam J. A.: User manual VASE and M-44 ellipsometers WVASE 32TM. Woollam Co., Lincoln (1999).

[18] Werner C., Eichhorn K-J., Grundke K., Simon F., Grählert W., Jacobasch H-J.: Insights on structural variations of protein adsorption layers on hydrophobic fluorohydrocarbon polymers gained by spectroscopic ellipsometry (Part I). Colloids and Surfaces A: Physicochemical and Engineering Aspects, **156**, 3–17 (1999).
DOI: 10.1016/S0927-7757(99)00007-2

[19] Pompe T., Renner L., Grimmer M., Herold N., Werner C.: Functional films of maleic anhydride copolymers under physiological conditions. Macromolecular Bioscience, **5**, 890–895 (2005).
DOI: 10.1002/mabi.200500097

[20] Seah M. P., Dench W. A.: Quantitative electron spectroscopy of surfaces: A standard data base for electron inelastic mean free paths in solids. Surface and Interface Analysis, **1**, 2–11 (1979).
DOI: 10.1002/sia.740010103

[21] Cole D. A., Shallenberger J. R., Nvak S. W., Moore R. L., Edgell M. J., Smith S. P., Hitzman C. J., Kirchho J. F., Principe E., Nieveen W., Huang F. K., Biswas S., Bleiler R. J., Jones K. J.: SiO_2 thickness determination by x-ray photoelectron spectroscopy, Auger electron spectroscopy, secondary ion mass spectrometry, Rutherford backscattering, transmission electron microscopy, and ellipsometry. Journal of Vacuum Science and Technology B: Microelectronics and Nanometer Structures, **18**, 440–444 (2000).
DOI: 10.1116/1.591208

[22] Wendler F., Graneß G., Heinze T.: Characterization of autocatalytic reactions in modified cellulose/NMMO solutions by thermal analysis and UV/VIS. Cellulose, **12**, 411–422 (2005).
DOI: 10.1007/s10570-005-2201-4

[23] Gunnars S., Wågberg L., Cohen Stuart M. A.: Model films of cellulose: I. Method development and initial results. Cellulose, **9**, 239–249 (2002).
DOI: 10.1023/A:1021196914398

[24] Jacobasch H-J., Grundke K., Werner C.: Surface characterization of cellulose materials. Papier, **49**, 740–745 (1995).

[25] Wessel H. P., Bartsch S.: Conformational flexibility in highly sulfated β-D-glucopyranoside derivatives. Carbohydrate Research, **274**, 1–9 (1995).
DOI: 10.1016/0008-6215(95)00131-C

[26] Sun X-L., Grande D., Baskaran S., Hanson S. R., Chaikof E. L.: Glycosaminoglycan mimetic biomaterials. 4. Synthesis of sulfated lactose-based glycopolymers that exhibit anticoagulant activity. Biomacromolecules, **3**, 1065–1070 (2002).
DOI: 10.1021/bm025561s

[27] Capila I., Linhardt R. J.: Heparin-protein interactions. Angewandte Chemie International Edition, **41**, 390–412 (2002).
DOI: 10.1002/1521-3773(20020201)41:3<390::AID-ANIE390>3.0.CO;2-B

eXPRESS Polymer Letters Vol.3, No.11 (2009) 743–751
Available online at www.expresspolymlett.com
DOI: 10.3144/expresspolymlett.2009.92

Aluminium trihydroxide in combination with ammonium polyphosphate as flame retardants for unsaturated polyester resin

T. D. Hapuarachchi[1]*, *T. Peijs*[1,2]

[1]Queen Mary University of London, Centre for Materials Research, School of Engineering and Materials, London, E1 4NS, UK
[2]Nanoforce Technology Limited, Joseph Priestley Building, London, E1 4NS, UK

Received 30 April 2009; accepted in revised form 3 September 2009

Abstract. The thermal and reaction to fire characteristics of a flame retardant unsaturated polyester (UP) ternary system are presented here. Thermal gravimetric analysis showed an improved thermal stability between 200–600°C with the addition of ammonium polyphosphate (APP) and aluminium trihydroxide (ATH) formulation. Cone calorimetry tests indicated that ATH is more efficient than calcium carbonate at delaying the ignition time, lowering the carbon monoxide yield and lowering the peak heat release (PHRR). However the addition of APP and ATH to the formulation failed to demonstrate any significant synergistic effect at reducing the PHRR.

Keywords: *thermosetting resins, unsaturated polyester, aluminium trihydroxide, ammonium polyphosphate, flame retardant*

1. Introduction

Unsaturated polyester resins (UP) are extremely versatile in terms of their properties and applications and have been a popular thermosetting resin for glass-fibre reinforced plastics (GRP) [1]. This matrix material has been used for many years in broad technology fields such as naval, offshore applications, automotive and construction industries. The reinforcement of polyesters has been traditionally with glass fibres. Recent studies replacing the traditional fibres with various cellulosic fibre reinforcements have shown promising results. These systems meet the environmental credentials without losing the characteristic properties of composite materials [2–4]. However despite the numerous advantages that polymeric materials provide to society in everyday life, there is an obvious disadvantage related to the high flammability of many polymers. Fire can be broken down into their constituent fire hazards: ignitability, ease of extinction, heat release rate, flame spread, smoke obstruction and smoke toxicity [5–7].

According to fire statistics, more than 12 million fires break out every year in the United States, Europe, Russia and China killing some 166 000 people and injuring several hundreds of thousands. Calculating the direct losses and costs for these countries is difficult, but $500 million per annum is an estimate based on some national data [8]. Therefore, in the pursuit of improved approaches to flame retardancy (FR) of polymers, a wide variety of concerns must be addressed. Competing with expensive flame retardant polymers as well as reducing the overall cost of the final product demands that the FR's are kept at a reasonable cost. This limits the solutions to the problem primarily to

---

*Corresponding author, e-mail: d.hapuarachchi@qmul.ac.uk additive type approaches. These additives must be easily processable with the polymer, must not excessively degrade the other performance properties, and must not create environmental problems in terms of recycling or disposal. Traditional systems such as brominated FR's (e.g. Hexabromocyclododecane (HBCD)) which has been used in many polymers including unsaturated polyester to prevent flame spread, but have significant disadvantages of producing dense smoke and corrosive combustion by-products which can have a negative impact on the environment. Another commonly used filler is alumina trihydrate or aluminium trihydroxide (ATH), which is looked upon as a 'greener' FR. The effectiveness of this flame retardant tends to be limited since relatively large amounts of the filler are needed for adequate flame retardancy (>60 wt%), which has a detrimental effect on the processing and as well as possible alterations to the mechanical properties of the final product. Some previous studies have shown improved flame retardancy of thermoplastic systems based on improving the effect of ATH in combination with other FR fillers such as nitrogen rich melamine [9]. Also, there has been some research carried out using combinations of aluminum trihydroxide together with ammonium polyphosphate (APP) in different polymer systems [10]. These studies resulted in some synergistic or antagonistic behaviour with respect to reducing the flammability of the polymer. To date, these two fillers have not been used together in a UP system. Therefore the purpose of this work is to carry out thermal and cone calorimetry studies on unsaturated polyester resin with ATH in combination with APP to create a flame retardant ternary system.

2. Materials and specimen preparation

This study consisted of bench scale fire testing a set of flame retardant unsaturated polyester specimens. The unsaturated polyester resin (UP) used was a P17 (ortho resin) from Reichhold Organic Chemicals Ltd. A non-flame retardant specimen consisting of 50 wt% calcium carbonate ($CaCO_3$) (~200 phr) supplied by Omya UK was prepared. The flame retardant fillers used were aluminum trihydroxide (OL104) from Albemarle Corporation and Exolit™ ammonium polyphosphate from Clariant. An unfilled unsaturated polyester specimen was also produced as a control specimen. To prepare the specimens, the fillers were dispersed in the UP under excessive shear mixing using a High Speed Mechanical Mixing (HSMM) Citenco, FHP Motors LC9 with four blades. The formulation was mixed for 5 min at 3000 rpm. The specimens were cured in an open steel mould with dimensions of 100×100 mm. The formulations (Table 1) were prepared and cured for 10 min at 140°C in an air circulated oven.

Table 1. UP formulations studied in this investigation

Specimens (weight percentage)
Unsaturated Polyester Resin (UP)
+50wt% Calcium Carbonate ($CaCO_3$)
+30wt% ATH
+40wt% ATH
+50wt% ATH
+50wt% ATH+5wt% APP
+50wt% ATH+10wt% APP
+50wt% ATH+15wt% APP

3. Experimental procedures

3.1. Cone calorimetry

All the tests for this study were conducted in the horizontal orientation. An irradiance of 50 kW/m^2 was used. Ignition was spark induced; specimens were run without a retainer frame and in triplicate and averaged.

3.2. Thermal analysis

Thermogravimetric analysis (TGA) was carried out using TA Instruments Q500 TGA at a heating rate of 10°C/min under air and nitrogen rich atmospheres; with a gas flow rate of 20 ml/min. In each case, specimens of approximately 5 mg were positioned in a platinum pan. Differential scanning calorimetry (DSC) analysis was carried out using Mettler Toledo DSC822e and closed aluminum pans with a pierced hole in the cover. Thermal scans were run from 30–350°C at 10°C/min with specimen masses averaging 5 mg, in air.

4. Results and discussion

4.1. Cone calorimetry

Inorganic hydroxide flame retardant additives decompose when heated, releasing water in the vapour phase of combustion (pyrolysis stage). As

Table 2. The delay in the time to ignition (TTI) for the FR UP specimens

Specimens	TTI [s]
UP	7
+50wt% $CaCO_3$	8
+30wt% ATH	20
+40wt% ATH	22
+50wt% ATH	24
+50wt% ATH+5wt% APP	26
+50wt% ATH+10wt% APP	27
+50wt% ATH+15wt% APP	30

this elimination of water results in an endothermic reaction, heat is removed from the substrate. This removal of heat slows down the decomposition of the substrate, which is indicated by the delay in time to ignition (TTI) (Table 2) and also the reduction in heat release rate (Figure 1).

This phenomenon allows the substrate to remain below its ignition temperature for the duration of the hydroxide decomposition process. Literature reports that the largest of the commercially used inorganic hydroxides absorbs between 1000 and 1500 J/g of energy during decomposition [11]. Although other references may cite different values for this parameter, the apparent discrepancies should not be of great concern, as they are relative. The values obtained depend on the type of equipment used to measure the endothermic response, the heating rate used, the sample size, particle size, crystal morphology, the method of sample preparation and the temperature range used in the determination. The addition of the fillers within the UP shows a delay in ignition times. Interference of the flame is due to the decomposition mechanisms of the individual fillers which are shown by the TGA and DSC thermograms, which will be discussed later. Cone calorimeter tests have been performed to estimate the reaction to fire of the flame retardant UP systems. Many reactions to fire parameters were determined, such as the time to ignition, the heat release rate, mass loss behaviour and the smoke production over time. In this study, tests were carried out at 50 kW/m² heat flux, which in the cone calorimeter is considered to represent a well developed fire [12]. The time to ignition data for the tested UP formulations is shown in Table 2. A marked improvement can be seen in the ATH filled formulations compared to unfilled ones with respect to delaying the ignition time. The UP had a TTI of 7 seconds and combusted violently with a large flame during testing. As the loading of ATH increases the TTI was prolonged.

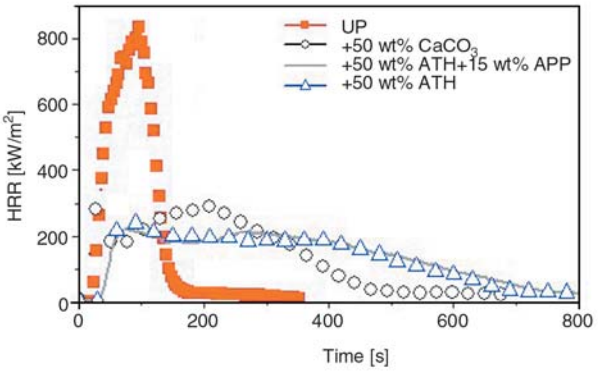

Figure 1. The reduction in heat release rate profile for the FR UP specimens

The ATH starts to break down in the temperature range of 180–200°C, conversion to aluminium oxide taking place in an endothermic reaction with release of water vapour. As a result of the endothermic breakdown, the UP is cooled, and thus fewer pyrolysis products are formed. The water vapour liberated has a diluting effect in the gas phase and forms an oxygen displacing protecting layer over the condensed phase [13].

Table 3 reports a PHRR of 836 kW/m² for the unfilled UP. This was reduced to 289 kW/m² with the introduction of $CaCO_3$, which is thought to occur for two reason; (i) more of the UP volume had been replaced by the filler, thus simply reducing the amount of combustible material present and (ii) when $CaCO_3$ decomposes it releases CO_2 which is thought to form around the flame front and thus diluting the combustion mixture [14].

As the ATH loading increased from 30 to 50 wt% the PHRR decreased from 337 to 244 kW/m², respectively. Inorganic hydroxides are generally used at levels of 50 wt% or more to attain the flame retardant results required. In this study 50 wt% was the maximum loading that could be achieved due to

Table 3. The peak heat release rate (PHRR) and total heat release (THR) of the FR UP specimens

Specimens	PHRR [kW/m²]	THR [MJ/m²]
UP	836	080
+50wt% CaCO3	289	85
+30wt% ATH	337	116
+40wt% ATH	319	113
+50wt% ATH	244	107
+50wt% ATH+5wt% APP	240	105
+50wt% ATH+10wt% APP	230	93
+50wt%ATH+15wt% APP	221	90

very high shear forces needed to disperse the highly viscous mixture. The results show that the calcium carbonate had a positive effect in reducing the PHRR. This was thought to be due to fuel replacement. The ATH reduced the PHRR further, the endothermic and water liberating effect reduced the combustion of the specimen. This was evident from PHRR for 50 wt% ATH and 50 wt% $CaCO_3$ loaded UP specimens, which were 224 and 289 kW/m^2 respectively. The addition of APP also reduced the PHRR. A formulation with the maximum ATH loading of 50 wt% was chosen to formulate three specimens with 5, 10 and 15 wt% APP, the PHRR were 240, 230 and 221 kW/m^2, respectively. Again the explanation for this reduction could be due to more inorganic filler being introduced into the resin thus less UP being available for combustion. However research by Levchik *et al.* [15] and Shen *et al.* [16] have shown a reaction between ATH and APP. Ammonium polyphosphate, a well known component of intumescent flame retardants is considered a shield coating precursor because of the formation of a continuous cross linked vitreous phase called ultraphosphate during thermal decomposition [17]. Whereas aluminium trihydroxide on thermal decomposition undergoes endothermic dehydration releasing water to the gas phase with the *in situ* formation of a thermally stable ceramic material alumina (Al_2O_3).

The formation of an Al_2O_3 surface layer acts in a similar way to an intumescent flame retardant whereby it shields the heat and mass transfer between the unsaturated polyester and the flame. The flame retardant effectiveness of ATH is however detrimental to the mechanical properties (not tested here), i.e. high loadings generally $\geq$ 50 wt% are necessary to reach a suitable flame retardant effect but results in a dense and brittle material [18, 19]. The combined use of ATH and APP was studied aiming at a more thermally stable P–Al–O surface coating instead of the P–O, bringing together film forming action of ultraphosphate with thermal stability of Al_2O_3 to improve high temperature surface protection of the polymer. Table 3 shows the total heat release (THR). Unfilled UP had a THR of 80 MJ/m^2, which increased for the specimen with the addition of ATH and APP. The total heat release is calculated by integrating the area underneath the HRR vs. Time curve. Due to the FR's prolonging the burn time for the specimens results in the slight increase in THR. Zhang *et al.* [20] proposed a correction factor based on theoretical analysis of taking account of the effective heat of combustion of the filler and polymer separately then multiple it with the individual mass loss rates. They suggested that if this correction factor was taken into consideration in their study, then the THR for a PP specimen loaded with 70 wt. % ATH would have been 6.5% lower. Nevertheless the most significant predictor of fire hazard is the heat release rate; therefore the rate at which heat is released is of more interest than the total amount [21, 22]. An increasing burn time is indicative of the FR additive impeding or hindering the combustion process. Also in general the most important factor in evaluating a material is the peak heat release rate (PHRR) as this signifies the time at which the material evolves the maximum amount of heat into the surrounding, this can give a crude indication of the time available to escape the fire before flashover (the near simultaneous ignition of all combustible material in an enclosed area). The unfilled UP reaches its PHRR of 836 kW/m^2 in 96 seconds and the 50 wt% ATH+15 wt% APP system reached its PHRR in 76 seconds but this was only 221 kW/m^2 which is almost 4 times lower than the unfilled UP.

Table 4 shows the time to peak effective heat of combustion (EHC) and average EHC for the specimens tested. The EHC is calculated from the THR and total mass loss, which was reduced from an overall average of 20.79 to 18.81 MJ/kg for the unfilled UP and 50 wt% ATH+15 wt% APP system, respectively. This is an indication of the combustion mechanism being interfered with, most likely in the vapour phase by the FR mechanisms of the aluminum trihydroxide and ammonium poly-

Table 4. The delay in time to peak effective heat of combustion (EHC) and the reduction in average EHC of the FR UP specimens

Specimens	Time to peak EHC [s]	Average EHC [MJ/kg]
UP	236	20.79
+50wt% $CaCO_3$	470	20.86
+30wt% ATH	600	19.92
+40wt% ATH	639	19.44
+50wt% ATH	652	19.28
+50wt% ATH+5 wt% APP	672	19.08
+50wt% ATH+10 wt% APP	728	18.91
+50wt%ATH+15 wt%APP	874	18.81

Table 5. The delay in the time to peak specific extinction area (SEA) for the FR UP specimens

Specimens	Time to peak SEA [s]
UP	136
+50wt% $CaCO_3$	420
+30wt% ATH	645
+40wt% ATH	668
+50wt% ATH	680
+50wt% ATH+5wt% APP	712
+50wt% ATH+10wt% APP	720
+50wt% ATH+15wt% APP	730

phosphate. Also, the time to peak EHC was delayed, which shows that the combustion is being hindered by the flame retardant mechanisms. The results of the smoke parameter measurements made in the cone calorimeter can be expressed in a number of different forms. Table 5 displays the time to peak specific extinction area (SEA), which is the total obstruction area of smoke produced, divided by the total mass loss during the burn.

The shift in the time to peak is most likely to be due to the FR formulations generating a protective charred layer which prevents volatiles and smoke evolving from the specimen's surface. Another important smoke measurement is the average smoke production release (SPR). The SPR is the area of obscuration produced per second. Figure 2 illustrates the effect of FR fillers on reducing the average SPR from 0.06 to 0.04 m²/s for the unfilled UP and 50 wt% ATH+15 wt% APP specimens, respectively. Table 6 lists the total smoke release (TSR) and total smoke production (TSP). The rise in these two properties is indicative of incomplete combustion. This smouldering (flameless combustion) effect results in a longer burn time which, allows for more smoke and soot debris to accumulate which is especially important here due to the high degree of aromatic content (especially the styrene) in the unsaturated polyester resin [23].

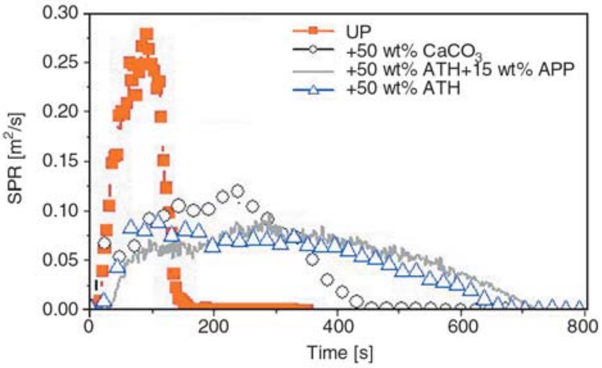

Figure 2. The effect on the smoke production release (SPR) of the FR UP specimens

The gas products released by a decomposing polymer substrate depend on the chemical nature of the organic constituents, oxygen availability, and temperature of the fire. Table 6 also displays the mean carbon monoxide yield (COY) in kg/kg. The mean COY is seen to be inversely proportional to the TSR and TSP. The theory behind this is that more carbon monoxide is liberated at a higher decomposition temperature in the UP. Cunliffe *et al.* [24] carried out this work on the pyrolysis behaviour of various polymers including unsaturated polyester. The generation of carbon oxides would be expected from the breakdown of ester bonds within the resin. The higher pyrolysis temperatures caused by the higher PHRR of the UP would result in more carbon monoxide to be evolved due to further cracking of the polyester chains. While the types and amounts can vary between materials, all polymers release carbon monoxide and carbon dioxide [25, 26]. Carbon monoxide is a major safety concern because it is lethal at a relatively low concentration, with human death occurring within one hour at a concentration of about 1500 ppm.

4.2. Thermal analysis

To examine the effect of FR's on the thermal stability and the decomposition behaviour, TGA data under nitrogen and air atmospheres were determined and analysed. The TGA curve of aluminum

Table 6. The total smoke release (TSR) total smoke production (TSP) and carbon monoxide yield (COY) measurements

Specimens	TSR [m²/m²]	TSP [m²]	Mean COY [kg/kg]
UP	2172	21.7	0.0311
+50wt% $CaCO_3$	3209	32.1	0.0243
+30wt% ATH	3442	34.4	0.0237
+40wt% ATH	3546	35.5	0.0232
+50wt% ATH	3811	38.1	0.0216
+50wt% ATH+5wt% APP	3838	38.4	0.0215
+50wt% ATH+10wt% APP	3914	39.1	0.0213
+50wt% ATH+15wt% APP	3996	39.5	0.0212

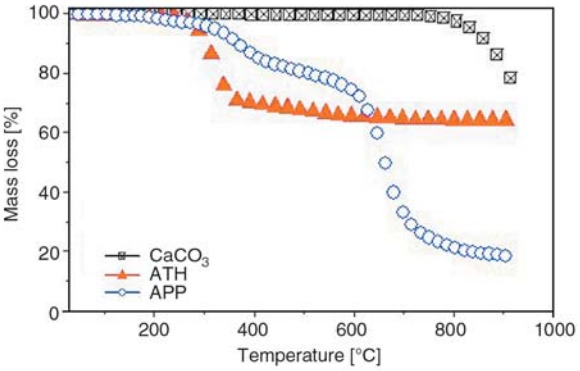

Figure 3. The TGA thermogram of fillers used in the UP formulations

trihydroxide (ATH) (Figure 3) which was heated to 900°C shows one main weight loss step at about 240°C which is due to endothermic release of its 35% water of crystallisation into the gas phase, this leads to the *in situ* formation of a ceramic layer of γ-Al_2O_3. Both the endothermic dehydration and the formation of the ceramic layer are responsible for the FR mechanism of inorganic hydroxides [27].

The TGA analysis carried out on ammonium polyphosphate (APP) shows that the elimination of ammonia and water starts at 190°C (maximum rate of weight loss at 370°C) with transformation of linear crystalline APP into a vitreous crosslinked ultraphosphate) which undergoes fragmentation to volatile P_2O_5. Ammonia evolution from APP is related to acidic sites formation involved in the intumescence phenomenon. Calcium carbonate ($CaCO_3$) thermally decomposes at a much higher temperature than the other two fillers. The single decomposition step occurred at 800°C which indicates a higher thermal stability. Calcium carbonate does not combust; it thermally decomposes and converts through the following mechanism; $CaCO_3 \rightarrow CaO+CO_2$. When $CaCO_3$ is heated to 800°C it liberates CO_2 and will thus become CaO. Figure 4a and 4b show the results of the UP formulations test in the TGA under air and nitrogen respectively. The formulations started to decompose at around 250°C due to the decomposition of the resin system. The unsaturated polyester started to decompose at 250°C, whereas the main weight loss occurred between 300 and 400°C. During thermal decomposition, it is thought that the polystyrene cross-links started to decompose first which was followed by volatilisation of the styrene. The linear polyester portion undergoes scission. Ferreira *et al*. [28] have shown that during thermal decomposition, volatiles are lost UP to 400°C while above 400°C; it is solid phase oxidation reactions that predominate. The 50 wt% $CaCO_3$ specimen demonstrated the best performance in terms of thermal stability when tested in air.

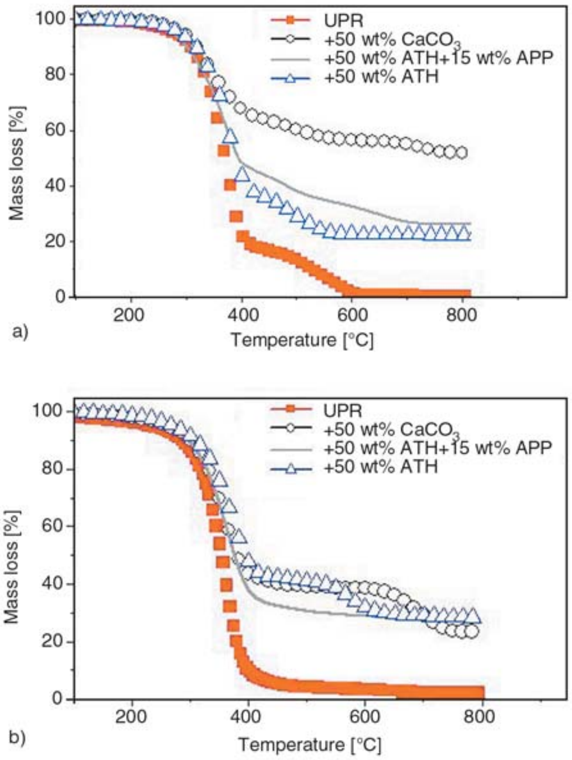

Figure 4. a) The effect of the various fillers and their combination on improving the thermal stability and residual mass of UP, b) The effect of the various fillers and their combination on improving the thermal stability and residual mass of UP tested in nitrogen

The ATH loaded specimens showed a marked improvement in residual weight retention at temperatures above 600°C as the loading level increase. This is thought to be due to the conversion of $Al(OH)_3$ to Al_2O_3 which is a thermally stable engineering ceramic which possesses a melting temperature of 2054°C. The addition of APP to the formulation also increased the residual mass, which was also observed for the cone calorimeter specimens (Table 7). It has been well documented that as APP decomposes it dehydrates and converts into an intumescent char; this could be the reason for the extra residual mass. The ATH+APP specimens which were run under nitrogen (Figure 4b) showed no major differences to those which were tested in air. Since the pyrolysis of polymers during fires are characterised by anaerobe decomposition, it was important to conduct the TGA tests in nitrogen as

Table 7. The peak mass loss rate, residual mass and average specific mass loss for the FR UP specimens from the cone calorimeter

Specimens	Peak mass loss rate [g/s]	Residual mass [%]	Average specific mass loss [g/s·m²]
UP	0.420	6.8	34.4
+50wt% $CaCO_3$	0.220	36.7	11.1
+30wt% ATH	0.210	17.7	14.4
+40wt% ATH	0.170	18.7	13.7
+50wt% ATH	0.165	25.1	10.9
+50wt% ATH+5wt% APP	0.164	26.7	9.7
+50wt% ATH+10wt% APP	0.162	28.4	9.3
+50wt% ATH+15wt% APP	0.161	28.8	9.3

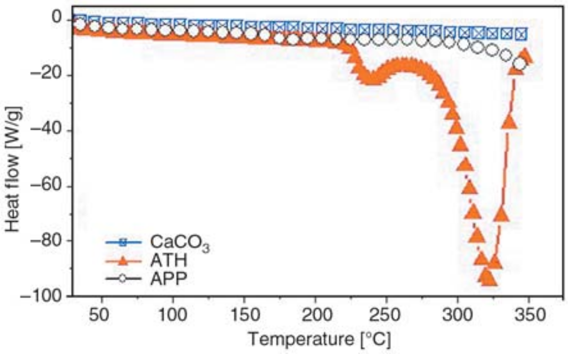

Figure 5. DSC thermogram of the unfilled fillers on their own

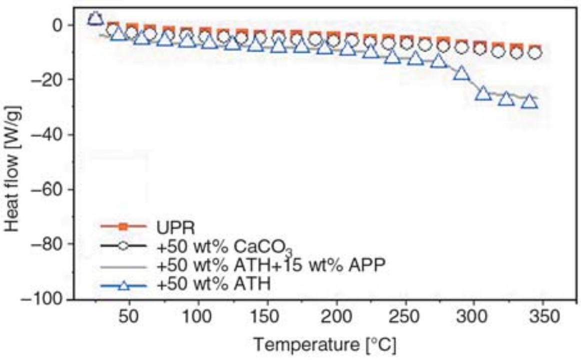

Figure 6. DSC thermogram of the FR UP formulations

well as thermo-oxidative conditions. With respect to char yields, the pure UP comprised of slight more at the end of the run. However the most significant difference was with the $CaCO_3$ specimen. There was rapid decomposition after 400°C and had only a 22% char yield whereas when tested in air it held stable up to 800°C in which it ended with a 55% char yield. The specimen not being able to form a protective skin in the presence of a nitrogen rich atmosphere was thought to be attributed to this difference [29]. Figure 5 shows the energy absorption profile investigated by differential scanning calorimetry (DSC) on the fillers. The aluminum trihydroxide absorbed the most significant amount of thermal energy out of all the fillers. The ATH underwent endothermic decomposition and absorbed 978 J/g of thermal energy. However, the other two fillers did not show any significant endothermic effects. The DSC scan of APP showed an endothermic process between 240 and 260°C which corresponds to polymorphic transitions of residual APP crystal structure form APP I to APP form II, above which ammonia and water elimination begins at low rates as seen from TGA (Figure 6).

This process decreases the concentration of fuel available for combustion and limits the amount of heat being fed back into the surrounding polymer. The result is a decrease in the mass burning rate for the polymer. Figure 6 shows the heat sink effect caused upon by the introduction of ATH into the UP resin. The direct result of this and the evolution of water vapour can be witnessed in Table 2 which shows TTI data. As the ATH loading increases so too does the time to combustion.

5. Conclusions

The purpose of this study was to observe any possible flame retardant improvements to commercial unsaturated polyester using ‘greener’ non-toxic flame retardants. The use of ATH in combination with APP was expected to impart an improved flame retardant effect in the UP system. A combination of both FR’s showed an improved ignition delay time as well as decreases in the peak heat release rate and carbon monoxide yield. However, synergistic behaviour was not witnessed but instead a mere fuel replacement effect on the role of the fillers is more plausible. In general, synergism can be defined as two or more components working together to produce a result not obtainable by any of the components independently. The polymer used plays an important part in the effectiveness of these two FR fillers and their combination does not work with all polymers as shown in the literature. The additional reduction in the PHRR with the addition of APP does not justify its use due to the resultant difficulties with increased viscosity, which will result in major processing difficulties in adopting these materials in potential fibre reinforced composites.

References

[1] Heger F. J., Sharff P. A.: Buildings: Plastics and composites. in 'Encyclopaedia of materials: Science and technology' (eds.: Buschow K. H. J., Cahn R., Flemings M. C., Ilschner B., Kramer E. J., Mahajan S., Veyssiere P.) Pergamon Press, Oxford, 833–841 (2001).

[2] Aziz S. H., Ansell M. P., Clarke S. J., Panteny S. R.: Modified polyester resins for natural fibre composites. Composites Science and Technology, **1**, 525–535 (2005). DOI: 10.1016/j.compscitech.2004.08.005

[3] Goutianos S., Peijs T., Nystrom B., Skrifvars M.: Development of flax fibre based textile reinforcements for composite applications. Applied Composite Materials, **13**, 199–215 (2006). DOI: 10.1007/s10443-006-9010-2

[4] Hapuarachchi T. D., Ren G., Fan M., Hogg P. J., Peijs T.: Fire retardancy of natural fibre reinforced sheet moulding compound. Applied Composite Materials, **14**, 251–264 (2007). DOI: 10.1007/s10443-007-9044-0

[5] Hirschler M. M.: Fire performance of organic polymers, thermal decomposition, and chemical composition. in 'Fire and polymers: Materials and solutions for hazard prevention' (eds.: Nelson G. L., Wilkie C. A.) ACS Symposium Series, Washington, Vol 797, 214–227 (2001).

[6] Purser D. A.: Toxic product yield and hazard assessment for fully enclosed design fires. Polymer International, **49**, 1232–1255 (2000). DOI: 10.1002/1097-0126(200010)49:10<1232::AID-PI543>3.0.CO;2-T

[7] Babrauskas V.: Effective measurement techniques for heat, smoke and toxic fire gases. in 'Fire: Control the heat, reduce the hazard' QMC Fire and Materials Centre, London, 4.1–4.10 (1988).

[8] Manor O., Georlette P.: Flame retardants and the environment. Speciality Chemicals, **25**, 36–39 (2005).

[9] Zilberman J., Hull R., Price D., Milnes G. J., Keen F.: Flame retardancy of some ethylene-vinyl acetate copolymer-based formulations. Fire Materials, **24**, 159–164 (2000). DOI: 10.1002/1099-1018(200005/06)24:3<159::AID-FAM734>3.0.CO;2-D

[10] Castrovinci A., Camino G., Drevelle C., Duquesne S., Magniez C.: Vouters M.: Ammonium polyphosphate-aluminum trihydroxide antagonism in fire retarded butadiene-styrene block copolymer. European Polymer Journal, **41**, 2023–2033 (2005). DOI: 10.1016/j.eurpolymj.2005.03.010

[11] Lyons J. W.: The chemistry and uses of fire retardants. Wiley, USA (1987).

[12] Schartel B., Bartholmai M., Knoll U.: Some comments on the use of cone calorimeter data. Polymer Degradation and Stability, **88**, 540–547 (2005). DOI: 10.1016/j.polymdegradstab.2004.12.016

[13] Sobolev I., Woycheshin E. A.: Alumina trihydrate. in 'Handbook of fillers for plastics' (eds.: Katz H. S., Milewski J. V.) Van Nostrand Reinhold, New York, 292–310 (1987).

[14] Deodhar S., Shanmuganathan K., Patra P., Fan Q., Calvert P., Warner S., Nick C. W.: Polypropylene based novel flame retardant nanocomposite compositions. in 'Technical Papers in Composites 2006 Convention and Trade Show American Composite Manufacturers Association. St Louis, USA' p. 16 (2006).

[15] Levchik S. V., Camino G., Costa L.: Mechanism of action of phosphorous-based flame retardants in Nylon 6. I: Ammonium polyphosphate/talc. Journal of Fire Sciences, **13**, 43–58 (1995). DOI: 10.1177/073490419501300103

[16] Shen C. Y., Stahlheber N. E., Dyroff D. R.: Preparation and characterization of crystalline long-chain ammonium polyphosphate. Journal of the American Chemical Society, **91**, 62–67 (1969). DOI: 10.1021/ja01029a013

[17] Camino G., Luda M. P.: Mechanistic study on intumescence. in 'Fire retardancy of polymers: The use of intumescence' (eds.: Le Bras M., Camino G., Bourbigot S., Delobel R.) Royal Society of Chemistry, Cambridge, 48–63 (1998).

[18] Hippi U., Mattila J., Korhonen M., Seppälä J.: Compatibilization of polyethylene/aluminum hydroxide (PE/ATH) and polyethylene/magnesium hydroxide (PE/MH) composites with functionalized polyethylenes. Polymer, **74**, 1193–1201 (2003). DOI: 10.1016/S0032-3861(02)00856-X

[19] Liauw C. M., Lees G. C., Hurst S. J., Rothon R. N., Dobson D. C.: The effect of surface modification of aluminium hydroxide on the crystallisation behaviour of aluminium hydroxide filled polypropylenes. Macromolecular Materials and Engineering, **235**, 193–203 (1995). DOI: 10.1002/apmc.1996.052350116

[20] Zhang J., Wang X., Zhang F., Horrocks A. R.: Estimation of heat release rate for polymer-filler composites by cone calorimetry. Polymer Testing, **23**, 225–230 (2004). DOI: 10.1016/S0142-9418(03)00098-9

[21] Babrauskas V., Grayson S. J.: Heat release in fires. E and FN spon, Chapman and Hall, London (1992).

[22] Babrauskas V., Peacock R. D.: Heat release rate: The single most important variable in fire hazard. Fire Safety Journal, **18**, 255–272 (1992).

[23] Troitzsch J.: International plastics flammability handbook. Hanser Publishers, New York (1990).

[24] Cunliffe A. M., Jones N., Williams P. T.: Recycling of fibre-reinforced polymeric waste by pyrolysis: Thermo-gravimetric and bench-scale investigations. Journal of Analytical and Applied Pyrolysis, **70**, 315–338 (2003).
DOI: 10.1016/S0165-2370(02)00161-4

[25] Hume J.: Assessing the fire performance characteristics of GRP composites. in 'International conference on materials and design against fire. London, Great Britain' 11–15 (1992).

[26] Sastri S. B., Armistead J. P., Keller T. M., Sorathia U.: Flammability characteristics of phthalonitrile composites. in 'Proceedings of the 42nd International SAMPE Symposium, Anaheim, USA' 1032–1038 (1997).

[27] Bourbigot S., Le Bras M., Leeuwendal R., Shen K. K., Schubert D.: Recent advances in the use of zinc borates in flame retardancy of EVA. Polymer Degradation and Stability, **64**, 419–425 (1999).
DOI: 10.1016/S0141-3910(98)00130-X

[28] Ferreira J. M., Errajhi O. A. Z., Richardson M. O. W.: Thermogravimetric analysis of aluminised E-glass fibre reinforced unsaturated polyester composites. Polymer Testing, **25**, 1091–1094 (2006).
DOI: 10.1016/j.polymertesting.2006.07.012

[29] Krämer R. H., Raza M. A., Gedde U. W.: Degradation of poly(ethylene-co-methacrylic acid)-calcium carbonate nanocomposites. Polymer Degradation and Stability, **92**, 1795–1802 (2007).
DOI: 10.1016/j.polymdegradstab.2007.07.006